Experiments related to the infra-red conversion of the Glasgow 10 m prototype gravitational wave detector

David Alexander Clubley

Presented as a thesis for the degree of
PhD in the University of Glasgow

Summary

Large scale laser interferometric gravitational wave detectors are being constructed by research teams worldwide. The Japanese TAMA 300 interferometer is operational but still under development, the American LIGO detector is operating in a preliminary mode, the British-German GEO 600 interferometer is close to being fully operational and the French-Italian VIRGO project is not far behind. The development of these detectors is possible after nearly 30 years of research using smaller prototype interferometers. The Glasgow prototype interferometer has allowed the development of techniques relevent to all large scale detectors.

This thesis describes recent experiments performed using the Glasgow prototype interferometric gravitational wave detector to convert its laser and optics to operate at 1064 nm. This infra-red conversion brings it into line with the large scale detectors which will all operate with infra-red lasers. Associated with this conversion were related experiments testing optical components for GEO 600.

An injection locked Nd:YAG laser system was constructed and characterised as the new laser source for the interferometer. Experiments to stabilise and measure the frequency noise properties of the laser were performed, using one of the Fabry-Perot cavities which make up the interferometer as a frequency analyser. The transference of the frequency properties of a highly stabilised master oscillator to the high power injection locked slave laser was verified. A measurement of the frequency noise around the relaxation oscillation of a Non Planar Ring Oscilator was performed and a new upper limit set.

The detector was operated with the new laser source and the displacement

sensitivity was close to being shot noise limited. A direct measurement of the thermal noise of a mirror mass was made by damping its mechanical Q-factor, thus making thermal noise the limiting noise source to the detector displacement sensitivity.

A new detector displacement calibration technique was demonstrated using radiation pressure from a low power laser to move one of the detector mirrors. This was shown to be suitable as a calibration method for large scale detectors. GEO 600 optics were characterised and shown to be suitable for use. A new Brewster polariser was shown to have very low optical losses while maintaining a high extinction ratio. The additional phase noise around an electro optically applied phase modulation of the laser field was performed and shown to be at a level below that required for GEO 600.

Finally experiments to make a single frequency Yb:YAG laser system are described. Yb:YAG may be the gain medium of choice for future detector upgrades where very much higher power lasers are required. A single frequency Yb:YAG source was required for testing high power Yb:YAG amplifiers which are currently being developed.

Acknowledgements

I would firstly like to thank Gavin Newton for all the help and encouragement of the last three and a big bit years. His patience and good humour were very much appreciated and i'll buy him a Guiness any time. Also thanks to Ken Skeldon for the help and advice and the good company during those late nights in the lab making sensitivity measurements, which in hindsight were worth it in the long run. I would also like to thank Jim Hough for his interest and for giving me the chance to work in the group and for the great opportunities that have resulted. Further thanks to Bryan Barr who helped with the detector over the last few months and Paul McNamara for his help back at the start.

The work presented in this thesis is the continuation of over 20 years of development of the prototype detector. It would therefore not have been possible without the work of the many who have worked in the switch room before. A special acknowledgement goes to them.

Also I thank the other members of the group for useful discussions, advice and distractions. Also Prof. Byer, Eric Gustafson and all at Stanford for the enjoyable and interesting couple of months I spent there.

I must also thank my family and friends for the help and support over the last few years. This thesis is dedicated to the memory of my two Grannies as their influence on myself and those around me helped make this possible.

Lastly I am grateful to those who read over the various drafts of this thesis, Oliver Jennrich, Ken Skeldon, Jim Hough and Gavin Newton.

Preface

This thesis is an account of the work carried out between October 1997 and December 2000 with the Glasgow 10 m prototype interferometric gravitational wave detector and on associated experiments.

Chapter 1 contains a brief introduction to gravitational waves including how they interact with matter and possible sources. This is derived from published literature.

Chapter 2 contains definitions essential to the description of Fabry-Perot cavities. Further an outline of the Glasgow 10 m prototype gravitational wave detector is given. The equations presented can be found in many books on optics.

Chapter 3 describes the injection locked Nd:YAG laser system built as the new light source for the interferometer. The properties of this laser system are presented. This work was carried out under the supervision of Dr. G. Newton.

Chapter 4 describes experiments to stabilise and measure the frequency properties of the injection locked laser. These experiments used the two Fabry-Perot cavities in the 10 m interferometer as a frequency reference and analyser. These experiments were performed mainly with Dr. K. Skeldon and Dr. G. Newton.

Chapter 5 describes measurements of the frequency noise around the relaxation oscillation frequency of a Non-Planar Ring Oscillator. This again used the Fabry-Perot cavity in one arm of the detector as a frequency analyser to improve on previous measurements by almost an order of magnitude. These experiments were performed with Dr. K. Skeldon and Dr. G. Newton.

Chapter 6 describes experiments to measure the displacement sensitivity of the interferometer using the new laser system. Experiments to measure the

thermal noise of a heavily damped test mass were then performed. The sensitivity measurements were made mainly with Dr. K. Skeldon, Dr. G. Newton and Mr. B. Barr.

Chapter 7 describes a new technique for calibrating the prototype detector using photon pressure. This has been suggested as a possible calibration technique in the past but this was the first time the experiment was performed with the detector. This experiment was performed with Dr. K. Skeldon and Dr. G. Newton. The frequency response of the mirror to the radiation pressure force was calculated by Dr. G. Newton.

Chapter 8 describes experiments to measure the properties of optical components for the GEO 600 gravitational wave detector. These measurements were performed under the supervision of Dr. G. Newton. The polarisers were tested at the Laser Zentrum Hanover with the GEO 600 high power laser source with the assistance of Dr. O. Brozek. The experiments on the Brewster prism were performed with Dr. G. Newton, Dr. K. Skeldon and two undergraduate project students: Mr. M. von Gradowski and Miss S. Thieux.

Chapter 9 describes an experiment to measure the phase noise imposed on a laser beam around an electro-optically applied phase modulation. This experiment was performed under the supervision of Dr. G. Newton.

Chapter 10 describes experiments performed during a two month visit to the Ginzton Lab., Stanford University. The laser described was developed from an initial design by Mr. T. Rutherford.

Contents

List of Figures

List of Tables

Chapter 1

Theory

1.1 Introduction

The existence of gravitational radiation was first proposed by Einstein in his theory of General Relativity in 1916 [1]. He predicted that a varying gravitational field emanates from any object with a time varying quadrupole moment. The gravitational field propagates as a wave with a velocity equal to the speed of light.

Observations of the decay in the orbital period of pulsar PSR1913+16 provided the first experimental evidence of the existence of gravitational radiation [2] but direct detection has not yet been achieved. Experiments toward the direct detection of gravitational waves have been advancing since 1960, but due to the very high degree of measurement sensitivity required, they have so far not yielded gravitational wave signals. Developments of new techniques have allowed detectors with the necessary broadband sensitivity to be designed and these are either online or due to come online within the next few years [3, 4, 5, 6]. These detectors should allow direct observations to be made.

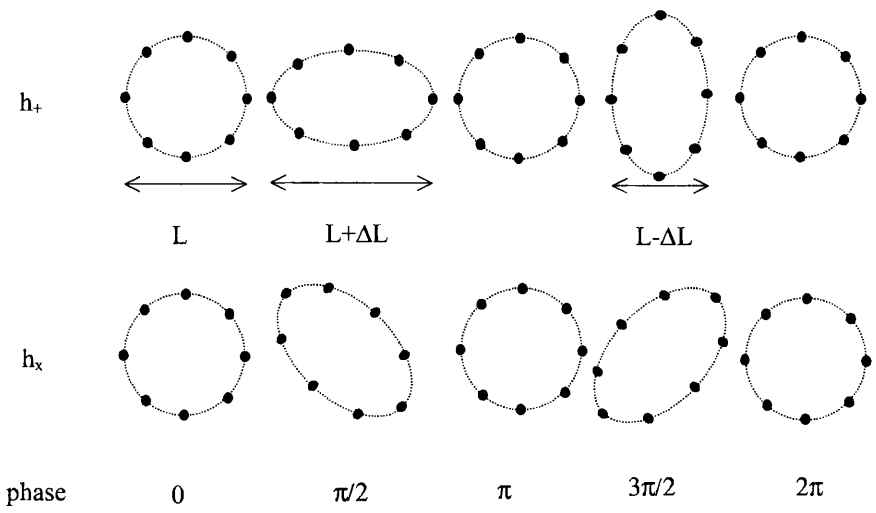

Figure 1.1: *The effect on a ring of test particles of a gravitational wave passing perpendicular to the page. The effect of the two polarisations is shown.*

1.2 Interaction of Gravitational waves with matter

In order to detect gravitational waves it is necessary to understand their generation and how they interact with matter. First it is useful to compare gravitational radiation with electromagnetic radiation. Electromagnetic waves are produced by acceleration of charge and are dipole in nature. For gravitational radiation, conservation of mass prohibits monopole radiation in a similar way to conservation of charge prohibiting monopole electromagnetic radiation. Further, in the case of gravitational radiation, the absence of negative mass prohibits dipole radiation, so it is quadrapole in nature. Sources of gravitational radiation must therefore display a time varying quadropole moment.

Gravitational waves can be split into two polarisations commonly labeled h_+ and $h_\times$. Traditionally the effect on a ring of test particles by the passage of a gravitational wave is used to demonstrate the interaction with matter. As shown in Fig 1.1 a gravitational wave passing perpendicular to the plane of

the page will distort the ring of particles. As the wave passes through one cycle, the ring is contracted in one axis while expanding in the other then vice-versa as the period is completed. The orientation of the axis depends on the polarisation of the wave. The separation of the particles L in the absence of gravitational radiation is increased to a maximum of $L+\Delta L$ and decreased to a minimum of $L-\Delta L$ during the passage of a gravitational wave. A gravitational wave of suitable polarisation can be characterised by an amplitude h given by

$$h = \frac{2\Delta L}{L} \tag{1.1}$$

where h is the strain induced on space.

1.3 Sources of Gravitational Waves

As stated earlier gravitational waves are produced by objects with a time varying quadropole moment. It is interesting to first consider a lab based gravitational wave generator described in [7]. Consider a 10 m long rod, fixed to a pivot such that it can rotate about its centre, with a mass 1000 kg fixed to each end. If the beam rotates about its midpoint at 10 Hz then the system emits gravitational waves with an amplitude $h \sim 10^{-43}$. This means a ruler of length 10 m will display a length variation of order 10^{-42} m during one cycle of gravitational radiation which would be impossible to detect in a lab based experiment. Astrophysical events involve very large masses and accelerations and provide sources which offer the best chance of detection.

1.3.1 Supernovae

Supernovae are categorised as either type I or type II. Type I supernovae are thought to result from the nuclear explosion of a white dwarf star after it has accreted too much matter to remain stable. The core may become a neutron star after the explosion. Type II supernovae are predicted to occur when the

core of a massive star collapses to a compact object sending a shockwave outward through the star causing it to explode. In both cases if the collapse was symmetrical then no gravitational radiation would be produced, however the angular momentum of the star is believed to increase rapidly during collapse which would probably lead to asymmetry and so to the generation of gravitational waves [8]. The amplitude of a gravitational wave emanating from a supernova which emits energy E in the form of gravitational radiation at a frequency f in a time τ has been calculated to be

$$h \approx 5 \times 10^{-22} \left[\frac{E}{10^{-3} M_{\odot} c^2}\right]^{1/2} \left[\frac{1\,\mathrm{kHz}}{f}\right] \left[\frac{\tau}{1\,\mathrm{ms}}\right]^{-1/2} \left[\frac{15\,\mathrm{Mpc}}{r}\right] \tag{1.2}$$

at a distance r from the source [9]. $M_{\odot}$ is the mass of the sun and 15 Mpc is the distance to the Virgo cluster.

1.3.2 Coalescing Binaries

A binary system consists of two stars orbiting about their centre of mass. The rotational period of the binary system decreases as energy is emitted from the system in the form of gravitational waves. In the final few moments before coalescence the rotation frequency increases rapidly and emits a characteristic chirp gravitational wave signal. The strain amplitude of this chirp gravitational wave signal is [9]

$$h \approx 10^{-23} \left[\frac{M}{M\odot}\right]^{5/3} \left[\frac{f}{100\,\mathrm{Hz}}\right]^{2/3} \left[\frac{100\,\mathrm{Mpc}}{r}\right] \tag{1.3}$$

where f is the orbital frequency of the binary system, r is the distance from the earth and M is the chirp mass defined as

$$M = \frac{(M_1 M_2)^{3/5}}{(M_1 + M_2)^{1/2}} \tag{1.4}$$

where M_1 and M_2 are the masses of the two stars. The binary system studied in [2] is a pulsar with a neutron star companion. Its orbital period of 7.75 hours will increase until coalescence occurs in $\sim 3.5 \times 10^8$ years.

1.3.3 Continuous sources

Pulsars and other rotating neutron stars could provide continuous sources of gravitational radiation if the star is non-axisymmetric. The equatorial eccentricity ε defines the asymmetry of the star. An estimate of the strain amplitude resulting from a pulsar is [10]

$$h \approx 6 \times 10^{-25} \left[\frac{f_{rot}}{500\,\mathrm{Hz}}\right]^2 \left[\frac{1\,\mathrm{kpc}}{r}\right] \left[\frac{\varepsilon}{10^{-6}}\right] \tag{1.5}$$

where f_{rot} is the rotational frequency and r is the distance from earth. These continuous sources allow detectors to operate over long integration times and so improve the signal to noise ratio and improve the chance of gravitational wave detection.

Normal modes of neutron stars could provide another continuous source of gravitational radiation. The gravitational radiation would be at too high a frequency for current detectors to see but future developments may allow observation [7]. Recently the r-mode instability of neutron stars [11] has caused considerable interest. The r-mode is a normal mode of a neutron star which is unstable to gravitational radiation. Current estimates indicate that the resulting gravitational wave strain amplitudes will be too small for current detectors but future upgrades may allow detection [12].

1.4 Gravitational wave detectors

There are predominantly two types of gravitational wave detectors, narrow band bar detectors and broadband laser interferometric detectors.

1.4.1 Bar detectors

The development of resonant bar detectors was pioneered in the 1960s by Weber, and work on these continues at several locations worldwide.

A bar detector typically consists of a bar with physical properties such that its fundamental resonant frequency lies in the range 500 Hz to 1.5 kHz generally centred on a frequency where there is an expected source of gravitational radiation. A passing gravitational wave will expand the bar of length l by

$$\delta l \sim hl \tag{1.6}$$

where l is the length of the bar and h is the gravitational wave amplitude. It is not possible to measure this motion directly since a motion sensing transducer will also be affected by the gravitational wave. However if a burst of gravitational radiation has a frequency that matches the resonant frequency of the bar, the then the bar will ring with a decay time dependent on the materials internal Q-factor. This ring becomes a measurable quantity.

The gravitational wave signal is masked by a number of noise sources. Acoustic and vibrational excitation of the mass is reduced by suspending it from vibration isolation stages and placing the bar in a chamber held under vacuum. At room temperatures thermal motion in the mass dominates the gravitational wave induced signal. For this reason the bars of modern detectors are held at temperatures around 100 mK to reduce the thermal noise. The vibration amplitude due to thermal noise is [7]

$$\delta l_{rms} = \sqrt{\frac{kT}{4\pi^2 M f^2}} \tag{1.7}$$

where M is the mass of the bar which is at temperature T. Even at such low temperatures this is approximately 1000 times greater than the amplitude due to gravitational waves. A sudden excitation of the mass at its resonant frequency ω_0 will decay in amplitude with a time constant τ. A thermal excitation takes a time τ to change by its full amplitude. So if the material has large decay time τ or equivalently high internal quality factor Q, then the thermal noise amplitude over timescales which are short in comparison to the decay time τ is small. Typical values of Q for bar detectors are of order 10^6

with decay time $\tau = \frac{2Q}{\omega_0}$ or $200\,s$ for $\omega = 2\pi \times 1000\,\mathrm{Hz}$. A gravitational wave of frequency 1 kHz will change the dimensions of the bar over timescales of 1 ms, allowing its effect to dominate over the thermal noise.

Modern bar detectors operate at very low temperatures. The first of these at Stanford University was damaged in the 1989 earthquake and was shut down. Other detectors have been developed by research groups worldwide; EXPLORER [13] at Cern, Switzerland, ALLEGRO [14] at Louisiana State University, NIOBE [15] in Perth, Australia, AURIGA [16] in Padua, Italy and NAUTILUS [17] in Rome. The best sensitivity was achieved with AURIGA and NAUTILUS was $h \approx 4 \times 10^{-19}/\sqrt{\mathrm{Hz}}$ with a bar temperatures of 250 mK and 100 mK respectively [18].

Recently an experiment to try and measure burst sources of gravitational waves in a data run using all five sensitive bar detectors was performed. The typical sensitivity was $h \approx 5 \times 10^{-22}$ at approximately 1 kHz using the data from all five detectors [19].

1.4.2 Laser interferometric detectors

In the 1970's construction of laser interferometric detectors was begun. The basic operation of these detectors can be understood with reference to Fig 1.2. The two arms of the Michelson interferometer lie perpendicular to each other such that a passing gravitational wave introduces a differential length between the arms. If the recombined light field at the output port of the interferometer is set on a dark fringe, then a gravitational wave is measured as a deviation from this condition.

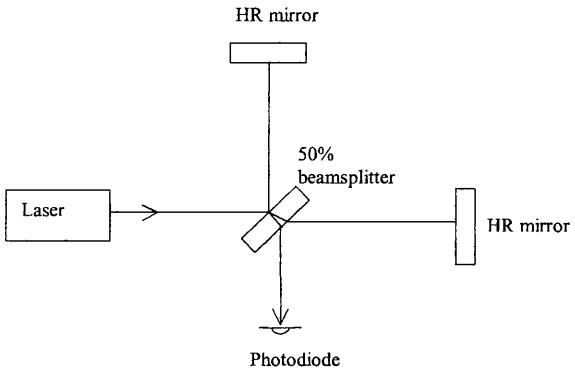

Figure 1.2: *A Michelson interferometer. The gravitational wave increases the length of one arm while decreasing the other and then vice-versa during one period. If the output port is held on a dark fringe then the gravitational wave signal will be observed as a deviation from this condition.*

1.4.3 Detector configurations

The phase shift between the light in each arm of the Michelson interferometer with arm length L is given by

$$\phi = \frac{2\pi}{\lambda} hL \tag{1.8}$$

for a gravitational wave of amplitude h. As the gravitational wave induces a strain in space, the relative phase shift between the light in the arms is increased if the length of the arms is increased. Impracticalities of making very long arms necessitates the use of other schemes to effectively increase the arm length. There are predominantly two methods of achieving this aim; Herriot delay lines and Fabry-Perot cavities.

Delay line interferometer

The delay line interferometer was proposed in the early 1970's. The optical path length in each arm of the interferometer is increased by reflecting the light between two mirrors. The reflected laser beams do not overlap as shown in

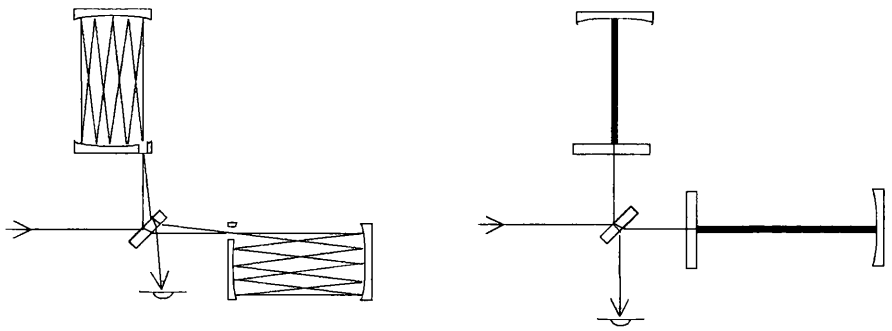

Figure 1.3: *Two methods of increasing the storage time of light in an arm of the Michelson interferometer. The Herriot delay line and Fabry-Perot cavity are shown in the arms of a Michelson interferometer.*

Fig 1.3. At the Max-Planck Institut für Quantenoptik in Garching, Germany, a 30 m mirror separation was used in a delay line Michelson interferometer and up to 90 beams were present in each arm giving an effective optical length of 2.7 km [20]. The disadvantages of this scheme are that large mirrors are required to allow all the individual beams to be separated and sensitivity to scattered light becomes a serious problem. GEO 600 uses a simple delay line with only two passes of the light to produce an effective arm length of 1200 m.

Fabry-Perot interferometer

The use of a Fabry-Perot cavity to increase the effective length of one arm was developed by the Glasgow group in the early 1980's. In this scheme the light builds up in the cavity if the input laser frequency matches a cavity resonant frequency as shown in Fig 1.3. The effective length of the cavity is increased as the light is trapped for some time once it enters the cavity. The advantage of this scheme is that small mirrors can be used as the laser paths are superimposed on each other. The LIGO, VIRGO and TAMA 300 gravitational wave detectors use this configuration.

The Glasgow prototype interferometer uses Fabry-Perot cavities to increase

the length of the arms. The arm length of 10 m is increased to an effective length of $\sim$ 32 km. The Glasgow prototype uses a different configuration to that of Fig 1.3 in that there is no recombination of the light from each arm at the beamsplitter. This will be described in more detail later.

1.5 Noise sources in interferometric Gravitational wave detectors

The gravitational wave is detected by observing a change in the dark fringe power at the interferometer output port. This relies on the fact that the only mechanism for varying the dark fringe power is for a passing gravitational wave to introduce a relative phase shift between the light field in each arm. Other sources of noise can result in a change in the dark fringe power. Some of these can be controlled while others present a fundamental limit to the sensitivity of the detectors.

1.5.1 Seismic noise

If the interferometer mirrors were mounted rigidly to ground then seismic noise would move the mirrors and introduce a relative change in the arm lengths causing a varying dark fringe power. A typical seismic noise displacement spectral density is $\frac{10^{-7}}{f^2}\,\mathrm{m}/\sqrt{\mathrm{Hz}}$ and varies by around an order of magnitude at different sites on the earths surface. To isolate the mirrors from this noise source, each is suspended as part of a multi-stage pendulum [21].

1.5.2 Thermal noise

Thermal noise originates from the random motion of atoms in the mirror mass and suspension wires. The maximum motion is concentrated around the frequencies of the resonant internal modes of the mirror mass, pendulum mode

frequencies of the suspension system and violin mode frequencies of the suspension wires.

As a precursor to a later chapter it is useful to consider the thermal noise of a mirror mass. The thermal noise is resonantly enhanced at the internal mode frequencies of the mirror mass. The mirrors used with the prototype interferometer which have mass 2.8 kg and diameter of 15 cm have dominant internal modes at 23 kHz, 25.4 kHz, 26.1 kHz, 28,7 kHz, 32 kHz and 36 kHz [22]. These are well away from the frequency range of interest for detecting gravitational waves but the tails of the resonance curve for each mode contribute to a low frequency thermal noise background.

The spectral density of displacement due to thermally excited motion from each internal mode is given by [23]

$$x^2(\omega) = \frac{4k_B T\omega_0^2\phi(\omega)}{\omega m[(\omega_0^2 - \omega^2)^2 + \omega_0^4\phi^2(\omega)]} \tag{1.9}$$

where the mirror is of mass m, the internal mode frequency is ω_0 and $\phi(\omega)$ is the mechanical loss of the mode. $\phi(\omega)$ is derived from the complex form of Hookes law

$$F = -k[1 + i\phi(\omega)]x \tag{1.10}$$

and is the phase by which the displacement x lags the driving force. The Q-factor related to the mechanical loss by

$$Q = \frac{1}{\phi(\omega)} \tag{1.11}$$

so from Equation 1.9 the thermal noise far from the internal mode is decreased as the Q-factor is increased. The aim is therefore to develop high Q-factor materials and suspension systems [24, 25, 26].

1.5.3 Shot noise

The gravitational wave signal is derived from the photocurrent of a photodiode examining the dark fringe power at the interferometer output port. There

is a limit to the minimum power fluctuation that can be detected, due to statistical fluctuations in the diode photocurrent. If N photons are detected by the photodiode then there is an error $\sqrt{N}$ associated with this. For a simple Michelson interferometer, the shot noise limited strain sensitivity is

$$h(f) = [\frac{h_{Planck}\lambda}{2\epsilon Pc}]^{1/2}\frac{f}{\sin(\pi f\tau)}/\sqrt{\text{Hz}} \tag{1.12}$$

where h_{Planck} is Planck's constant, P is the power incident on the photodiode of quantum efficiency ϵ, λ is the wavelength of the laser light and τ is the time the laser light is stored in the arm of the interferometer. The shot noise strain sensitivity improves as the detected power increases, so high power lasers are used as light sources for gravitational wave detectors. The laser power cannot however be increased indefinitely as the radiation pressure exerted by the laser light on the interferometer mirrors becomes a limiting noise source. Further the shot noise limited sensitivity is best when $f\tau = \frac{1}{2}$ i.e. when the cavity storage time is half the period of the gravitational wave.

1.5.4 Laser noise

Fluctuations associated with the laser light source for the interferometer can be split into three main catagories; frequency noise, power noise and beam geometry fluctuations.

Frequency noise is due mainly to the optical path length in the laser cavity changing. In an ideal Michelson interferometer with equal arm lengths and mirror reflectivities, frequency noise is common to both arms and produces no change in power at the output port. In real interferometers however, small differences in the optical properties (e.g. the length) of each arm make frequency noise a problem. It can be controlled by using an optical cavity to define the laser frequency properties or locking the laser frequency to an atomic transition.

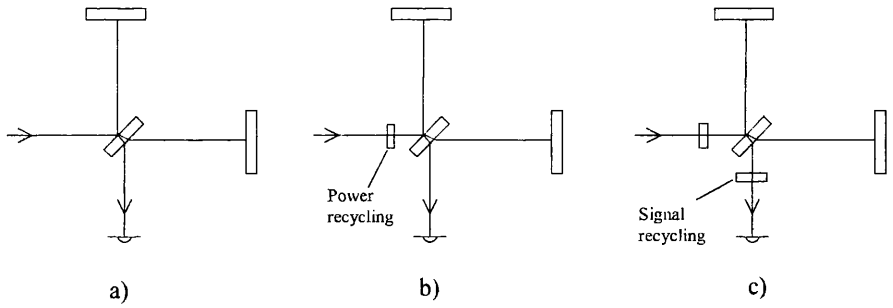

Figure 1.4: *a) A simple Michelson interferometer and b) with a power recycling mirror and c) with power and signal recycling mirrors.*

Power noise of the laser light will couple to the output of the Michelson interferometer. The effect of power noise is minimised by operating the interferometer with a dark fringe at the output port, but if the operating point is slightly offset from the null, some coupling is evident. Power noise can be controlled by sampling a small amount of the laser light on a photodiode and using a feedback system to control the laser power.

For a TEM_{00} laser beam, geometry fluctuations can be considered as higher order spatial modes contaminating the TEM_{00} mode. These changes can lead to varying interference and cause spurious output signals from the interferometer. Beam geometry fluctuations can be attenuated by using a resonant Fabry-Perot cavity or a single mode optical fibre to remove high order spatial modes from the laser beam.

1.5.5 Recycling techniques

Recycling techniques can be understood with reference to Fig 1.4. Under normal operating conditions when the output is at a dark fringe the laser power returns toward the laser. In the early 1980s it was suggested that this light could be sent back into the cavity by placing a further mirror between the laser and the beam splitter [27]. This power recycling mirror increases the power

at the beamsplitter without increasing the power of the laser. To increase the sensitivity further the technique of signal recycling was developed [28]. A gravitational wave introduces phase modulation sidebands to the laser field in the interferometer. The main laser field remains in the interferometer since the output port is held at a dark fringe. However, a fraction of the power containing gravitational wave induced sidebands exits at the output port. A signal recycling mirror placed at the output port sends the light field containing the sideband information back into the interferometer and can resonantly enhance this signal. When both power and signal recycling mirrors are used, a dual recycled interferometer is made. This technique has been demonstrated on an operational prototype gravitational wave detector [29].
Subsequently the technique of resonant sideband extraction [30] was developed to allow Fabry-Perot armed interferometers with storage times much greater than the gravitational wave period to be used. In this configuration a mirror at the output port allows the gravitational wave induced sidebands to leak out from the interferometer while the optical carrier resonates. This technique will be used in the planned LIGO II detector.

1.6 Conclusions

The nature and generation of gravitational waves has been discussed. Possible sources of gravitational radiation and the detectors designed to try to detect them have been outlined.

Chapter 2

The Glasgow 10 m prototype gravitational wave detector - an overview

2.1 Introduction

The Glasgow 10 m prototype gravitational wave detector was first constructed in the late 1970's. Since the first measurements were performed, there have been numerous upgrades to improve the sensitivity to levels where it became feasible to build large scale detectors to achieve higher levels of sensitivity to gravitational radiation.

The aim of this chapter is to provide definitions which are essential in the discussion of optical cavities and to give an overview of the prototype detector on which subsequent chapters will develop.

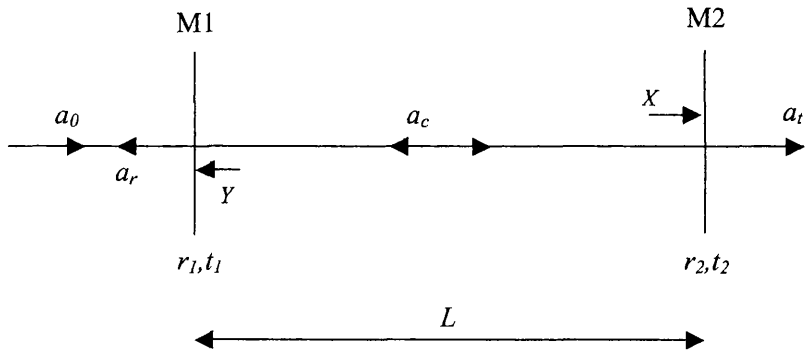

Figure 2.1: *A Fabry-Perot cavity.*

2.2 Optical cavities

Several key properties of optical cavities need to be defined. Consider a Fabry-Perot cavity of length L shown in Fig 2.1, whose two mirrors have amplitude reflectance and transmitance coefficients of r_1, t_1 and r_2, t_2 respectively. It is assumed that there are no absorption losses so $r_1^2 + t_1^2 = 1$ and $r_2^2 + t_2^2 = 1$. If laser light of amplitude a_0 is incident on mirror M1 then the amplitude a_c of light circulating in the cavity and the amplitude a_t transmitted through mirror M2 can be calculated. At point X the amplitude of the circulating field in the cavity is given by

$$a_{c,X} = a_0 t_1 \sum_{n=0}^{\infty} (r_1 r_2)^n e^{-ik(2n+1)L} \tag{2.1}$$

which is equivalent to

$$a_{c,X} = \frac{a_0 t_1 e^{-ikL}}{1 - (r_1 r_2) e^{-2ikL}} \tag{2.2}$$

given that

$$\sum_{n=0}^{\infty} m^n = \frac{1}{1-m} \text{ for } |m| < 1. \tag{2.3}$$

The amplitude of the light transmitted through mirror M2 is then given by

$$a_t = a_{c,X} t_2. \tag{2.4}$$

Converting this to the transmitted intensity gives

$$I_t = \frac{I_0 (t_1 t_2)^2}{(1 - r_1 r_2)^2 + 4(r_1 r_2) \sin^2(kL)} \tag{2.5}$$

which is a maximum when $kL = q\pi$ meaning that

$$\nu = \frac{qc}{2L} \tag{2.6}$$

for maximum transmission. The maximum transmitted intensity depends on the relative values of r_1, t_1 and r_2, t_2 assuming no absorption losses.

An expression for the amplitude of light returning from the input cavity mirror a_r can be derived. This is a sum of the light directly reflected from the input mirror and that transmitted from the cavity through the mirror. Considering first the intra-cavity amplitude of the light at point Y in Fig 2.1, the circulating field is the sum of an infinite series

$$a_{c,Y} = \frac{a_0 t_1}{r_1} \sum_{n=0}^{\infty} (r_1 r_2)^{n+1} e^{-ik2(n+1)L} e^{i\pi} \tag{2.7}$$

or

$$a_{c,Y} = -\frac{a_0 t_1}{r_1} (r_1 r_2) e^{-2ikL} \sum_{n=0}^{\infty} (r_1 r_2 e^{-2ikL})^n \tag{2.8}$$

which using Equation 2.3 gives

$$a_{c,Y} = -\frac{a_0 t_1}{r_1} \frac{(r_1 r_2) e^{-2ikL}}{1 - (r_1 r_2) e^{-2ikL}}. \tag{2.9}$$

The total return field is then given by

$$a_r = a_0 r_1 + a_{c,Y} t_1 \tag{2.10}$$

which when converted to intensity gives an expression for the return intensity dependent on the value of the factor $2kL$. The maximum return intensity when $kL = (q+1)\pi$ is given by

$$I_{r,max} = (a_0 r_1 + \frac{a_0 t_1^2 (r_1 r_2)}{r_1 (1 + r_1 r2)})^2 \tag{2.11}$$

and occurs when the light is anti-resonant with the Fabry-Perot cavity. A minima in the return power when $kL = q\pi$ is given by

$$I_{r,min} = (a_0 r_1 - \frac{a_0 t_1^2 (r_1 r_2)}{r_1 (1 - r_1 r2)})^2 \tag{2.12}$$

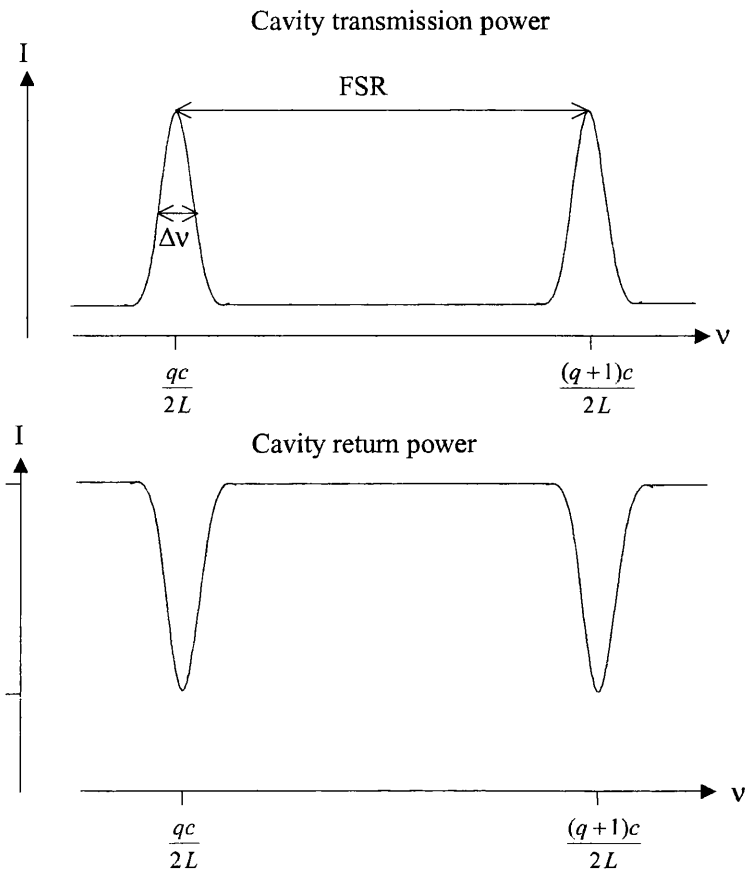

Figure 2.2: *The variation in intensity transmitted through and returning from the cavity as the laser frequency is tuned through cavity resonant frequencies.*

and occurs when the light resonates in the cavity. The variation in the intensity of the light transmitted from the cavity as the laser frequency moves through a cavity resonant frequency takes the form of an Airy function described by Equation 2.5 and shown in Fig 2.2.

The spacing of the resonances or spacing in the maxima of the Airy functions is the free spectral range defined as

$$\mathrm{FSR} = \frac{c}{2L} = \frac{c}{p} \tag{2.13}$$

where c is the speed of light and p is the round trip optical path length. The

visibility is defined here to be

$$V = 1 - \frac{I_{min}}{I_{max}}. \tag{2.14}$$

In the simple case outlined here this is determined by how well matched the mirrors are, analogous to impedance matching in electrical circuits. If the mirrors are identical then in the absence of mirror losses no power returns from the cavity when the light resonates in the cavity. In practice absorption losses in the mirror substrates and modematching considerations in the Gaussian optics case, complicate the evaluation of V.

To describe the resonance, a property of the Fabry-Perot cavity called the finesse F is defined. Resonances are characterised by their quality factor Q defined as

$$Q = 2\pi \frac{\text{energy stored in oscillator}}{\text{energy lost/cycle}} \tag{2.15}$$

and the higher the Q the less loss is associated with the oscillation. In the case of a Fabry-Perot cavity, since the energy lost during one cycle of light is very small in comparison to the stored energy in a given mode, Q is typically very large. The Q of the resonance in an optical cavity can be better defined in terms of the finesse F where

$$Q = nF \tag{2.16}$$

and n is the number of wavelengths in a round trip length p. In the case of a high finesse cavity where $r_1 \approx r_2 \approx 1$, the finesse F can be approximated as

$$F = \pi \frac{(r_1 r_2)^{\frac{1}{2}}}{1 - (r_1 r_2)}. \tag{2.17}$$

The finesse gives an indication of the loss in a Fabry-Perot cavity. In general high finesse cavities have highly reflective mirrors. The cavity storage time τ_s is defined to be the time taken for the intra-cavity intensity I_c to decay to $\frac{I_c}{e}$, if the input intensity I_i is suddenly reduced to zero. It is related to the finesse by

$$\tau_s = \frac{F}{\pi \times \text{FSR}}. \tag{2.18}$$

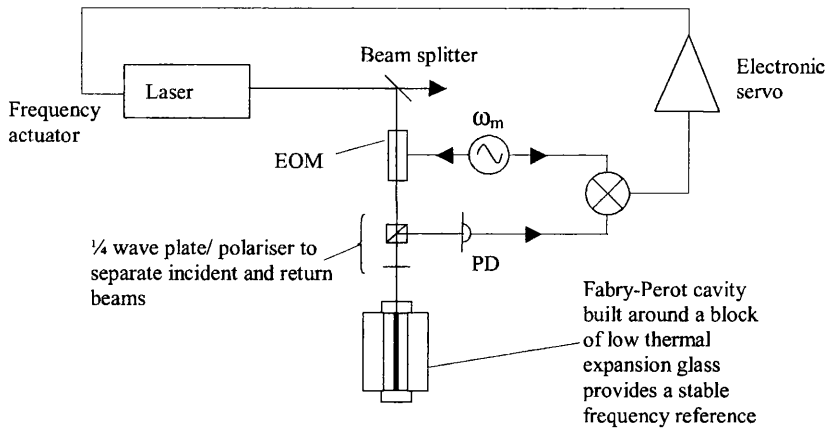

Figure 2.3: *A simple rf-reflection locking setup. Here the laser frequency is locked to the resonant frequency of the Fabry-Perot cavity.*

The effective optical length of the cavity can be defined in terms of the finesse and is given by

$$p_{eff} = \frac{F}{\pi} p. \tag{2.19}$$

Using the expression for finesse, the linewidth of the resonance can be defined as

$$\Delta\nu = \frac{\mathrm{FSR}}{F} = \frac{1}{\tau_s \pi}. \tag{2.20}$$

This represents the full width at half maximum of the Airy function describing the resonance.

2.3 Rf reflection locking

In the preceding section the resonance condition of a Fabry-Perot cavity was discussed. The resonance occurs when the frequency of the input laser field satisfies the condition described in Equation 2.6.

The operation of a frequency stabilising servo requires an error signal to be generated which has a linear response to frequency deviations. Several techniques can be used for this purpose [31, 32, 33, 34], although some have advantages

over others. Rf-reflection locking [34] is a way of generating an error signal with the desired characteristics. An rf-locking scheme is shown in Fig 2.3, where the resonant frequency of the Fabry-Perot cavity is used to define the frequency of the laser. The laser light is phase modulated at an angular frequency ω_m before entering the cavity. A modulation frequency of greater than 5 MHz is typically used, because the laser intensity fluctuations are generally shot noise limited above this frequency. The phase modulated light can then be described by

$$E(t) = E_0 e^{-i(\omega t + \beta sin\omega_m t)} \tag{2.21}$$

or equivalently

$$E(t) = E_0(J_0(\beta)e^{-i\omega t} + J_1(\beta)e^{i(\omega t+\omega_m t)} - J_1(\beta)e^{i(\omega t-\omega_m t)}$$
$$+J_2(\beta)e^{i(\omega t+2\omega_m t)} - J_2(\beta)e^{i(\omega t-2\omega_m t)}...etc \tag{2.22}$$

where $J_n(\beta)$ are the Bessel functions of the first kind. For $\beta < 1$ only $J_0(\beta)$ and $J_1(\beta)$ need be considered. The laser frequency spectrum therefore consists of a carrier at angular frequency ω and sidebands at $\omega \pm \omega_m$. If the Fabry-Perot cavity linewidth $\Delta\nu \ll \frac{\omega_m}{2\pi}$ and the angular laser frequency ω matches a cavity resonant frequency ω_0, then the sidebands lie outside the cavity linewidth and they are reflected from the input mirror.

The phase of the field leaking from the cavity lags that of the directly reflected light, the phase difference passing through 90^o on resonance. If the incident light field is not resonant the the phase difference is greater or less than 90^o depending whether $\omega < \omega_0$ or $\omega > \omega_0$. The return field from the cavity therefore can be written as the sum of the reflected and leakage fields. The reflected field

$$E_r(t) \;\; \alpha \;\; E_0(J_0(\beta)e^{-i\omega t} + J_1(\beta)e^{i(\omega t+\omega_m t)} - J_1(\beta)e^{i(\omega t-\omega_m t)}) \tag{2.23}$$

and the leakage field which has no component at ω_m

$$E_t(t) \;\; \alpha \;\; E_c(J_0(\beta)e^{-i\omega t}e^{i\phi} \tag{2.24}$$

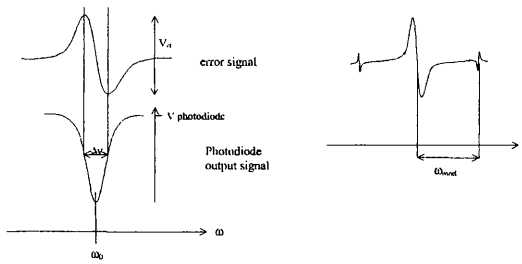

Figure 2.4: *Left side - The error signal produced from rf-reflection locking around the cavity resonant frequency ω_0. Also shown is the corresponding low frequency photodiode output. Right side - The error signal to the modulation frequency from the cavity resonant frequency ω_0. The shape of the error signal gives a very wide locking range of twice the modulation frequency.*

if a small modulation index β is considered and ϕ is the phase offset from resonance. The photocurrent from a photodiode detecting the return light therefore has a component at the modulation frequency ω_m which is proportional to

$$-E_t J_0(\beta) E_c J_1(\beta) \sin(\phi) \tag{2.25}$$

or

$$-E_t J_0(\beta) E_c J_1(\beta)(\phi) \tag{2.26}$$

for small offset from resonance. Demodulation of the diode photocurrent at the modulation frequency generates a signal of the form shown in Fig 2.4. This signal has a zero crossing at the resonance allowing a servo system to be generated to lock to this point and is linear for small phase offsets. Rf reflection locking has the added advantage that it gives a very wide locking range. An error signal is produced with a full width of twice the modulation frequency. This allows the servo to aquire lock as long as the laser frequency is within the modulation frequency from the cavity resonant frequency.
The transfer function of the frequency discriminator T_{rf} with rf-reflection locking can be approximated by considering the gradient of the error signal around

the locking point given by

$$T_{\text{rflock}} = \frac{V_{rf}}{\Delta\nu} \tag{2.27}$$

where $\Delta\nu$ is the cavity linewidth and V_{rf} is the peak-peak signal from the demodulator. This locking technique is widely used and has the advantage of being relatively immune to intensity noise in the laser light since the detected signals are at frequencies where the laser intensity noise is shot noise limited.

2.4 Detector configuration

The basic configuration of the Glasgow prototype gravitational wave detector is shown in Fig 2.5. The two cavities are labeled primary and secondary and this notation will be used from here onwards. The Fabry-Perot cavities comprise two highly reflecting mirrors and have a finesse of approximately 10,000. The mirrors have a mass of 2.8 kg and are 12.7 cm in diameter. The inboard mirrors (those closest to the beamsplitter) are flat while the outboard mirrors have a radius of curvature of 15 m. The high finesse gives an effective cavity length of around 32 km and a linewidth of around 1.5 kHz. The two cavities are contained in a vacuum system.

Light from a Nd:YAG laser with a wavelength of 1064 nm enters the final injection optics chain through a single mode optical fibre. This reduces beam-geometry fluctuations ensuring an approximately TEM_{00} mode enters the interferometer. The injection optics comprise mode matching lenses, two Faraday isolators [35] and a $LiNbO_3$ electro-optic modulator [36]. The light then enters the vacuum system and a 50:50 beam-splitter sends half the light towards each Fabry-Perot cavity. The light returning from the cavity is extracted from the incident beam by a suspended quarter-wave plate and polariser assembly.

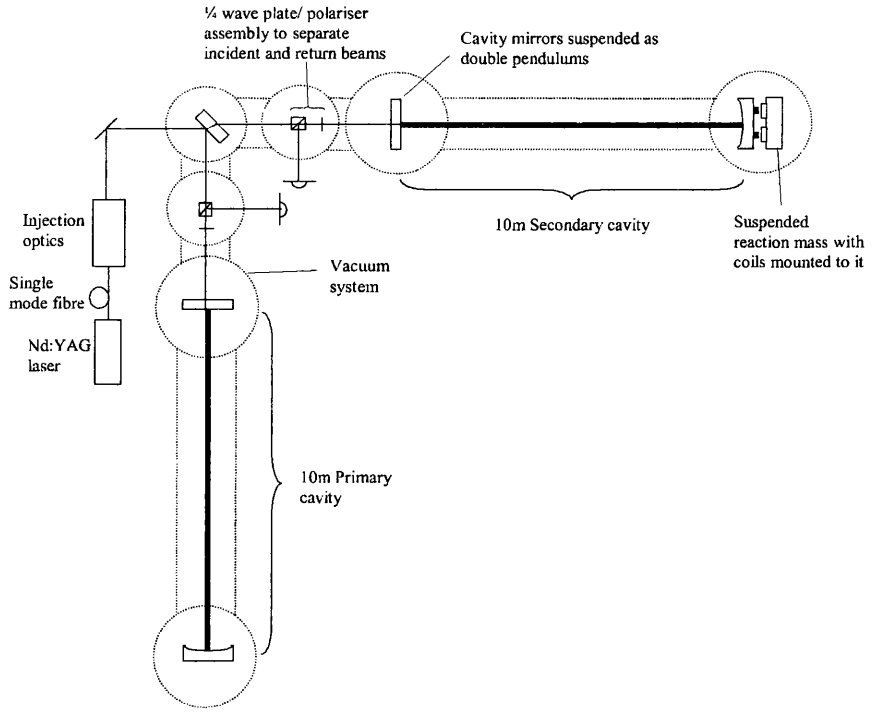

Figure 2.5: *A schematic of the prototype detector.*

2.4.1 Primary cavity

The primary cavity is used as a reference to define the frequency characteristics of the laser. An optical cavity used as a frequency reference must have fractional length changes $\frac{\Delta L}{L}$ less than the required fractional frequency fluctuations $\frac{\Delta \nu}{\nu}$ at a given frequency. For this reason the cavity mirrors are in part isolated from external noise sources. Fig 2.6 shows the mirror isolation system [37, 38]. Each mirror is suspended from a leaf spring as a double pendulum to give isolation from seismic noise. Added isolation is achieved by mounting the base plate on a series of lead-rubber stacks. The double pendulum reduces the spectral density of displacement of the mirror to $\sim \frac{10^{-7}\,\mathrm{m}}{f^4}$. The intermediate mass motion is damped via a coil and magnet arrangement for tilt, rotation and longitudinal motions. The cavity is contained in a vacuum chamber with a pressure of $\sim 10^{-4}$mb to reduce air refractive index fluctuations and limit

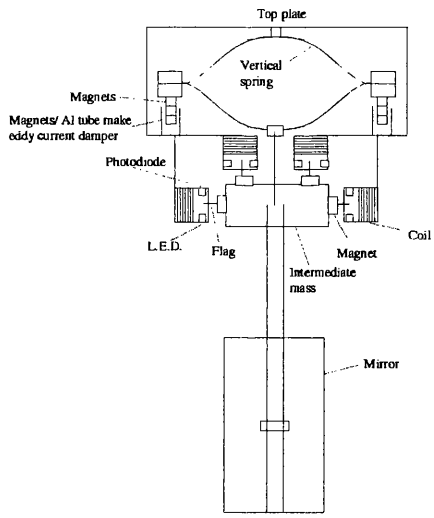

Figure 2.6: *The suspension system that isolates each mirror from seismic noise.*

the effect of acoustic noise.

With these isolation techniques, models of the suspension system predict that each mirror has a motion of $< 10^{-19}\,\mathrm{m}/\sqrt{\mathrm{Hz}}$ at frequencies above 400 Hz [37, 39]. The primary cavity therefore permits frequency stability to a level of $\sim 10^{-5}$ Hz above 400 Hz in an ideal situation given an adequate stabilisation servo system and the absence of any other noise sources.

2.4.2 Secondary cavity

The passage of a gravitational wave affects the length of the primary cavity and thus changes the laser frequency. To analyse this change in laser frequency and extract the information on the gravitational wave signal, a frequency analysing secondary cavity is used to measure the change.

The Fabry-Perot cavity is of similar finesse and the mirror suspensions are identical to the primary cavity. The difference is the inclusion of a suspended reaction pendulum shown in Fig 2.7. This is situated behind one mirror mass and has coils mounted to it. These coils combined with magnets bonded to

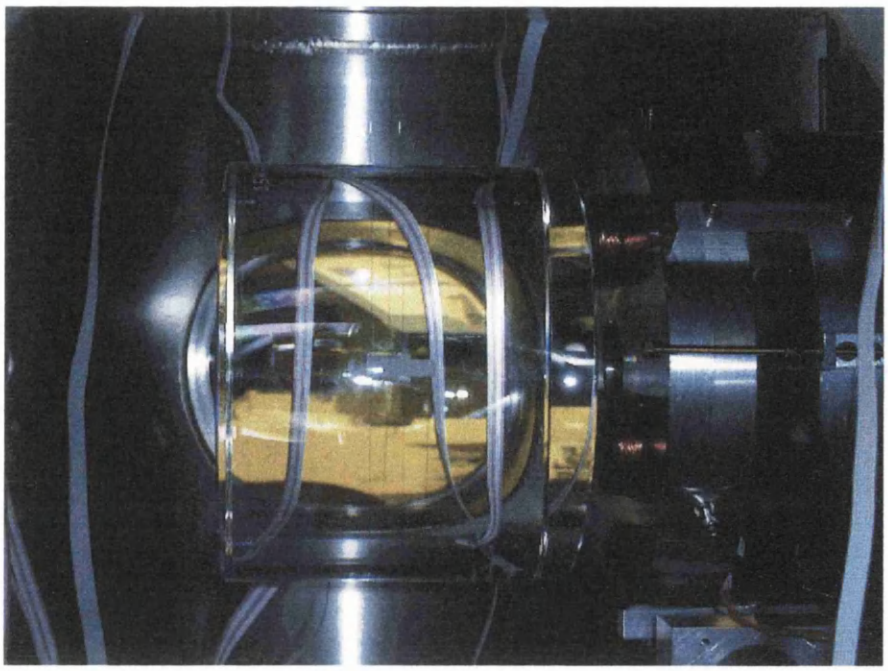

Figure 2.7: *The secondary outboard mirror with the reaction pendulum situated behind it. The red coils are clearly visible on the reaction pendulum and act on magnets bonded to the mirror.*

the cavity mirror, allow the cavity mirror to be moved. The cavity length can therefore be changed and locked to the laser frequency by feeding signals to the coils on the reaction mass. Analysis of the current fed to the coils to hold the secondary cavity resonant yields a power spectrum from which to derive the gravitational wave signal.

2.5 Conclusions

Definitions necessary for the discussion of optical cavities have been described and will be referred to later. The basic infrastructure of the Glasgow prototype gravitational wave detector has also been described. The following chapters will discuss in much more detail aspects of laser stabilisation and measurements performed with the interferometer.

Chapter 3

The laser system

3.1 Introduction

The Glasgow 10 m prototype gravitational wave detector has operated for around 20 years with an Argon ion laser source at a wavelength of 514 nm [40]. This laser in its commercial form is not suitable for highly sensitive interferometry and servo systems were developed to actively stabilise its frequency and intensity, reducing the noise to a level suitable for gravitational wave detection [41, 42]. Argon ion lasers are very inefficient, and if single frequency operation is enforced, the power output is limited to a few watts. Although coherent addition of Argon ion lasers was demonstrated to achieve higher light powers [43], an alternative reliable and more efficient option was needed for the next generation of detectors.

All large scale interferometric gravitational wave detectors currently being constructed use an infra-red laser source with a wavelength of 1064 nm [44, 45, 46, 47]. This choice was made due to recent development of high power, diode pumped Nd:YAG lasers operating at this wavelength, coupled with the availability of high quality optical components and of coatings for the optics of the interferometer.

Another advantage of using Nd:YAG lasers is the availability of the Monolithic Isolated Single mode End pumped Ring (MISER) laser often called a Non Planar Ring Oscillator (NPRO) [48], an extremely low noise, single frequency, but relatively low power Nd:YAG laser. These low noise lasers can be amplified in a Master Oscillator Power Amplifier (MOPA) or used to injection lock a high power oscillator.

A new laser system was required to convert the 10 m prototype to operate using infra-red light. An injection locked Nd:YAG laser source was assembled and characterised allowing tests to be performed on optical components and development of techniques for the British-German gravitational wave detector GEO 600.

3.2 The slave laser

A laser head was obtained on loan from the Ginzton Laboratory at Stanford University which consisted of a Nd:YAG crystal and copper cooling block [49]. A pumping scheme was developed using two water cooled OPC-A020 pumping diodes, each emitting 20 W.

A laser diode emits a highly divergent beam due to the extremely small size of the diode junction. The 42° divergence of the laser diodes output was reduced to 4° with a cylindrical lens and illuminated the central third of the Nd:YAG crystal as shown in Fig 3.1. Any light not absorbed by the Nd:YAG on its first pass was reflected back by a gold coated slide to ensure efficient usage of the available pump power. The copper housing provided cooling to counter the heating of the crystal which results from absorption of the pumping light. A thin layer of indium foil improved the heat flow between the Nd:YAG and copper and helped relieve any mechanical stress on the crystal.

The crystal has Brewster angled ends which polarise the laser output and eliminate the need for anti-reflection coatings. The angled input window also

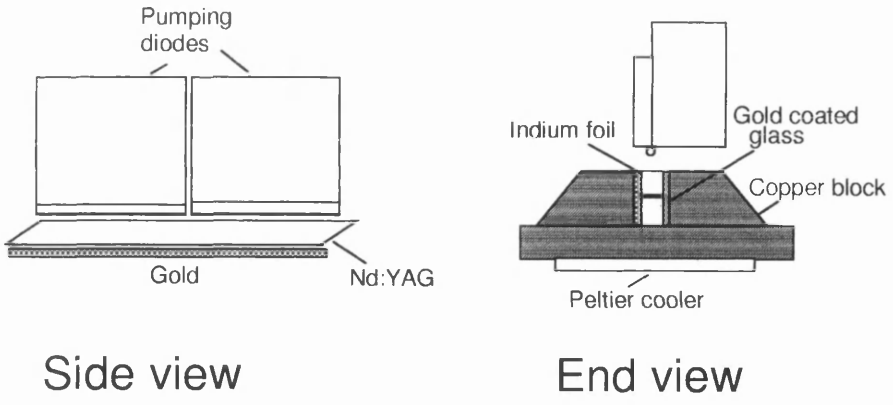

Figure 3.1: *Laser head and pumping scheme. Nd:YAG is pumped by two 20 W water cooled diode arrays.*

refracts the incident laser field producing a zig-zag mode pattern in the crystal. The zig-zag pattern maximises the overlap of the laser mode and the pumped region so utilising as much gain as possible and maximising the output power.

3.2.1 Thermal lensing

Cooling the Nd:YAG on two opposite faces creates a thermal gradient producing a thermal lens in the crystal. The resulting thermal lens is dominant in the direction of heat flow. To find the focal length of this thermal lens, a high reflecting mirror and output coupler, both of which were flat, were placed 22 cm apart and the gain medium centred between them. In this configuration the cavity can be approximated as shown in Fig 3.2. There is a slight reduction in length ΔL due to the optical path length in the Nd:YAG crystal. The size of the waist w_0 created at each mirror and focal length f of the thermal lens are related by

$$f = \frac{d^2 + \frac{\pi^2 \omega_0^4}{\lambda^2}}{2d} \tag{3.1}$$

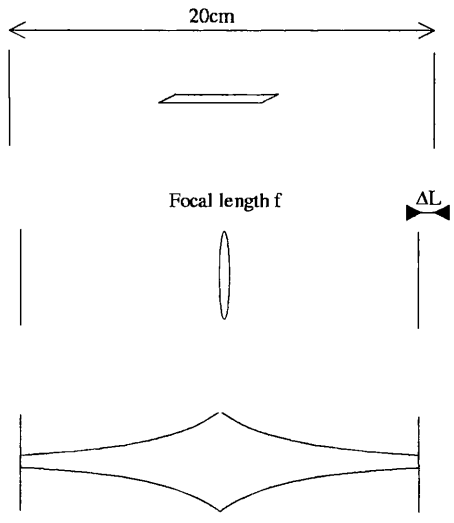

Figure 3.2: *Simplified laser cavity for use in thermal lens calculation.*

where d is the distance from lens to mirror. The laser output beam profile was characterised using a scanning slit profiler, and using the relation

$$w(z) = w_0\sqrt{1 + \left(\frac{\lambda z}{\pi w_0^2}\right)^2} \tag{3.2}$$

where z is the distance from the output coupler, the size of the waist w_0 formed at the flat output coupler was calculated [50]. This calculated waist size w_0 then gives the focal length of the lens from Equation 3.1.

In fitting the laser output to a standard Gaussian beam expansion, it was assumed that the beam was a diffraction limited fundamental mode. The thermal lens focal length was found to be $f = 7\,\text{cm}$ with 25 A of pump diode current. The focal length $f = 7\,\text{cm}$ is a factor of ~ 10 stronger than the lens effect in the perpendicular dimension. Due to this dominance, the lens can be approximated as cylindrical.

The output wavelength of the diode can be tuned by varying its temperature via its cooling water, with a tuning coefficient of $\approx 0.3\,\text{nm/°C}$. The output

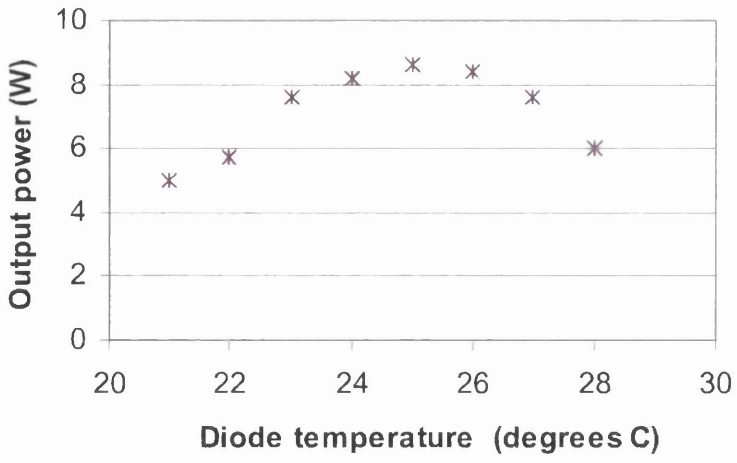

Figure 3.3: *Variation of output power with diode temperature. Maximum power is produced with a diode temperature* T = 25°C.

power with diode temperature is shown in Fig 3.3 for a diode current of 25 A. The optimum output power was obtained with a diode temperature of 25°C. It is at this temperature that the best overlap of pump and absorption wavelengths occur.

3.2.2 Characterisation of the laser

With the approximate value of thermal lens known, a cavity was designed to test the performance of the laser. A 1 m radius of curvature high reflecting mirror and a flat output coupler were placed 30 cm apart with the gain medium centred between them. As shown in Fig 3.4 the optimum output power was 8.6 W in a multi-axial TEM_{00} mode. This was achieved with an output coupling of 10 % and 31 W of pumping power. More pumping power was available however to maintain the diodes lifetime they were never run at full power. The threshold pumping power was 5 W and the slope efficiency $\frac{dP_{out}}{dP_{pump}} = 0.34$ where

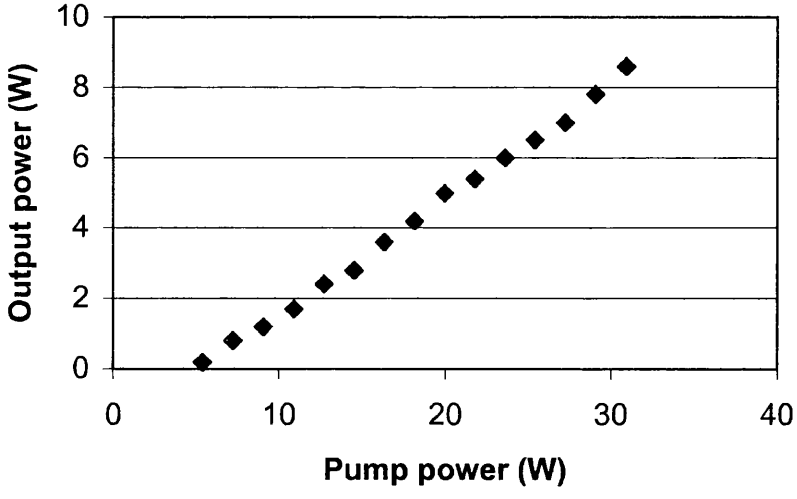

Figure 3.4: *Output power vs pumping power for linear cavity*

P_{out} is the laser output power and P_{pump} is the pump power. TEM_{00} mode operation was verified using a wideband photodiode and rf spectrum analyser: a system which could be used to detect amplitude fluctuations to a frequency of 1.8 GHz. Beating between the axial modes could be clearly seen spaced by $\sim$ 500 MHz: the free spectral range of the cavity. Transverse modes would be observable as smaller peaks clustered around the axial modes but were not observed. The M^2 of the output, defined as approximately the factor by which the beam divergence exceeds the diffraction limited divergence, was measured to be 1.34 in the direction of the dominant thermal gradient and 1.7 in the perpendicular direction.

To characterise the laser some key properties must be determined. Following the notation of Koechner [51] definitions of several parameters of the Nd:YAG crystal and laser are required. The small signal single pass gain is given by

$$G = e^{g_0 l} \tag{3.3}$$

where l is the path length of the laser mode in the pumped part of the crystal

and g_0 is the small signal single pass gain coefficient. The laser mode in the pumped region of the crystal has volume $V = Al$ where $A \approx 4w_x w_y$ is the mode cross sectional area. The saturation intensity I_{sat} is the light intensity passing through the gain medium required to reduce the small signal single pass gain coefficient to $\frac{g_0}{2}$ and values between 2kW/cm^2 and 2.9kW/cm^2 are quoted for Nd:YAG [52]. Several efficiency parameters are also defined; η_q is the quantum efficiency, the fraction of atoms excited to the highest level that relax to the upper laser level; η_s is $\frac{\lambda_{pump}}{\lambda_{laser}}$ called Stokes factor which represents the fundamental limit to laser efficiency; η_B is the efficiency of the pump region-laser mode overlap; η_a is the fraction of pump light actually absorbed by the Nd:YAG so $P_{abs} = \eta_a P_{pump}$.

Using these variables, the small signal single pass gain coefficient

$$g_0 = \frac{\eta_q \eta_s \eta_B P_{abs}}{I_{sat} V} \tag{3.4}$$

and so

$$\ln G_0 = g_0 l = \frac{\eta_q \eta_s \eta_B \eta_a P_{pump}}{I_{sat} A} = K P_{pump} \tag{3.5}$$

where the constant K includes all efficiency factors and constants for the laser. Assuming the thermal lens of the gain medium found previously the mode volume in the gain medium was calculated and the mode /pump volume ratio η_B was estimated to be ~ 0.6 though this is difficult to verify exactly. The pump absorption efficiency η_P was calculated based on an absorption coefficient of $\alpha = 12\,\text{cm}^{-1}$, $\eta_q = 0.95$ for Nd:YAG pumped at 808 nm and $\eta_s = 0.76$. Using these values $g_0 l$ is found to be $\sim 0.4 \pm 0.15$. The large error is due to the approximation of mode size in the gain medium and the difficulty in calculating η_B.

The losses of the laser crystal were found by directing a probe beam through it and measuring the attenuation. The single pass fractional power loss was found to be 0.03. It can be assumed that this is the dominant intra-cavity loss, so the cavity loss factor L is 0.06 since the crystal is double passed on every

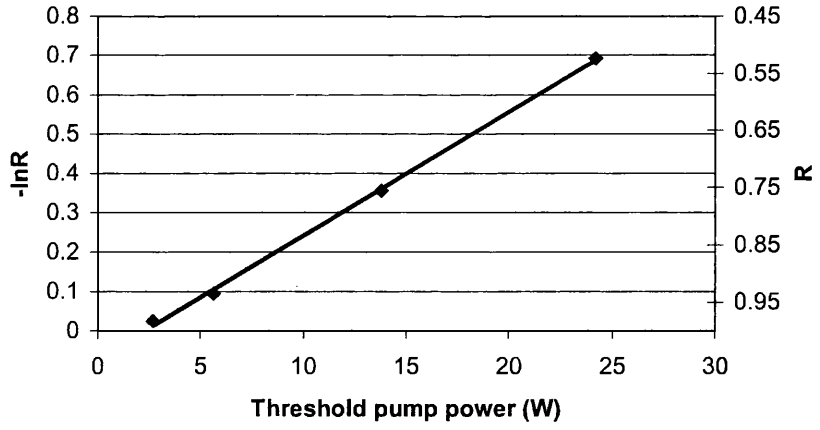

Figure 3.5: *Variation of threshold pumping power with -ln R where R is power reflectivity of output coupler. The gain is derived from the gradient and the internal loss from the -lnR axis intercept.*

round trip.

The output power of the laser is then given by

$$P_{out} = T(\frac{2g_0 l}{T+L} - 1)\frac{I_{sat}A}{2} \tag{3.6}$$

where T is the transmission of the output coupler. Given the size of the error associated with $g_0 l$ it is difficult to predict the expected output power from the laser exactly, although assuming a mode size as used in earlier calculations, several watts would be a reasonable estimate.

Fig 3.5 shows how the threshold pump power varies with output coupling. The analysis of Findlay-Clay [53] shows that the threshold pump power P_{TH} is related to the power reflectivity of the output coupler R by

$$-\ln R = 2KP_{TH} - L \tag{3.7}$$

where K is the overall efficiency of the laser given by the product of the η factors. From Fig 3.5 the gradient gives $K = 0.031$ so from Eq 3.5 the small signal single pass gain is $e^{0.031P_{pump}}$ which equals $e^{0.49}$ at full pump power. Also

from Fig 3.5 the single pass loss is 0.035. This loss is a combination of scatter losses at each total internal reflection in the Nd:YAG crystal and depolarisation loss. The depolarisation loss is minimised by the dominant one dimensional cooling.

3.3 Injection Locking

3.3.1 Introduction

If a coupling mechanism exists between two oscillators they can become locked together, such that the phase changes of one are followed by the other. The phase lock only occurs if the oscillators are separated in frequency by less than the locking range as given by the Adler equation [54].

The Adler equation has been applied to two independent lasers to show that if a noisy high power laser (slave laser) is coupled to a low noise, low power laser (master laser) by injecting light from the master laser into the slave cavity then the two can become phase locked. The phase lock occurs only if the frequency difference between the two lasers is less than the locking range given by

$$\Delta\nu_{lock} = \frac{T \times FSR \times \eta}{\pi}\sqrt{\frac{P_{master}}{P_{slave}}} \tag{3.8}$$

where light from a master laser of power P_{master} is injected into a free running slave laser with power P_{slave} through an output coupler with transmission T and with a mode matching factor η [55].

The free running slave laser field would normally develop from spontaneously emitted photons from the gain medium. Now the injected master field dominates over the spontaneously emitted photons, and is regeneratively amplified and saturates the slave gain medium such that the injection locked output follows the masters phase fluctuations. In this way the desirable frequency noise properties of the master oscillator can be transferred to the slave [56].

Injection locking is especially useful because a low noise NPRO can be used as the master oscillator to injection lock a noisy high power laser. If the slave laser field can propagate as a running wave (either in a ring cavity or a twisted-mode cavity), injection locking forces the slave laser field into this running wave, and since the NPRO emits a single frequency this is reproduced in the injection locked slave. This removes the need for additional intra-cavity optics to force single frequency, unidirectional operation of the slave laser which would reduce its efficiency. Injection locking has been demonstrated with slave/master power ratios of up to 100/1 and with output powers of up to 30 W [57, 58, 59, 60].

3.3.2 Ring laser cavity

Solid state lasers suffer from spatial hole burning if a standing wave is generated in the laser cavity. If the laser is forced to operate at a single frequency then the standing wave generates regions of high and low electric field intensity in the gain medium. The available but unused gain at the nodes of the standing wave can produce parasitic oscillations contaminating the dominant single frequency laser mode. Spatial hole burning in solid state lasers can be prevented by forcing a traveling wave in the laser cavity.

A figure-8 ring laser was constructed which produced a total of 4 W in a TEM_{00} mode. The reduced output power compared to the linear cavity was due to a reduced overlap between the laser mode and pumped region.

The ring laser has two counter-propagating laser fields, and therefore has two output beams, each with approximately equal power emerging from the cavity. The single frequency NPRO output field was modematched and injected into the ring cavity through a 10 % output coupler. The slave laser is relatively unaffected by this injected laser field until the frequency of the light from the NPRO lies within the injection locking range of the frequency of an axial mode in the slave laser. The NPRO field then resonates, is amplified by and

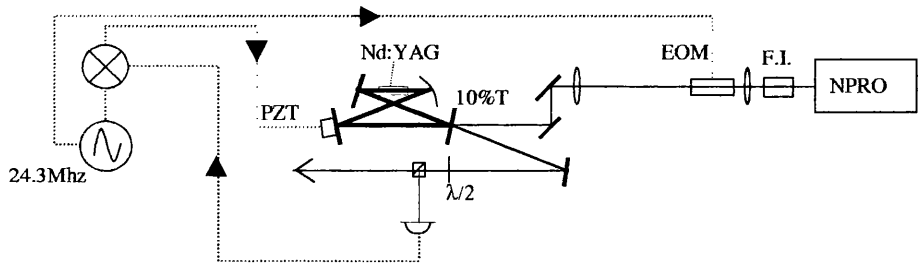

Figure 3.6: *rf-reflection locking setup to hold the slave laser frequency within the injection locking range.*

saturates the slave gain medium. The injection locked slave then follows the phase changes of the NPRO until the injected master oscillation frequency moves outwith the injection locking range. While the laser is injection locked, the laser field in the slave cavity propagates unidirectionally. A servo system is required to hold the slave cavity length resonant with the master laser.

3.3.3 Injection locking schemes

To derive an error signal for locking the slave frequency to master frequency, several different techniques can be implemented. Rf-reflection locking [34], described in Chapter 2, has traditionally been used and generally works very well. The error signal produced is insensitive to intensity noise and using this technique a lock to the slave cavity resonant frequency is obtained.

Rf-reflection locking was used to hold the slave cavity length within the injection locking range as in Fig 3.6 and the injection locked laser emitted $\sim 4\,W$ of single frequency TEM_{00} light. The servo system used is shown in Fig 3.7. The unity gain frequency of 15 kHz was limited by a mechanical resonance of the PZT which actuates a cavity mirror and is required to hold the cavity on resonance.

With the laser injection locked, single frequency operation can be observed with a scanning Fabry-Perot cavity. Fig 3.8 shows the multi-axial mode structure

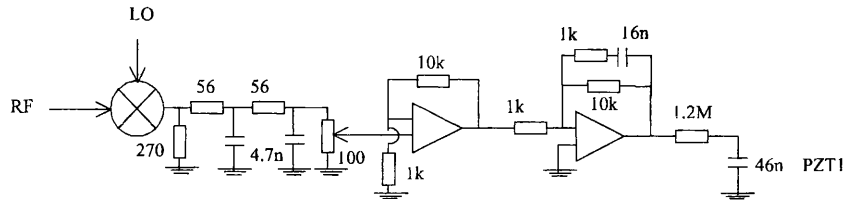

Figure 3.7: *rf-locking servo used to hold slave laser frequency within injection locking range.*

of the laser when not injection locked and the single frequency injection locked output when the servo loop is closed.

There are problems associated with rf-reflection locking as used in injection locking. The phase modulation sidebands are contained in the injection locked laser output field. As will be described later the presence of these sidebands caused problems when the injection locked laser was used as the light source for the 10 m prototype interferometer. This prompted the search for a different injection locking scheme where the output would contain no phase modulation sidebands.

A polarisation spectroscopic technique based on [32] has been shown to generate an error signal of the required form and has successfully been used to injection lock a Nd:YAG laser [61]. This arrangement is complicated by the need for a polarisation analyser in the injection locked output field. Alternatively the phase modulated master field could be injected into the slave cavity through a different cavity mirror, such that the sideband information is not contained in the main output beam. The disadvantage of this scheme is that the injection locking range is reduced, since to maintain overall output power, the mirror would have to be of reasonably low transmitance.

A modulation free, fringe side lock can be used to produce the required error signal. To keep the laser injection locked, the frequency of an axial mode of the slave cavity must be within the locking range of the injected master laser frequency. In most practical cases this locking range of several MHz represents

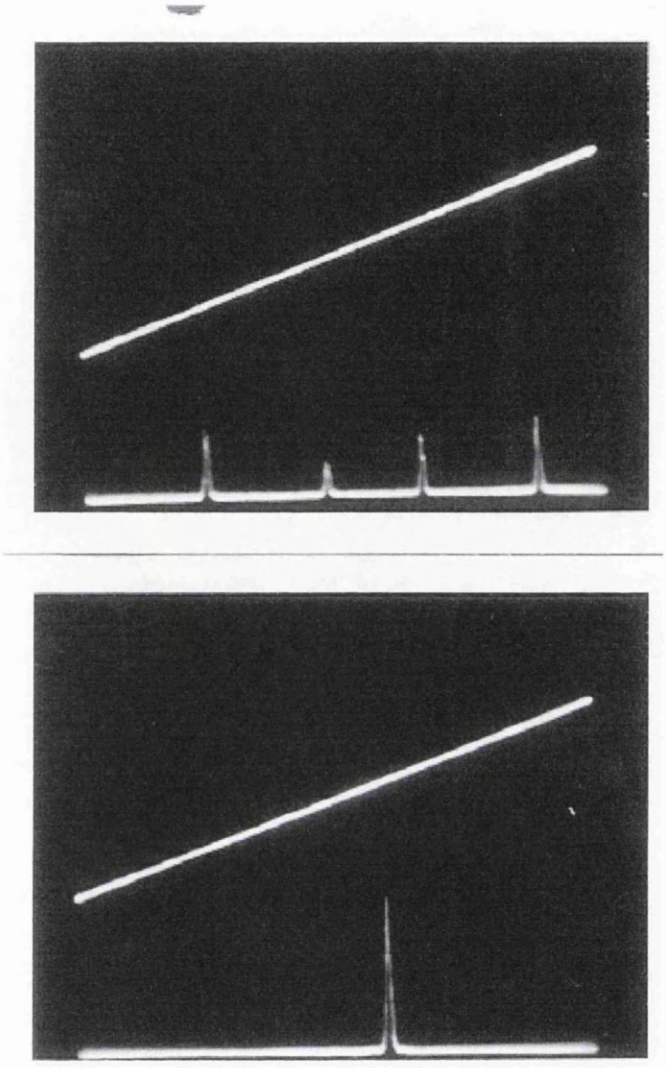

Figure 3.8: *Free running multi-axial mode slave laser and single frequency injection locked laser viewed using a scanning Fabry-Perot optical spectrum analyser. The line in the upper part of each picture shows the ramped scan to a mirror in the Fabry-Perot cavity.*

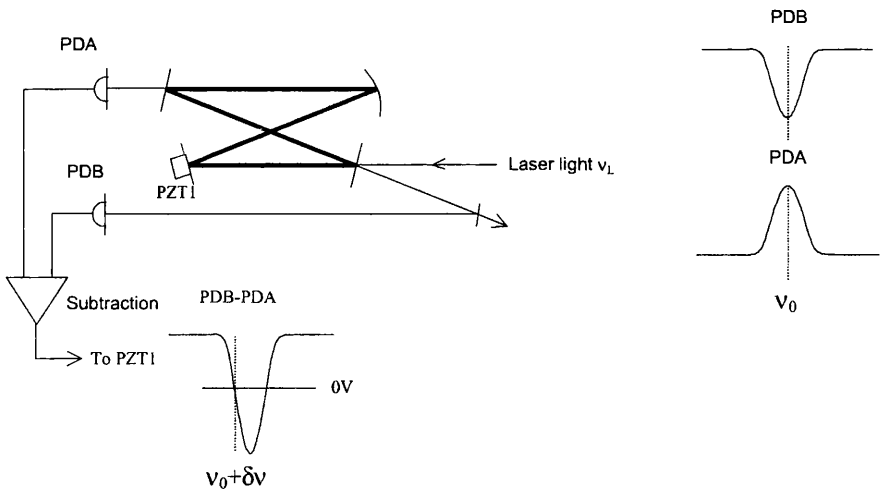

Figure 3.9: *Fringe-side locking schematic to lock the length of a passive Fabry-Perot to a laser. The locking point on the fringe side is offset from the cavity resonant frequency by* $\delta\nu$.

a sizeable fraction of the slave cavity linewidth. A lock to the centre of the slave cavity resonance is therefore not required, as long as an error signal is derived which can be used to counter the large frequency shifts imposed by external noise sources such as acoustic noise.

A fringe side lock scheme is shown in Fig 3.9. In this case, when the incident laser frequency moves through a resonant frequency ν_0 of the cavity, the signal from photodiode A passes through a maxima and photodiode B a minima. Subtraction of the diode outputs can give a signal which passes through zero for some value of $\delta\nu$ the difference between the laser frequency and cavity resonant frequency. This can be used as an error signal and fed to the PZT to lock cavity resonant frequency to the laser frequency. The electronic amplification of each diode photocurrent can be varied to compensate for the different power incident on each photodiode due to the different mirror reflectivities. Further the locking point (value of $\delta\nu$) can be changed by varying the relative amplification.

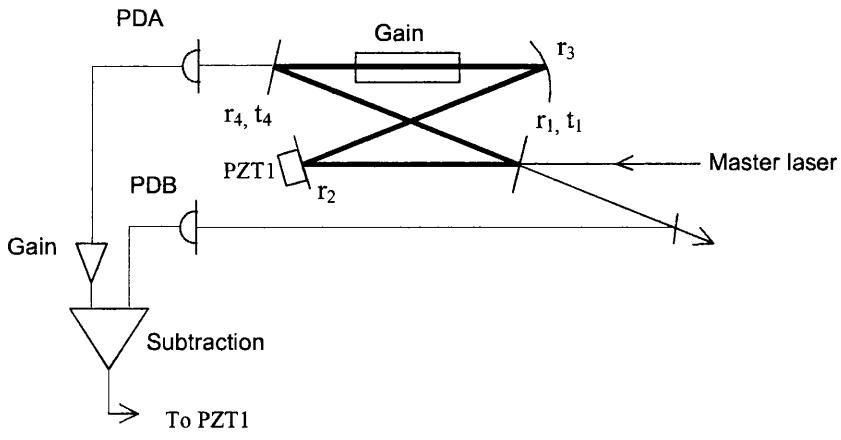

Figure 3.10: *Fringe-side injection locking schematic.*

Consider now the slave laser cavity. If it were single frequency and unidirectional then the laser frequency would be at the value where the round trip loss is lowest. This corresponds to the cavity resonant frequency ν_0 as shown in Fig 3.11. The slave laser cavity linewidth is around 10 MHz, considerably greater than the linewidth of the slaves output field. If the frequency of the circulating slave laser field could be pulled away from ν_0, it would still circulate in the cavity but at a reduced level.

If the laser field of the master oscillator is now aligned to resonate in the slave laser cavity the situation is similar to that of Fig 3.10

When the frequency of the light from the master laser lies within the injection locking range of the slave laser frequency ν_0, the slave's free running mode is extinguished and is replaced by an oscillation at the master frequency. Varying the frequency of the master laser then allows the injection locked laser frequency to be tuned. The magnitude of the field circulating in the slave cavity (and so the injection locked output power) is then proportional to the cavity characteristic Airy function. The important point is that injection locking pulls the slave laser frequency away from the slave cavity resonant frequency ν_0 and forces the magnitude of the circulating field to drop. The slave laser cannot

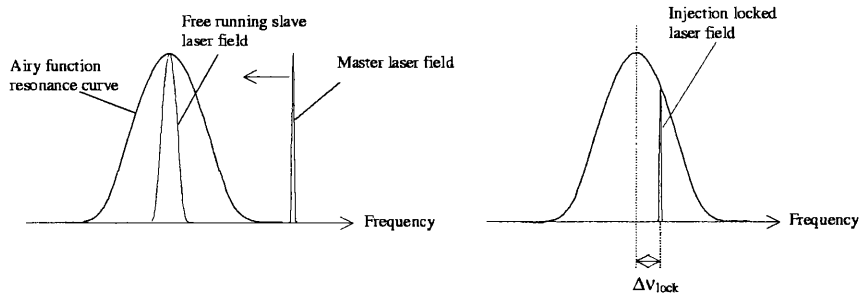

Figure 3.11: *Airy function associated with slave cavity resonance with the free running slave laser output at the cavity resonant frequency ν_0. Shown is the condition with the master laser frequency outside locking range where the slave laser frequency lies at ν_0. When the master laser frequency is within the locking range, the injection locked laser frequency is at that of the master laser.*

return to ν_0 until the master laser frequency is outwith the injection locking range. A subtraction technique for locking a laser to a passive Fabry-Perot cavity can still be used. Each photodiode detects the field from the slave laser which is subtracted to leave a locking signal dependent on the master laser as in the passive case. The relative gains of PDA and PDB can be tuned to allow the locking point to be somewhere on the fringe side within the injection locking range from the cavity resonant frequency.

A servo was constructed to use the error signal obtained from the fringe-side lock and is shown in Fig 3.12. The locking bandwidth is again limited by a resonance in the intra-cavity PZT at 15 kHz. The peak output power is similar to that obtained with rf-reflection locking and can be varied by small changes in the locking point.

If the locking point is moved towards the edge of, or just outside the locking range from the cavity resonant frequency, an interesting observation can be made. The two photodiodes still produce a locking signal to lock the frequency of the slave laser. The slave laser however cannot follow exactly the master frequency changes. In this situation the free running oscillation of the

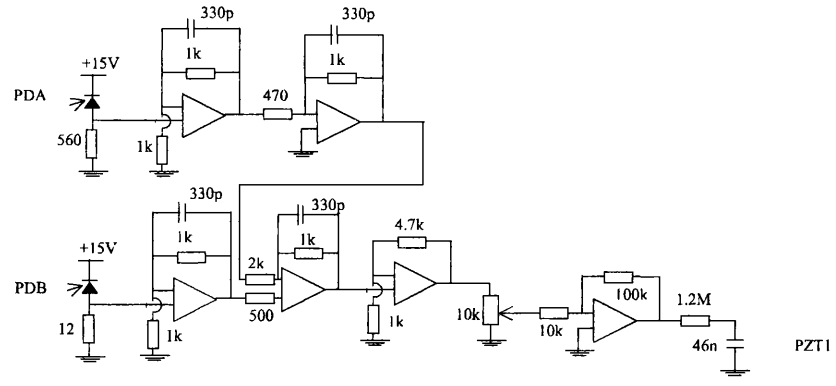

Figure 3.12: *Fringe side lock servo used to hold slave laser frequency within the injection locking range.*

slave laser begins to contaminate the single frequency output. Viewing the laser frequency spectrum with a scanning Fabry-Perot cavity shows the dominant oscillation at the frequency of the master laser but other free running oscillations now appear at different frequencies as in Fig 3.13. The top picture shows the situation when the locking point is close to the resonant frequency of the slave laser cavity i.e. slave laser frequency is well within the injection locking range. The middle picture shows the case when the locking point is moved close to the injection locking range from the slave laser cavity resonant frequency and small contaminant frequencies are present. The lower picture shows the result of moving the locking point to the edge of the injection locking range. The single frequency output is now heavily contaminated.

3.4 Power noise

A Nd:YAG laser power noise is dominated by the relaxation oscillation [62]. Occurring typically at several hundred kHz it produces around 40-50 dB of excess power noise and is caused by differing time constants associated with the upper state lifetime and cavity storage time. The actual frequency is given

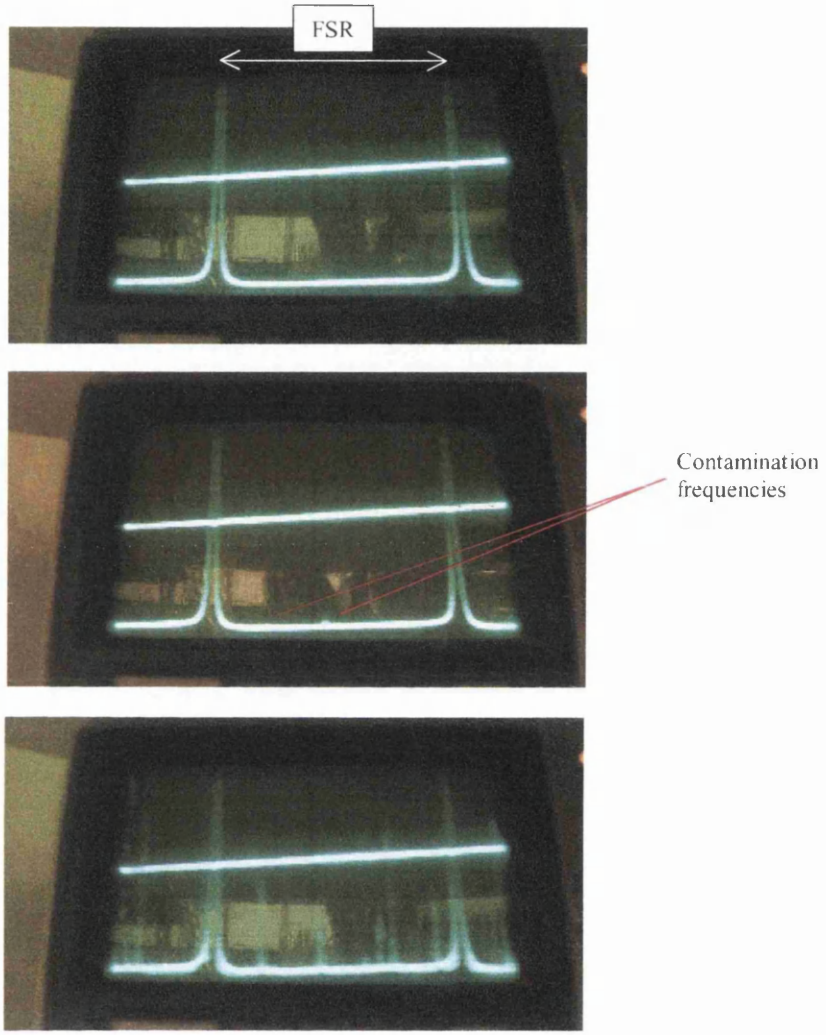

Figure 3.13: *The injection locked slave laser output viewed on a scanning Fabry-Perot optical spectrum analyser. The ramped line is the scan signal. The content of each picture is described in detail in the text.*

by

$$\nu_{RO}^2 = \frac{1}{(2\pi)^2}\gamma_l\gamma_c(r-1) \tag{3.9}$$

where γ_l is the upper state decay rate, γ_c is the cavity decay rate and r is the normalised pumping rate defined as

$$r = \frac{\text{Pump power}}{\text{Threshold pump power}}. \tag{3.10}$$

Generally the further above threshold the Nd:YAG is pumped the higher the relaxation oscillation frequency.

The power noise spectra of the NPRO around the relaxation oscillation frequency is shown in Fig 3.14. A power noise reduction servo supplied with the NPRO suppresses this relaxation oscillation and gives $\sim$ 20 dB of noise reduction at lower frequencies [63, 64, 65].

The free running slave laser exhibits a relaxation oscillation at $\sim$ 133 kHz as shown in Fig 3.14. As a result of injection locking, the slave lasers relaxation oscillation frequency is unchanged but its decay rate is increased. The slave laser relaxation oscillation is therefore damped due to the dominant injected master field by an amount proportional to the ratio $\frac{P_{master}}{P_{slave}}$. The oscillation is at least critically damped for power ratios typically used in injection locking. It is replaced by an oscillation at the relaxation oscillation frequency of the master [56]. Since the noise reduction servo removes this, the injection locked lasers output power can be made to feature no relaxation oscillation.

The low frequency power noise of the NPRO is

$$\frac{\Delta P}{P} = 10^{-7}/\sqrt{\text{Hz}} \tag{3.11}$$

with the noise reduction servo active and this is approximately constant to 100 kHz. The spectral density of power noise of the injection locked slave laser is shown in Fig 3.15 and was measured using a YAG200 photo-diode with 10 mA of photo-current.

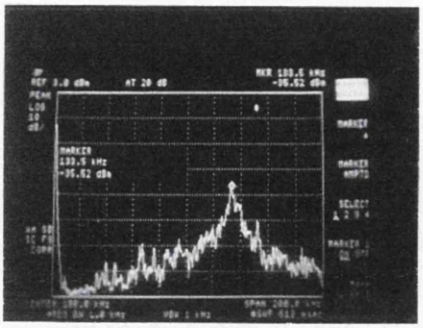

Spectral density of power noise for free running slave laser.

Relaxation oscillation at 133kHz.

Full scale 0-200kHz linear scale.
Power noise 10dB/div.

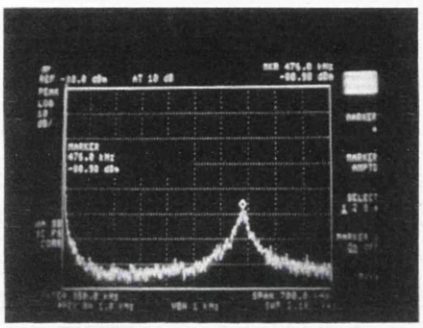

Spectral density of power noise for NPRO.

Relaxation oscillation at 476kHz.

Full scale 0-750kHz linear scale.
Power noise 10dB/div.

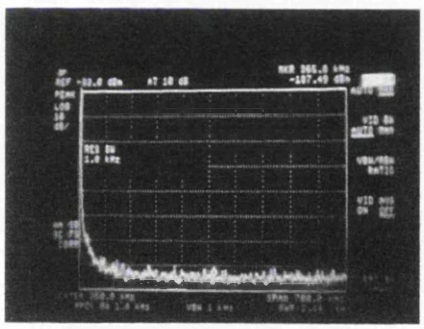

Spectral density of power noise for injection locked slave laser with NPRO relaxation oscillation servo operating.

Relaxation oscilation gone.

Full scale 0-700kHz linear scale.
Power noise 10dB/div.

Figure 3.14: *Intensity noise around relaxation oscillation*

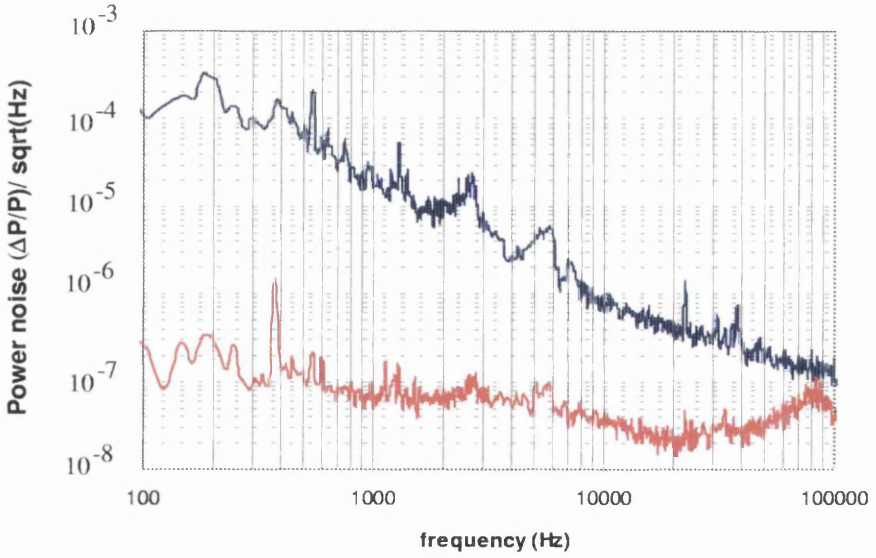

Figure 3.15: *Power noise of injection locked laser (top) and power stabilised injection locked laser. Shot noise level at* $5 \times 10^{-9}/\sqrt{\text{Hz}}$ *is well below measured spectra.*

The power noise of the injection locked laser is similar in magnitude to that of the free running laser up to 50 kHz. Structure can be seen in the injection locked lasers power noise spectrum at acoustic frequencies. The origin of this is due to the fact that the slave cavity path length is affected by acoustic noise in the room through refractive index fluctuations in the air and direct mirror motion. The PZT holding the slave cavity resonant, has therefore most action in the acoustic region. The laser mode is translated through the gain medium as the PZT moves, varying the position of the mode in the gain medium (as in Fig 3.16) and introducing power noise.

Further the pumping diodes are water cooled introducing vibrations which can move the pump beam relative to the Nd:YAG rod. This motion can make small changes in the gain thus adding power noise. If the water flow is turbulent the cooling may not be at a constant level, varying both the frequency and output power from the pumping diodes and introducing power noise. A noise

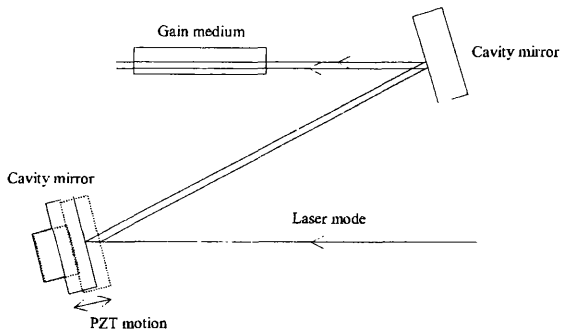

Figure 3.16: *Due to the angle at which the laser mode is incident on the actuated mirror, motion of the mirror displaces the laser mode in the gain medium.*

reduction servo was used to reduce the power noise of the injection locked laser. The electronic servo shown in Fig 3.17 is a modified version of that used to power stabilise the argon ion laser[1] and uses a crossed electro-optic modulator and polariser arrangement as the actuator. Linear polarised light incident on the EOM, can have its polarisation state changed by applying a voltage across the modulator crystal, assuming the optic axis of the crystal and the angle of polarisation are not parallel. The light power transmitted through the polariser is therefore variable. A LEYSOP $LiNbO_3$ electro-optic modulator was initially used, but thermal drifts caused the EOM to act as a variable high order waveplate, varying the polarisation by more than the range of the servo in short time scales. This problem was overcome by using two modulators in series with their optic axes perpendicular to each other. In this way thermal drifts, common to both crystals cancel but by applying an opposite sign of volts to both crystals the polarisation change caused by the voltage is doubled. The effect of the power noise reduction servo can be observed in Fig 3.15. The noise is reduced to $\sim 10^{-7}/\sqrt{\text{Hz}}$ around 1 kHz. Initially this power noise reduction was compromised by optical feedback. Improvements in the optical isolation

[1]Original design by S.D. Kilbourn and D.I. Robertson

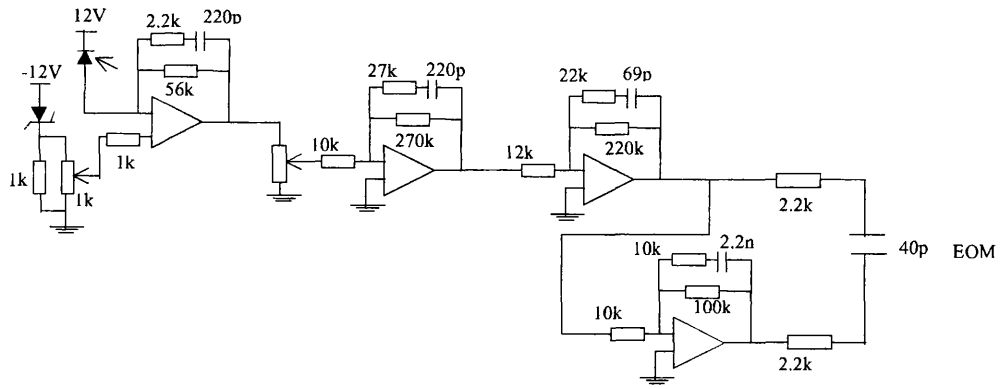

Figure 3.17: *Electronic servo system used to stabilise the power of the laser. The feedback actuator is the EOM.*

improved the noise reduction.

The power noise of the NPRO approaches the shot noise limit at a frequency of around 8 MHz. With the noise reduction activated this is reduced to around 5 MHz. The injection locked laser has very similar high frequency behaviour, also becoming shot noise limited by 5 MHz.

3.5 Conclusions

A laser system was constructed and characterised for use in the Glasgow 10 m prototype detector. Using a NPRO as the master oscillator, a high power slave laser was injection locked to make a single frequency laser with the low noise properties required. The laser produced $\sim$ 4 W in a TEM_{00} output mode. This type of laser has been used extensively before. The results presented here demonstrate that this laser behaves as predicted by the theory of injection locked lasers. The characterisation of the laser was crucial to the developments presented in later chapters. A new technique to hold the slave laser frequency within the injection locking range was used, relying on a simple fringe side lock and was found to operate well. This greatly simplifies the control scheme

required to frequency stabilise the laser.

Chapter 4

Frequency noise properties of the injection locked laser

4.1 Introduction

The injection locked laser described in Chapter 3, despite having better frequency stability than the argon ion laser, requires frequency stabilisation before it can be used with the 10 m prototype gravitational wave detector. Many experiments toward the frequency stabilisation of Nd:YAG lasers have been performed. Most have measured a relative stability between the laser frequency and a reference cavity [66, 67, 68, 69, 70] by way of an in-loop measurement at the error point of the stabilisation servo. Some measurements of the true frequency stability of the laser with reference to an independent frequency analyser have been performed, but results show the stabilised frequency properties several orders of magnitude above that required if the laser is to be used as the light source for a gravitational wave detector [71, 72].

A nested two loop stabilisation scheme was used for the argon ion laser [41] and this technique was utilised for the new infra-red laser source. Experiments were then performed to measure the absolute frequency noise properties of the

laser.

When designing a frequency stabilisation scheme several factors must be taken into account. A frequency reference is required and normally a resonant Fabry-Perot cavity is used for this purpose. The target fractional frequency deviation $\frac{\Delta\nu}{\nu}$ must be greater than the fractional length change of the reference cavity $\frac{\Delta l}{l}$ at frequencies of interest. The servo must have enough closed loop gain to reduce the frequency fluctuations to the required level. The effect of beam jitter and power noise in the laser light must be such that their contribution to the measurement can be ignored or controlled. Finally the minimum detectable frequency fluctuation as determined by the shot noise in the frequency discrimination detector must be below the frequency stabilisation target.

The two loop stabilisation system comprises a first pre-stabilisation loop which reduces the frequency fluctuations to $\sim 0.1\ \mathrm{Hz}/\sqrt{\mathrm{Hz}}$ in the band of interest and a second loop which reduces the fluctuations by a further factor of $\sim 10^4$.

4.2 1st loop frequency stabilisation

A Fabry-Perot cavity built around a Zerodur spacer, was selected as the first loop frequency reference. This monolithic spacer has a very low thermal expansion coefficient so provides a stable long term frequency reference.

The minimum fractional frequency fluctuation detectable due to shot noise using rf-reflection locking is given by [41]

$$\delta\nu = \Delta\nu_c \sqrt{\frac{\hbar\omega(1 - J_0^2(\beta)MV)}{16\eta P_0}} \left[\frac{1}{MJ_0(\beta)J_1(\beta)}\right] \times$$

$$\left[\frac{1}{1 \pm \sqrt{1 - V}}\right] \sqrt{1 + \frac{2{\nu_L}^2}{\Delta\nu_c}} / \sqrt{\mathrm{Hz}}. \qquad (4.1)$$

The parameters are the laser frequency ν_L, the reference cavity linewidth $\Delta\nu_c$, the modulation index β, the input power P_0, the power matched into the TEM_{00} mode of the cavity M, the visibility V and the quantum efficiency of

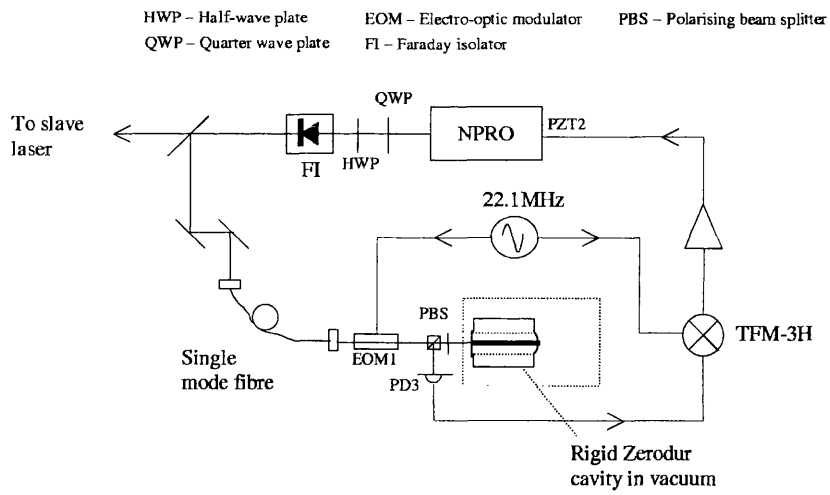

Figure 4.1: *First loop of laser frequency stabilisation.*

the photodiode η. The $\pm$ depends whether the internal cavity losses are greater or less than the transmission of the input mirror. The limit is proportional to the linewidth of the reference cavity $\Delta\nu = \frac{FSR}{F}$. For this reason, reference cavity mirrors were selected with a reflectivity high enough such that the shot noise limit would be below the frequency stability required. A target of the laser pre-stabilisation was set at $< 0.1\,\mathrm{Hz}/\sqrt{\mathrm{Hz}}$ due to phase noise in the AOM driver used in the second loop of stabilisation. This phase noise limits the frequency noise reduction of this pre-stabilisation loop. A finesse of 600 was found to be sufficient to attain this performance. This value of finesse facilitates lock acquisition, since it does not produce a large storage time which would necessitate the use of a wide bandwidth servo. The reference cavity must be isolated from external noise so it was placed in a vacuum vessel and mounted on rubber to limit the effect of acoustic and vibrational noise sources.

The rf-reflection lock frequency stabilisation scheme is shown in Fig 4.1. Approximately 20 mW was split from the main beam, phase modulated at 22.1 MHz and directed toward the rigid reference cavity. The rf reflection lock scheme based on the 22.1 MHz phase modulation provided an error signal

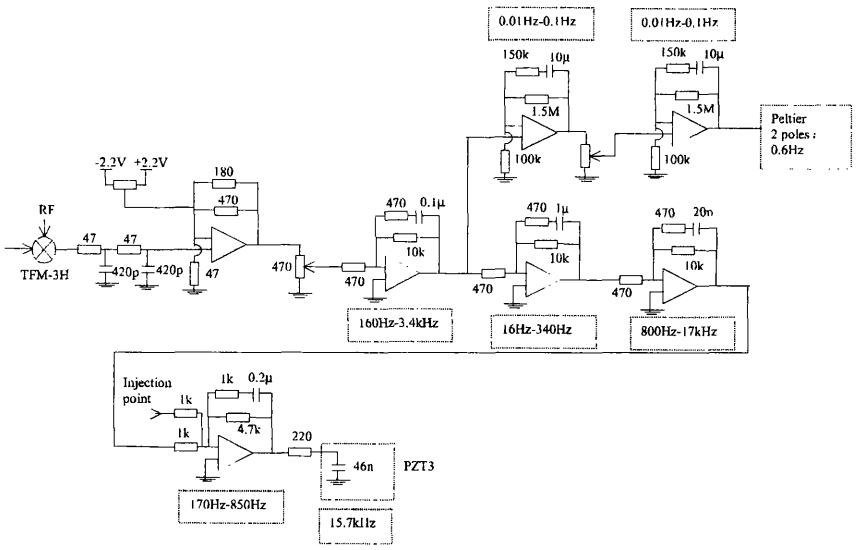

Figure 4.2: *Servo for first loop of frequency stabilisation.*

which was amplified and filtered and fed back to the PZT(PZT2) bonded to the NPRO crystal. The circuit for this stabilisation is shown in Fig 4.2. The stabilisation servo has a unity gain frequency of $\sim$ 60 kHz and limited by a resonance of PZT2 at around 200 kHz. In order to prevent the servo from running out of range, any long term drifting of the laser frequency was countered by feeding very low frequency signals back to a Peltier element located beneath the laser crystal. This was the dominant feedback element from DC to $\sim$ 0.6 Hz and provided a tuning range of several GHz.

Bode plots for the two feedback paths are shown in Fig 4.3. These plots were produced using the circuit modeling program LISO [73]. In producing these plots the effect of the reference cavity corner frequency at $\sim$ 1 MHz was ignored.

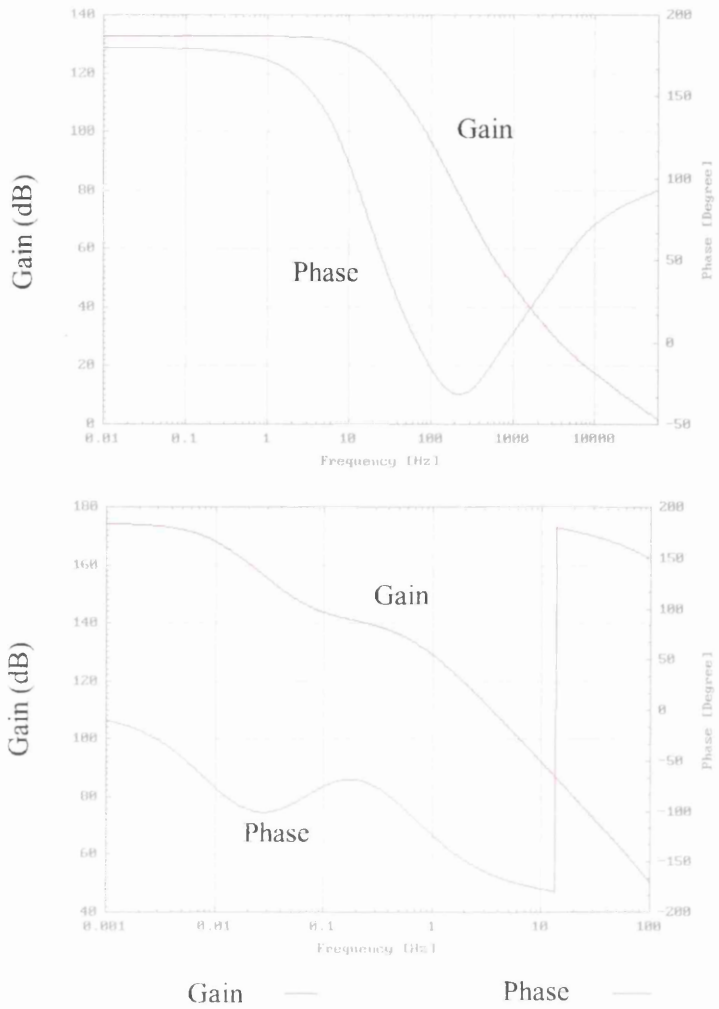

Fast path – unity gain frequency ~60kHz

Feedback element PZT2

Slow path – crossover frequency ~0.6Hz

Feedback element peltier

Figure 4.3: *Bode plots for the 1st loop frequency stabilisation electronics. The top plot shows the fast path with PZT2 as the actuator. The bottom plot shows the slow path with the Peltier element as the actuator. The discontinuity in the lower plot is a result of the plotting program.*

4.3 Measurement of frequency properties using secondary cavity

The frequency properties of the stabilised NPRO were measured using the secondary cavity. The secondary cavity is designed to stay on resonance with the laser light via a servo which produces a feedback signal to actuate on a cavity mirror. The cavity length control is achieved using magnetic forces between coils mounted on a suspended reaction mass and magnets bonded to the rear of the outboard cavity mirror. The locking scheme to develop the error signal for the cavity length control is based on another rf-reflection lock, this time operating at 12 MHz as shown in Fig 4.4. The photodiode circuit is shown in Fig 4.5 and is tuned to 12 MHz to give the maximum possible signal at the modulation frequency, while attenuating signals at other frequencies. With this arrangement shot noise in 10 mA of diode photocurrent produces a signal $\sim$ 20 dB above electronic noise.

The servo system to hold the secondary cavity locked must be designed to overcome the 12 dB/octave response of the pendulum. With careful design, electronic filtering can be used to give sufficient phase advance to give this loop a bandwidth of a few kHz, while notch filters are included to attenuate the effect of high-Q ($\sim 10^3$) internal mechanical modes of the mirror masses which would otherwise cause the servo to become unstable in a much reduced bandwidth [74].

With the loop locked, the signal required to be fed to the coils on the reaction pendulum to keep the cavity on resonance with the laser light gives a direct measure of the frequency deviations of the light. The closed loop response of the locking loop and the mechanical response of the mirror suspension must be taken into account: more specifically, at frequencies well within the bandwidth of the locking loop the feedback signal sent to the control coils can be calibrated to give a measure of the frequency fluctuations of the light. At frequencies well

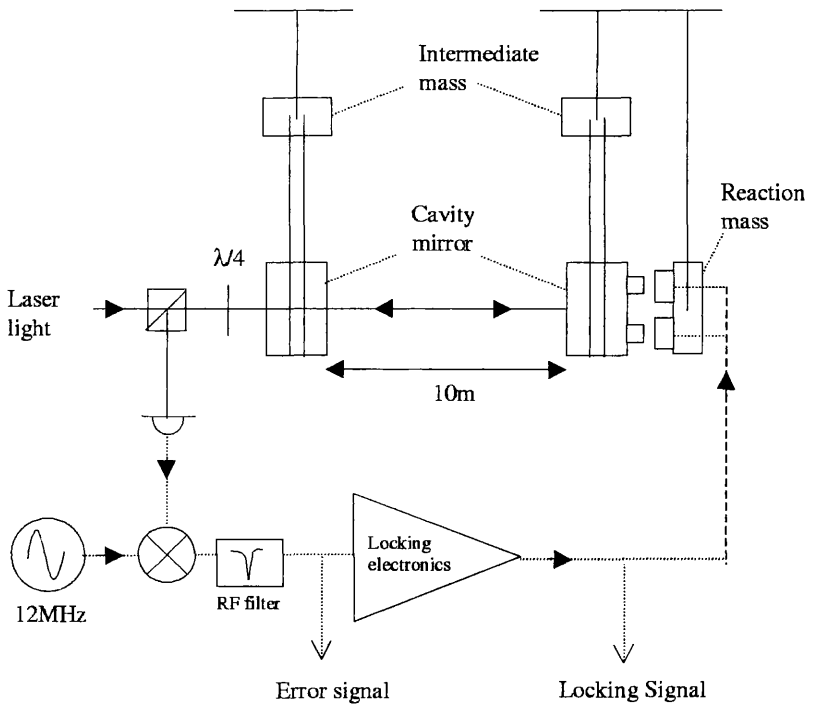

Figure 4.4: *The analyser cavity and locking scheme cavity*

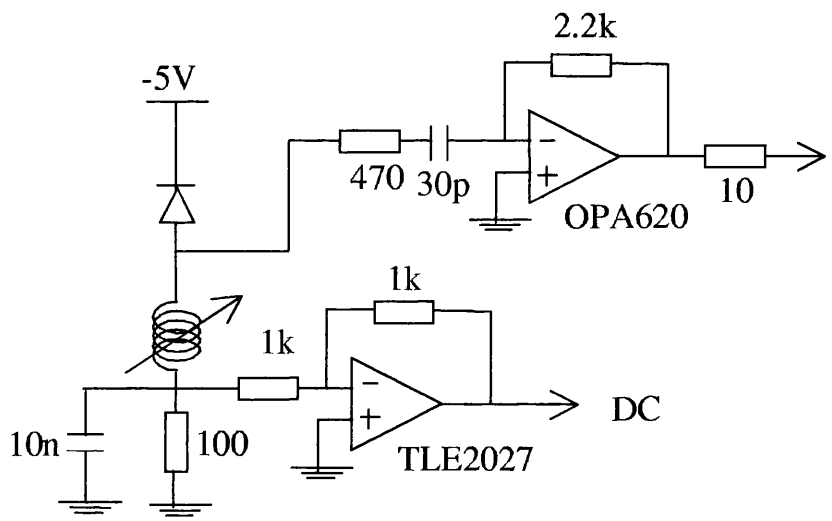

Figure 4.5: *Tuned photodiode for frequency noise measurements.*

above the loop bandwidth, the error signal of the loop is calibrated to yield the frequency fluctuations.

4.3.1 Calibration

The measured frequency fluctuations based on the feedback signal to the reaction mass, used to lock the secondary cavity to the laser light was cross-calibrated in three ways. Firstly, PZT2 bonded to the top of the NPRO crystal gives a frequency deviation of 2.4 MHz/V and this was confirmed using a commercial scanning Fabry-Perot optical spectrum analyser. Signals applied to this PZT can therefore be used to produce calibration peaks on the measured noise spectra. Such calibration peaks can be applied in low or high frequency regions appropriate to the cases of measuring the feedback signal or error point in the suspended cavity locking servo. Secondly, an acousto-optic modulator (AOM) [75] was placed in the beam immediately before the optical fibre directing the light to the secondary cavity. This component produced a known frequency deviation of 2 MHz/V and could also be used to produce a calibration peak in both locking signal and error point signal. This provides a useful check against the peaks applied to the PZT on the NPRO. Thirdly, in order to convert the feedback signal applied to the suspended mirror mass to a mechanical motion of the mirror, the mechanical transfer function of the pendulum suspension must be known. This transfer function has been modeled to predict the frequency behaviour of the mirror based on the response to a static force [37]. A check of this was made by constructing a small Michelson interferometer at the end of the interferometer vacuum chamber, but external to it. One of the arms of this interferometer had as its end mirror the suspended mirror of the secondary cavity. Sinusoidal signals of various frequencies were fed to the reaction pendulum coils and fringe counting techniques could be used to check the transfer function. The results of this are shown in Fig 4.6.

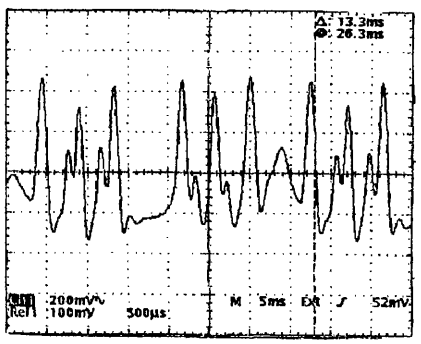

3 fringes per mirror sweep.
10Vp-p going to coils at 30Hz

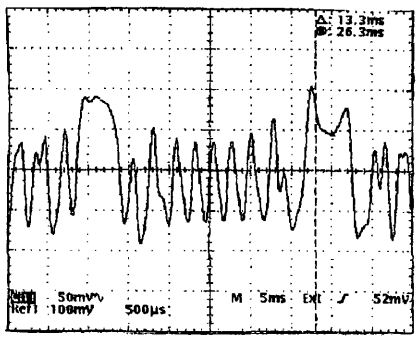

9 fringes per mirror sweep.
10Vp-p going to coils at 17.6Hz

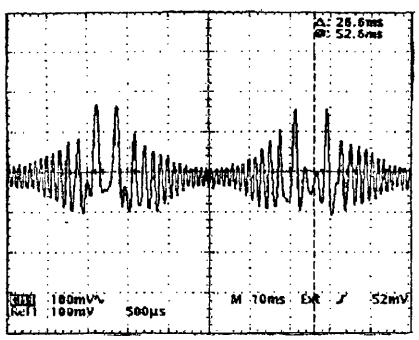

26 fringes per mirror sweep.
10Vp-p going to coils at 10Hz

Figure 4.6: *Fringes obtained from the calibration Michelson interferometer.*

All the various calibration techniques agreed to within 1 dB, and throughout the series of frequency noise measurements, it was common to have one or more of the calibration schemes operational, affording a constant check on the accuracy of the results.

4.3.2 Results

Fig 4.7 shows the spectral density of stabilised frequency noise obtained for the NPRO at low frequencies - those in the gravitational wave detection band. The spectral density of frequency noise is based on the feedback signal to maintain the analyser cavity lock. The background level is around $5 \times 10^{-2}\,\mathrm{Hz}/\sqrt{\mathrm{Hz}}$ at 1 kHz, which represents the shot noise limit of the laser frequency stabilisation loop. This was assertained by quadrupling the light level on the photodiode PD3 with the frequency stabilisation loop locked and observing the frequency noise spectral density reduced by a factor of two. Fig 4.8 shows the spectral density of frequency noise taken over 5 to 100 kHz and measured at the error point of the suspended cavity loop. The error point measurement must be corrected for the single pole of filtering introduced by the cavity corner frequency at $\sim$ 1 kHz. At higher frequencies (above 100 kHz) the spectral density of frequency noise of the NPRO begins to approach the Shawlow-Townes limit [76], estimated to be $\sim 2 \times 10^{-2}\,\mathrm{Hz}/\sqrt{\mathrm{Hz}}$, and this is shown in Fig 4.9. The stabilisation servo has little effect at frequencies above 200 kHz and the measurement represents the basic noise of the NPRO in this range.

4.3.3 Interesting observations

The need for isolation of the reference cavity from the vacuum chamber walls was explored. In a simple comparison experiment, the rigid reference cavity was mounted so that a part of it was touching the wall of its vacuum chamber. The spectral density of frequency noise in this case was limited to $> 1\,\mathrm{Hz}/\sqrt{\mathrm{Hz}}$

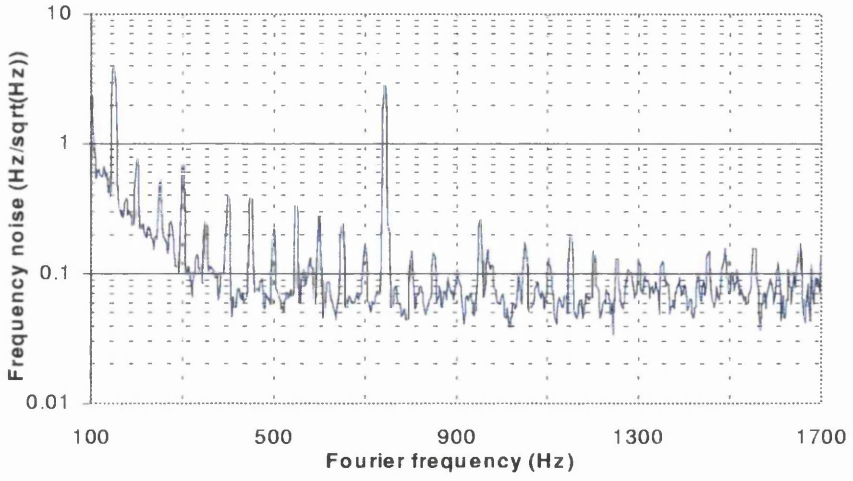

Figure 4.7: *Spectral density of frequency noise 100 Hz-1.7 kHz. Small spikes are 50 Hz harmonics and the large spike is a calibration signal.*

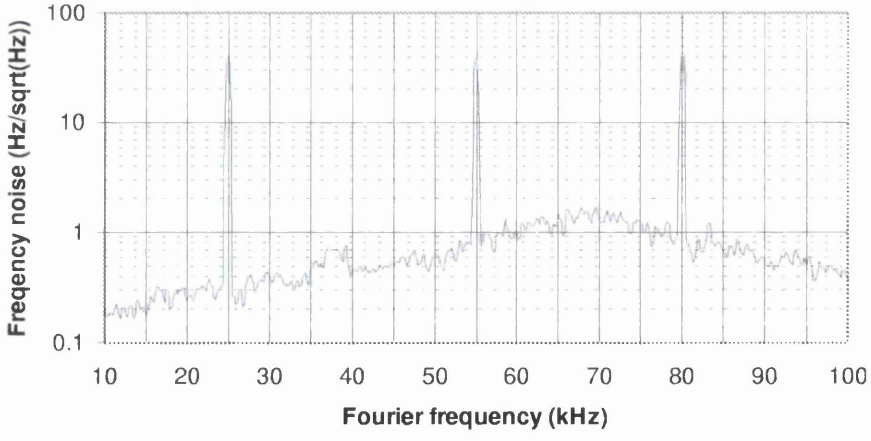

Figure 4.8: *Spectral density of frequency noise 5 kHz-100 kHz. Spikes are for calibration purposes.*

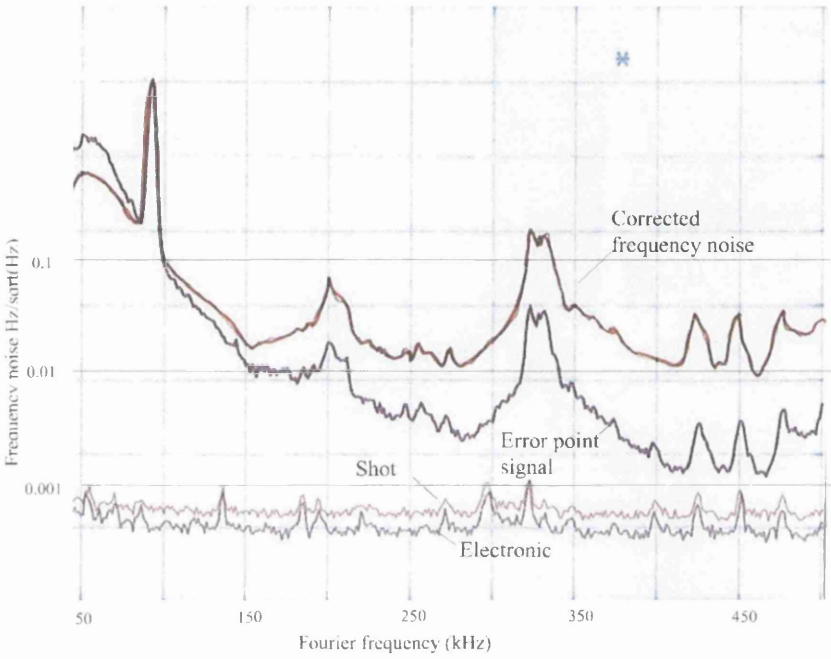

Figure 4.9: *Spectral density of frequency noise 50-500kHz. Level of noise approaches the Shawlow-Townes limit above 350 kHz.*

in the gravitational wave band, due to acoustic noise coupling through the vacuum vessel wall to the rigid cavity optical path length. Mounting the reference cavity on soft rubber pads allowed the results detailed in the previous section to be attained.

While making these frequency noise measurements the phase noise properties of voltage controlled oscillators (VCO) used as AOM drivers was examined. The motivation for this is that in the full stabilisation scheme, a voltage controlled oscillator driving an AOM is used to give a low noise broad-band frequency actuator. An 'Automates et Automatismes' AOM was inserted in the path of the light going to the frequency stabilisation rigid reference cavity. The AOM was double-passed to minimise the beam jitter introduced by the AOM and the 1st order diffracted beam aligned into the single-mode optical fibre before entering the reference cavity. The spectral density of frequency noise of the stabilised laser was then measured as before using different VCOs. The commercial VCO supplied with the AOM produced $\sim 2\,\mathrm{Hz}/\sqrt{\mathrm{Hz}}$ of noise but had the advantage of large pulling range $\pm 10\,\mathrm{MHz}$. The best VCO was found to be a modified ISOMET crystal oscillator with a varicap inserted to pull its frequency. The pulling range must be sacrificed in order to achieve the benefit of low phase noise performance, particularly when taking advantage of the narrow linewidth provided by crystal oscillators. The best balance achieved was based on a pulling range of $\pm 0.5\,\mathrm{MHz/V}$ while imposing a frequency noise of $\sim 0.2\,\mathrm{Hz}/\sqrt{\mathrm{Hz}}$ on the double-passed light.

4.3.4 Conclusions

The NPRO was frequency pre-stabilised and a spectral density of frequency noise of $5 \times 10^{-2}\,\mathrm{Hz}/\sqrt{\mathrm{Hz}}$ was measured using a suspended high finesse cavity as a frequency discriminator. This represents a level consistent with the initial requirement. The stabilisation achieved was limited by shot noise in the

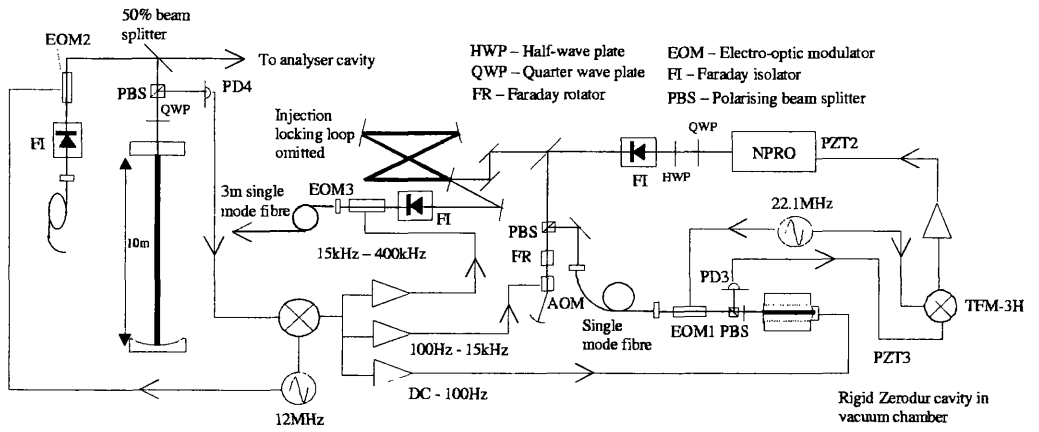

Figure 4.10: *Schematic of the second loop of frequency stabilisation. The actuators are PZT3 (mounted on the rigid reference cavity), the AOM (in the double passed optical spur which the light encounters on its way to the reference cavity) and phase corrector EOM3 (positioned immediately before the 3 m fibre).*

detected light.

4.4 2nd loop stabilisation

The aim of the 2nd loop of stabilisation is to reduce the frequency fluctuations of the laser light to a level comparable to that required for gravitational wave detectors. For example a spectral density of frequency noise of $\sim 10^{-5}\mathrm{Hz}/\sqrt{\mathrm{Hz}}$, corresponds to a fractional frequency fluctuation $\frac{\Delta f}{f} \sim 10^{-19}/\sqrt{\mathrm{Hz}}$, and to achieve this level a second reference cavity with fractional length fluctuations $\frac{\Delta L}{L} \sim 10^{-19}/\sqrt{\mathrm{Hz}}$ is required. To reduce the shot noise limited detectable frequency fluctuation to the levels necessary, requires the use of a narrow linewidth reference cavity given the light power available. The 2nd loop stabilisation scheme is shown in Fig 4.10. The primary cavity is used as a reference where the 10 m length and finesse of $\sim 10,000$ give a linewidth of $\sim 1.5\,\mathrm{kHz}$. A photodiode PD4 identical to that in Fig 4.5 generates a signal from the light

reflected from the primary cavity and an rf-reflection lock scheme is used to provide a correction signal to hold the laser frequency resonant with the cavity. This correction signal is added to the error point of the first loop via the use of two further actuators. One of the mirrors in the rigid Fabry-Perot reference cavity is mounted on to a PZT (PZT3) allowing the cavity resonant frequency to be changed. Correction signals from the second loop from DC to around 100 Hz are fed to PZT3 which provides 84.6 MHz/V actuation. The AOM driven by the modified ISOMET VCO is positioned in the path of the light entering the rigid reference cavity and provides frequency tuning of 0.5 MHz/V from approximately 100 Hz to 15 kHz. Since these signals are applied at frequencies well within the bandwidth of the first loop, the laser frequency changes by the size of the applied signal to either of these actuators when the first loop is locked. In practice the stability achieved by the first loop is limited to $\sim 2 \times 10^{-1}\,\mathrm{Hz}/\sqrt{\mathrm{Hz}}$ due to phase noise imposed by the VCO which controls the AOM. In view of this limit care was taken to ensure that the second loop had sufficient gain to reach the required spectral density of frequency noise. Correction signals above 15 kHz are applied to EOM3 which acts as a phase corrector. The overall frequency stabilisation system has a unity gain frequency of ~ 400 kHz and a gain of $\sim 1 \times 10^6$ at 1 kHz as determined by the comparison of the size of test signals injected into the servo loop when the loop was open and closed.

4.4.1 Calibration

The calibration method described above using a direct measurement of the feedback signal to the mirror in the secondary cavity is still valid. A different method of cross checking is now used. A frequency modulation is applied to the laser by sinusoidaly varying the length of the primary cavity. This is achieved via magnets bonded to the cavity mirror and coils mounted rigidly to a reaction

plate. The frequency deviation imposed can be measured by monitoring the feedback signal to the AOM, the dominant feedback element in the band of interest. The size of the peak on the feedback signal to hold the secondary cavity locked then gives a marker from which to derive the background noise level.

4.4.2 Results

First consider the frequency noise measured for the NPRO. The spectral density of secondary cavity locking signal is multiplied by the transfer function of voltage to frequency to give a spectral density of frequency noise in the band of interest and is shown in Fig 4.11.

The spectral density of frequency noise of the injection locked laser was then measured in the same way. A power noise reduction servo based on a crossed polariser and EOM reduced the power fluctuations of the injection locked laser to similar levels as that of the power stabilised NPRO.

To compare the frequency properties of master and injection locked slave lasers, the output of the injection locked laser was attenuated to reduce the power to a similar level to that of the master laser.

A first attempt to measure the frequency properties was made with rf-locking used to hold the slave cavity length within the injection locking range. This servo used a different modulation frequency to that for locking the suspended cavities.

With two different modulation frequencies beats were produced which caused the low noise locking electronics for the suspended cavities to become slew rate limited and severely impaired the performance of these servos. The modulation free injection locking scheme described in Chapter 3 allowed the results detailed below.

A comparison of the spectral density of frequency noise for the master and

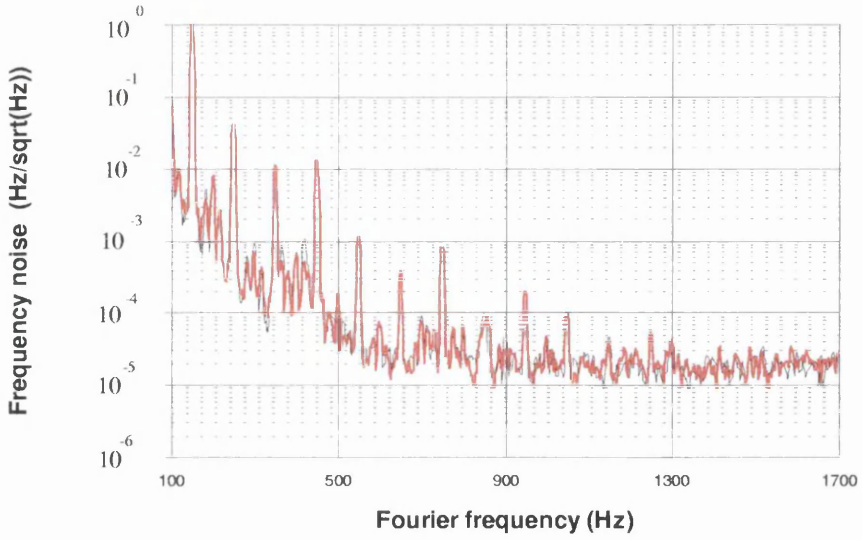

Figure 4.11: *The spectral density of frequency noise measured using the independent analyser cavity. Spectra are for the master laser (red) and for the injection locked laser. Peaks are dominantly 50 Hz harmonics.*

injection locked lasers is shown in Fig 4.11. The level of $2 \times 10^{-5}\mathrm{Hz}/\sqrt{\mathrm{Hz}}$ around 1 kHz is identical for both the master and injection locked lasers.

To ensure that the injection locked slave was following accurately the frequency fluctuations of the pre-stabilised master oscillator, a comparison of the relevant control signals for the master operating alone with those of the injection locked laser system was made. The signals fed to PZT2 on the NPRO gain medium, the phase corrector EOM3 and the AOM were measured with both stabilisation loops locked for the two cases. The results are shown in Fig 4.12, Fig 4.13 and Fig 4.14 and all control signals can be seen to be identical for both lasers in the frequency band of interest. From these results it is believed that the frequency of the injection locked slave laser is following accurately that of the pre-stabilised master oscillator.

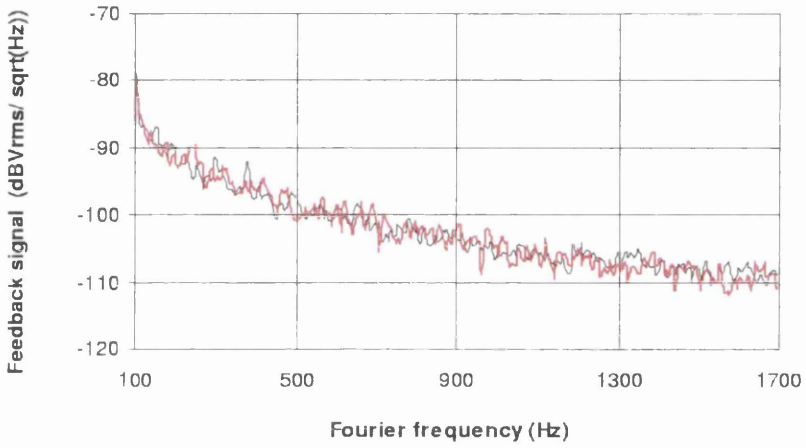

Figure 4.12: *Spectral density of signal fed to PZT2 on the master laser gain medium with both stabilisation loops locked. Spectra can be seen to be identical for the master laser alone (red) and injection locked system, showing that the slave laser is not introducing excess noise of a level comparable to that of the free-running master.*

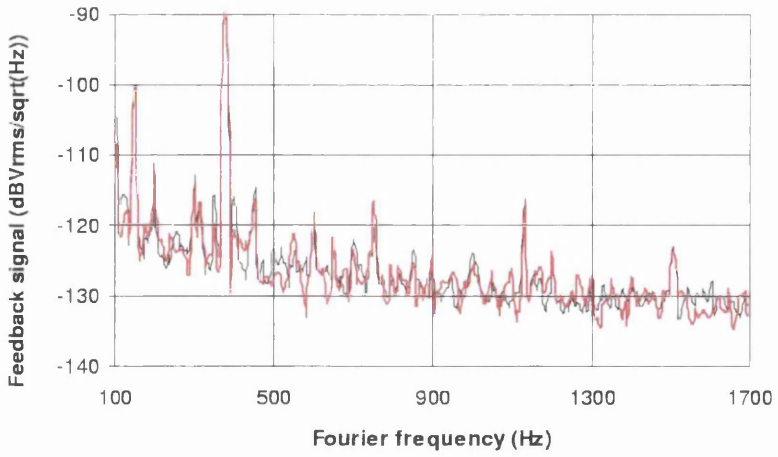

Figure 4.13: *Spectral density of the signal fed to the AOM with both stabilisation loops locked. Spectra are for the master laser alone (red) and injection locked slave and can be seen to be the same, showing that the slave cavity does not introduce noise of a level comparable to the pre-stabilised master laser. Peaks are dominantly 50 Hz harmonics.*

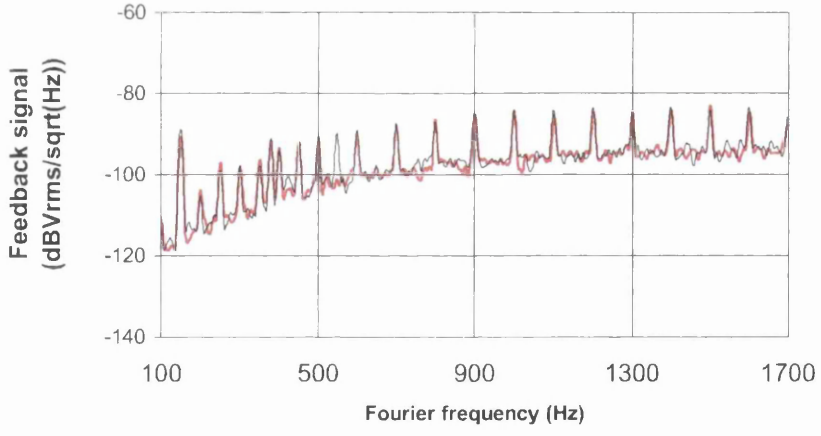

Figure 4.14: *Spectral density of the signal fed to the phase corrector EOM3 with both stabilisation loops locked. The two spectra are for the master laser alone (red) and injection locked slave. Peaks are dominantly 50 Hz harmonics.*

4.5 Conclusions

The spectral density of frequency noise of the NPRO was stabilised to a level of $2 \times 10^{-5}\mathrm{Hz}/\sqrt{\mathrm{Hz}}$ around 1 kHz. The injection locked laser frequency noise was shown to be identical in this region. This was achieved with a modulation free fringe side injection locking scheme and a two loop frequency stabilisation scheme. This demonstrates for the first time the feasibility of using an injection locked laser to increase the available light power without degrading the frequency properties of the master laser from the levels required for gravitational wave detection. This step is crucial for the large scale interferometers that will use injection locked lasers as their light sources. These experiments differ from others because a frequency analyser cavity with a very stable resonant frequency was used to measure the stabilised noise properties. The levels of stabilised frequency noise obtained are the best to date for a laser of this type. The published results based on these experiments can be found in [77].

Chapter 5

Measurement of the frequency noise associated with the relaxation oscillation of a Non-planar Ring Oscillator

5.1 Introduction

Despite the low level of the general broadband power noise, a NPRO exhibits a relaxation oscillation (RO) caused by differing time constants for the cavity decay rate and the upper state lifetime [62]. The RO is seen as a broad peak in the laser power spectrum. The frequency of this peak is dependent on the pump rate, and is typically of the order 500 kHz for a laser of this type. The question of whether there is an oscillation in the frequency of the laser at the RO frequency is less clear. The aim here is to set a limit on the frequency noise associated with the RO, which may be of particular interest when considering the effect such a frequency noise might have on the various control servos used in highly sensitive interferometric gravitational wave detectors. In view of the

high frequency at which the RO is located, the impact on interferometric gravitational wave detection could be through non-linearities associated with the detection system, similar to those associated with the beats between different modulation frequencies described in Chapter 4. Also, recent work to reduce the frequency noise of an NPRO using the pumping diode as a frequency actuator and varying the diode current have demonstrated some resonant behaviour in the frequency response around the RO frequency [78]. For these reasons it is useful to further investigate the level of frequency noise at the RO and improve on the limit set by previous measurements [79].

5.2 Source of the frequency noise

The dominant source of frequency noise is believed to arise through the non-linear refractive index n_2 and the time varying intra-cavity power at the RO frequency. As the intra-cavity laser mode is contained entirely within the Nd:YAG, the optical path length p is related to the geometrical path length l by $p = \frac{l}{n}$ where n is the observed refractive index of the Nd:YAG. The refractive index term can be expanded to account for the change induced by an electric field. The observed refractive index is given by $n = n_0 + \Delta n$ where n_0 is refractive index and Δn is the change caused by the presence of an electric field. The change in refractive index is proportional to the intensity I of light in the crystal and is given by $\Delta n = I n_2$ with n_2 the non-linear refractive index. The change in the laser frequency $\Delta\nu$ caused by a change in the refractive index Δn can be described by $\Delta\nu = \nu\frac{\Delta n}{n_0}$ where ν is the laser frequency. Given that at the RO frequency, the intra-cavity power of our 800 mW NPRO is ~ 30 W and varies by $\sim 1 \times 10^{-4}$ at the RO frequency the variation in the intra-cavity intensity can be calculated to be $\sim 3000\,\mathrm{W/m^2}$. Taking $n_2 = 9.38 \times 10^{-20}\,\mathrm{m^2/W}$ for YAG [80], and assuming the only intensity fluctuation is at the RO frequency, Δn is $\sim 2.8 \times 10^{-16}$ giving a frequency

change induced by the RO of $\Delta\nu \sim 0.01\,\mathrm{Hz}/\sqrt{\mathrm{Hz}}$.

Other mechanisms for the generation of frequency noise at the RO frequency include that induced by the time varying absorption of the 1064 nm circulating field at the RO frequency. The time delay associated with thermal changes to the Nd:YAG properties and the low absorption at 1064 nm, prevents the oscillating intra-cavity intensity at 1064 nm contributing an appreciable frequency noise level by this mechanism.

Measurements of the frequency noise at the relaxation oscillation frequency [79, 81] have been made and in particular [79] placed a limit of $1\,\mathrm{Hz}/\sqrt{\mathrm{Hz}}$ on the amplitude spectral density of frequency noise from a NPRO at the RO frequency, limited by the shot noise in the detected light. The use of the narrow linewidth secondary cavity as a frequency analyser has now allowed an improved limit to be placed on the frequency noise level.

5.3 Experiment

The frequency of the light from the NPRO was pre-stabilised as in Chapter 4 using the rigid reference cavity. The secondary cavity length was then locked to the pre-stabilised laser light and the signal at the error point (point X in Fig 4.4) of this loop measured with a high frequency spectrum analyser. The signal was measured with the RO power noise reduction servo on and off. The spectral density of error point signal is shown in Fig 5.1 for both cases.

Clearly there is structure in this spectrum when the power noise reduction servo is turned off. This shows that the content of the spectra with the noise reduction off is due primarily to power noise. There is however a contribution to the signal at the RO frequency from frequency noise of the laser. It is this signal that must be extracted.

The spectral density of noise due to the relaxation oscillation on the error point can be calibrated by modulating the laser frequency by a known magnitude

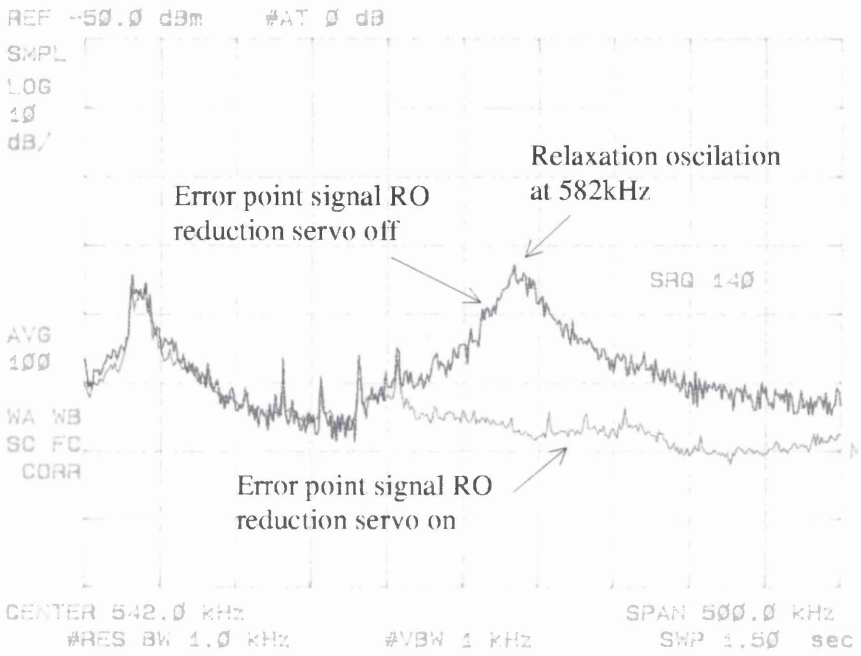

Figure 5.1: *Spectral density of error point signal from secondary locking servo with RO reduction servo on/off.*

and monitoring the effect on the error point. Trace A in Fig 5.2 shows the spectral density of error point signal around the relaxation oscillation. The peak at 592 kHz represents an applied frequency deviation of 20 Hz. The RO peak on the error point therefore represents 10 Hz of frequency deviation or $0.57\,\mathrm{Hz}/\sqrt{\mathrm{Hz}}$ given the 300 Hz measurement bandwidth. This method produces a result based on the total signal in the spectral density of error point signal at the relaxation oscillation frequency. The contribution to this total signal due to frequency fluctuations can be estimated and the limit improved. The method for achieving this relies on the differing sensitivity of the error point signal to power and frequency modulations of the laser light. If the cavity is detuned slightly such that the fringe visibility is reduced, then the error point sensitivity to a frequency modulation decreases.

The peak at 562 kHz in Fig 5.2 is a power modulation applied to the laser and shows how this noise source can couple through to the error point signal.

The secondary cavity was misaligned slightly, with the fringe visibility reduced by 25 %.

Trace B in Fig 5.2 shows the spectral density of error point signal under these conditions with the same calibration peaks applied to the laser. Clearly the intensity peak at 562 kHz is unchanged while the frequency peak at 592 kHz is reduced by $\sim$ 2.5dB. If it is assumed that a change in the RO structure of 0.5 dB would be discernible and it does not appear to have changed in this limit, while the frequency peak has changed by 2.5 dB, an upper limit of 1.1 Hz can be set on the frequency noise content of the RO. This corresponds to frequency noise spectral density of $7 \times 10^{-2}\,\mathrm{Hz}/\sqrt{\mathrm{Hz}}$ given the 300 Hz measurement bandwidth.

This is greater than would be expected if the measurement were limited by the frequency fluctuations due to the non-linear refractive index. It is likely that the contribution to the measured signal from laser power fluctuations at the RO frequency is limiting the measurement, despite using an RF modulation

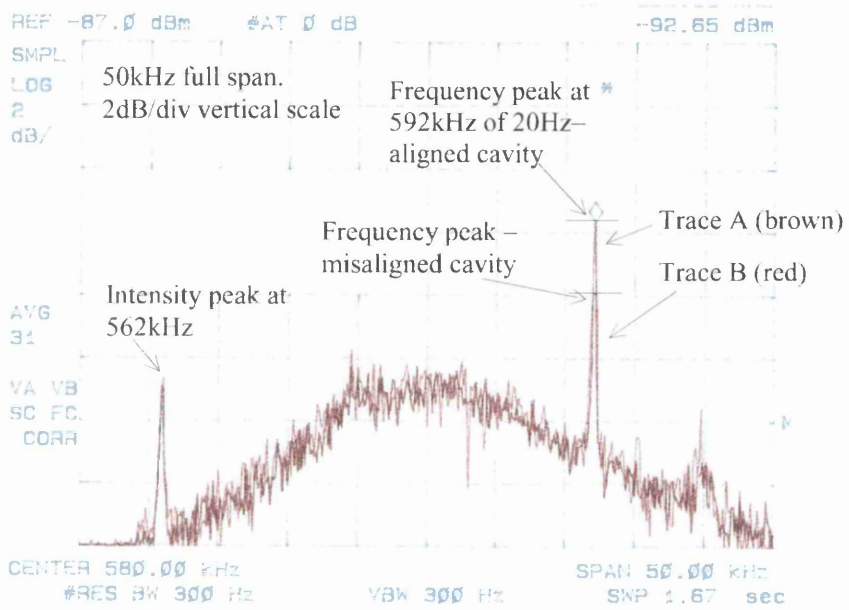

Figure 5.2: *Spectral density of error point signal from secondary locking servo at RO frequency. Spectra are for aligned cavity and misaligned cavity with intensity peak at 562kHz and frequency peak at 591kHz.*

technique and careful analysis of applied calibration signals to limit the impact of power noise.

The Schalow-Townes limited spectral density of frequency noise is below $0.01\text{Hz}/\sqrt{\text{Hz}}$ so is unlikely to be the limiting noise source.

5.4 Conclusions

The spectral density of frequency noise at the relaxation oscillation frequency was measured using the narrow linewidth secondary cavity to be not more than $7 \times 10^{-2}\,\text{Hz}/\sqrt{\text{Hz}}$. This is above the expected level based on a calculation of the frequency deviations arising from optical path length change due to the time varying refractive index at the RO frequency. This measurement has improved the upper limit set on this frequency noise by previous experiments but it should be noted that the actual frequency noise level was not measured due to the effect of power noise on the measurement. Published results can be found at [82].

Chapter 6

The prototype interferometer-sensitivity

6.1 Introduction

The preceding chapters have discussed the stabilisation of the new infra-red laser system and the optical arrangement of the two Fabry-Perot cavities which make up the prototype detector. The complete interferometer when operated as a gravitational wave detector can be calibrated to produce a spectral density of displacement sensitivity: that is the minimum differential displacement between the two cavities that can be measured. The displacement sensitivities of the different prototype detectors around the world vary by around an order of magnitude depending on the optical configuration. The best result is described in [83] where for the Caltech 40 m Fabry-Perot armed prototype the spectral density of displacement sensitivity reached $3 \times 10^{-19} \mathrm{m}/\sqrt{\mathrm{Hz}}$ at 450 Hz. The 30 m delay line Michelson interferometer at the Max Planck Institute in Garching reached a shot noise limited spectral density of displacement sensitivity of $4 \times 10^{-18} \mathrm{m}/\sqrt{\mathrm{Hz}}$ at 2 kHz [84]. The best performance of the Glasgow prototype detector described in [37] was $5 \times 10^{-19} \mathrm{m}/\sqrt{\mathrm{Hz}}$ around 1 kHz. All

these measurements were made with an argon ion laser source. Recently the TAMA 300 project has attained a spectral density of displacement sensitivity of $2 \times 10^{-18}\mathrm{m}/\sqrt{\mathrm{Hz}}$ around 1 kHz using an injection locked Nd:YAG laser in a power recycled Fabry-Perot Michelson arrangement [85].

6.2 Measurement

The spectral density of the frequency noise of the Nd:YAG laser was reduced to a level of $2 \times 10^{-5}\mathrm{Hz}/\sqrt{\mathrm{Hz}}$ around 1 kHz as measured with the secondary cavity as a frequency discriminator. This corresponds to a displacement of $7 \times 10^{-19}\mathrm{m}/\sqrt{\mathrm{Hz}}$ since $\frac{\Delta L}{L} = \frac{\Delta \nu}{\nu}$ and given the cavity length $L = 10\,\mathrm{m}$ and laser frequency $\nu = 2.82 \times 10^{14}\,\mathrm{Hz}$. The frequency noise is not reduced to the shot noise limit due to lack of gain in the frequency noise reduction servo. Residual frequency noise both in the gravitational wave band and at higher frequencies is common to both cavities of the detector. The demodulated photocurrent from the primary cavity photodiode PD4 gives information on the residual frequency noise of the laser. The effect of this residual noise can be reduced using common mode rejection. The signal due to excess frequency noise can be subtracted from the secondary cavity locking servo. With careful consideration of the different optical properties of each cavity (dominated by their differing finesse), several dB's of common mode rejection is possible, allowing the shot noise limit to be reached. This common mode rejection of frequency noise allows a more sensitive displacement sensitivity to be measured.

6.3 Results

The prototype interferometer was operated using the NPRO as the light source with around 15 mA (cavities unlocked) of diode photocurrent from each photodiode (same as Fig 4.5). The spectral density of displacement sensitivity was

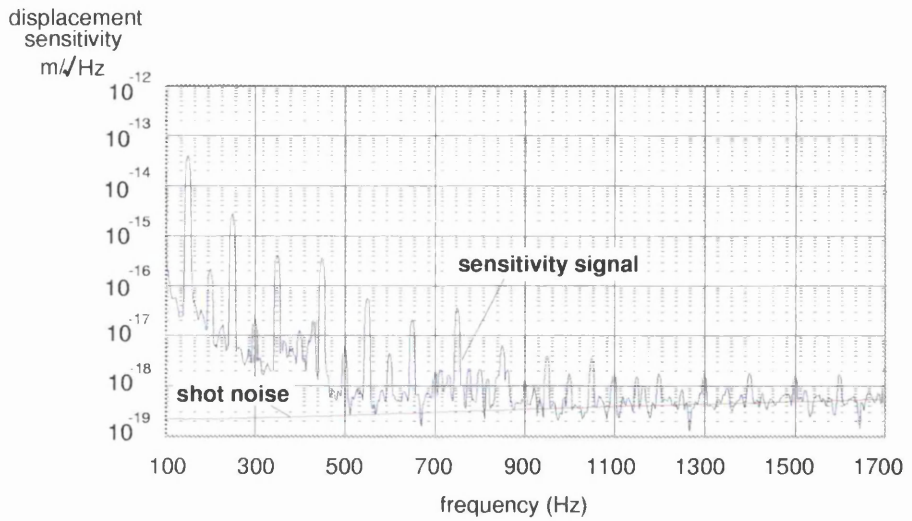

Figure 6.1: *Spectral density of displacement sensitivity obtained using the NPRO as the light source. Spikes are mainly mains in origin.*

measured to be $\sim 5 \times 10^{-19}\mathrm{m}/\sqrt{\mathrm{Hz}}$ at best and was limited by shot noise in the detected light. The spectral density of displacement sensitivity is shown in Fig 6.1 along with the calculated shot noise level. The cavity storage times were similar at 220μs and 230μs for primary and secondary cavities. Calibration of the displacement sensitivity is achieved as described in Chapter 4, using the static secondary outboard mirror response to an applied signal to the coils. The cross check is still performed by modulating the length of the primary arm. Although this imposes a frequency noise to the laser, it is not a common mode noise so is not removed by the common mode subtraction technique.

6.4 High power measurement

To improve the sensitivity, more light power is required to reduce the limit set by shot noise. The injection locked laser has sufficient output power such that the power handling ability of the detection photodiodes becomes the limiting

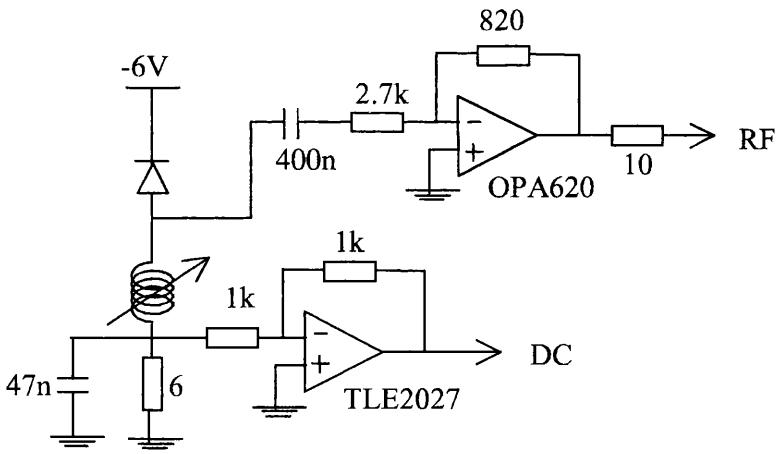

Figure 6.2: *High power acceptance photodiode tuned to 12 MHz. Photodiode is mounted to a Peltier cooler to remove excess heat.*

factor. The EG&G InGaAs photodiodes have a rated maximum of 100 mA photocurrent and 250 mW of power dissipation. To achieve the response required to detect the 12 MHz modulation frequency (necessary for the rf-reflection lock), several volts of bias are required to reduce the capacitance of the diode junction. Around 600 mW of power was then dissipated by the photodiode and for this reason the photodiode was mounted to a Peltier cooler to remove excess heat[1]. The photodiode amplifier circuit is shown in Fig 6.2 and the circuit is tuned to 12 MHz to give the maximum possible signal at the modulation frequency while attenuating out of band signals.

The injection locked laser was used as the light source and around 70 mA of photocurrent was produced from each diode in the unlocked state. This level of photocurrent was used due to saturation problems if higher power levels were incident on the photodiode. The primary cavity storage time at 120μs was lower than in the measurement with the NPRO as the light source, due to contamination of the mirrors. The spectral density of displacement sensitivity is shown in Fig 6.3 and was found to be at a level of $4 \times 10^{-19}\,\mathrm{m}/\sqrt{\mathrm{Hz}}$ around

[1]Peltier cooling assembly designed and built by A. McKellar

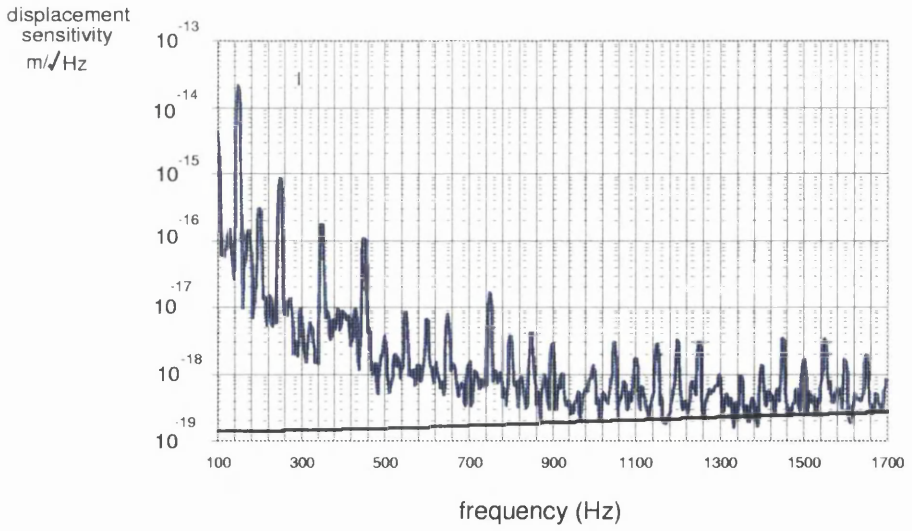

Figure 6.3: *Spectral density of displacement sensitivity obtained using the injection locked laser as the light source and high power acceptance photodiodes. The solid line is the shot noise limit.*

1 kHz.

The shot noise limit for this measurement was at a level of $\sim 3 \times 10^{-19}\,\mathrm{m}/\sqrt{\mathrm{Hz}}$ at 1 kHz so this is not the limiting noise source. More likely is that the contributions from the shot noise and thermal noise combine to limit the measurement. Thermal noise as described in Chapter 1 arises through random thermal positional fluctuations of the atoms in the mirror. In this experiment with the injection locked laser the magnets were bonded to the rear of the secondary outboard mirror with superglue. Using superglue is likely to lower the Q-factor of the mass internal modes and degrade the displacement sensitivity limited by thermal noise. A measurement of the Q-factor of the secondary outboard mass found the Q-factor of the fundamental mode to be around 3.6×10^4 [86]. This would produce a spectral density of thermal noise from this mirror of $2 \times 10^{-19}\,\mathrm{m}/\sqrt{\mathrm{Hz}}$ around 1 kHz [87] and gives an approximate thermal noise level for the detector. The Q-factors of the other mirrors were not measured, but given that they do not have large magnets glued to them,

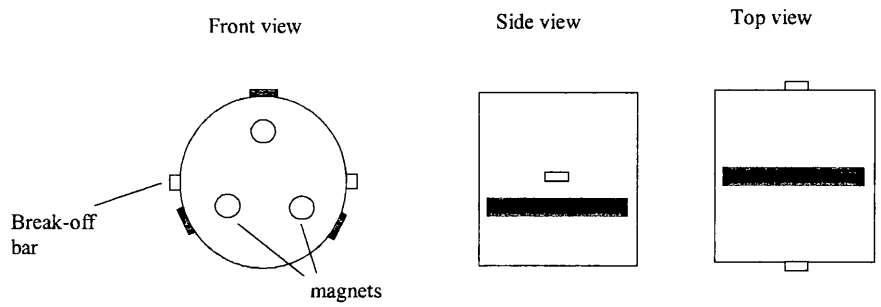

Figure 6.4: *Position of the smeared grease applied to the mirror mass.*

their contribution to the total thermal noise is believed to be less and will be ignored [2]. The combination of the thermal noise and the shot noise at a level of $3 \times 10^{-19}\,\mathrm{m}/\sqrt{\mathrm{Hz}}$ gives a spectral density of noise approximately consistent with the measurement and explains why the shot noise limit was not reached.

6.5 Direct measurement of thermal noise

The spectral density of displacement sensitivity limited by thermal noise in the 1 kHz region is degraded if the Q-factors of the internal modes of the mirror are reduced. As previously discussed magnets bonded to the mirror mass have a detrimental effect on the Q-factor, and a more severe effect can be observed if grease is applied to the mirror to damp the internal modes.

Apiezon vacuum compatible grease was applied to the secondary outboard mirror. This mass, already having the magnets bonded to its rear, was thought to have the lowest Q-factor of its internal modes. The grease was applied in three broad stripes as in Fig 6.4 and Fig 6.5 to maximally damp the internal modes. The spectral density of displacement sensitivity was then measured again and the results of this measurement and the measurement discussed

[2]There are small magnets bonded to the outboard mirror of the primary cavity for calibration purposes, but they are very small in comparison to those bonded to the secondary outboard mirror

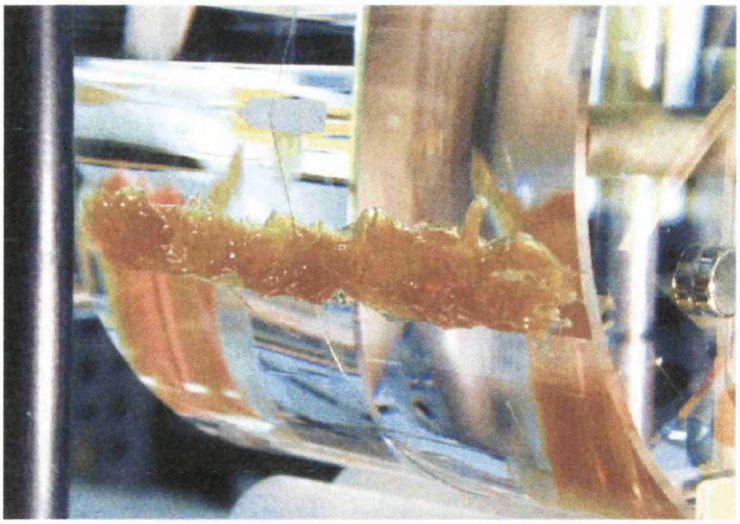

Figure 6.5: *One of the strips of grease applied to the mass.*

previously are shown in Fig 6.6 over a wide bandwidth and Fig 6.7 at low frequencies. There is clearly broadband noise limiting the spectral density of displacement sensitivity to $\sim 2 \times 10^{-18}\,\mathrm{m}/\sqrt{\mathrm{Hz}}$.

A measurement of the quality factor of the internal modes of the mirror with the grease applied [88] showed that the added damping provided by the grease had reduced the quality factor of the fundamental mode by over a factor of ten. It is believed that the limiting noise noise is now the thermal noise of the mirror mass.

6.6 Conclusions

A spectral density of displacement sensitivity of $5 \times 10^{-19}\,\mathrm{m}/\sqrt{\mathrm{Hz}}$ was measured using the NPRO as the light source. This was limited by shot noise in the detected light. This was the first shot noise limited displacement sensitivity obtained using an infra-red laser as the light source. Published results can be found in [89]. With the injection locked laser as the light source a slightly improved level of spectral density of displacement sensitivity of $4 \times 10^{-19}\,\mathrm{m}/\sqrt{\mathrm{Hz}}$

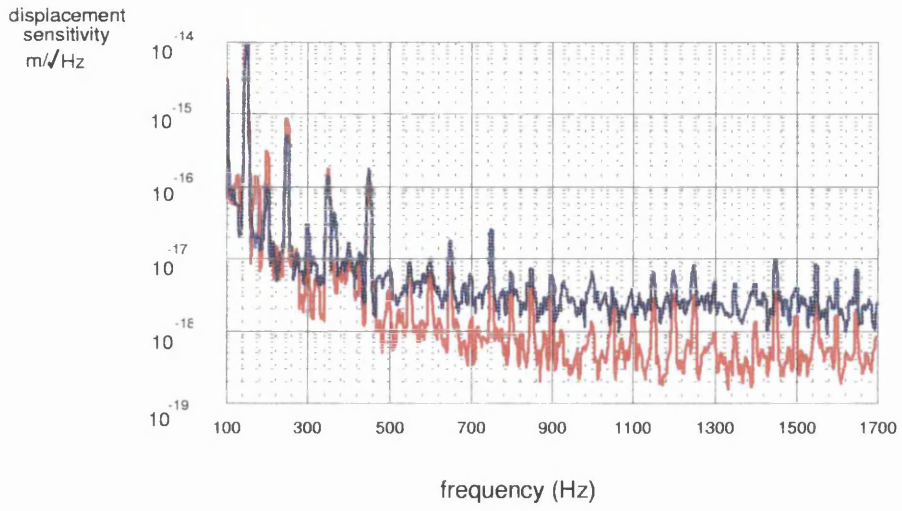

Figure 6.6: *Spectral density of displacement sensitivity measured with injection locked laser in previous experiment (red) and with grease applied to secondary outboard mirror mass (blue).*

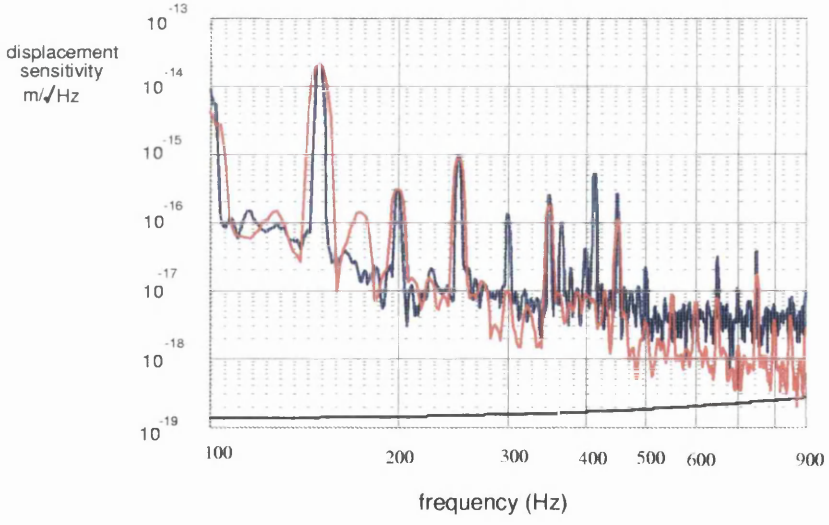

Figure 6.7: *Low frequency spectral density of displacement sensitivity measured with injection locked laser in previous experiment (red) and with grease applied to secondary outboard mirror mass (blue). The shot noise limit is the black line.*

was attained, limited by a combination of shot noise and thermal noise. This is again a crucial experimental step for interferometric gravitational wave detectors and demonstrates for the first time close to shot noise limited performance using an injection locked laser. Published results can be found in [90]. The Q-factor of the secondary outboard mass was lowered by smearing grease on the mirror mass and the thermal noise limited sensitivity was found to be at a level of $\sim 2 \times 10^{-18}\,\mathrm{m}/\sqrt{\mathrm{Hz}}$. This shows that off resonance thermal noise can be measured directly using an instrument of this type. Damping the quality factor of the internal modes severely compromises the detector sensitivity limit due to the thermal noise. This opens up the possibility of measuring thermal noise and testing models of thermal noise behaviour, allowing a better understanding of the phenomenon to be obtained.

Chapter 7

Calibration of prototype detector using radiation pressure

7.1 Introduction

The calibration method for the detector described in Chapters 4 and 6 used a coil/magnet arrangement to introduce a time varying length change to the primary cavity, thus introducing a modulation to the stabilised laser frequency. The magnitude of this frequency modulation was then calibrated by observing the feedback signal to the AOM, the frequency actuator in the band of interest. This method produced a reliable calibration of the detector sensitivity but has the disadvantage that the magnets bonded to the mirror in the primary cavity, lower the Q-factor of the internal modes of the mirror [91]. This reduction in Q-factor can degrade the displacement sensitivity limit set by thermal noise in the detector.

Large scale interferometric gravitational wave detectors may use similar techniques to calibrate the displacement sensitivity of the detector. One arm length

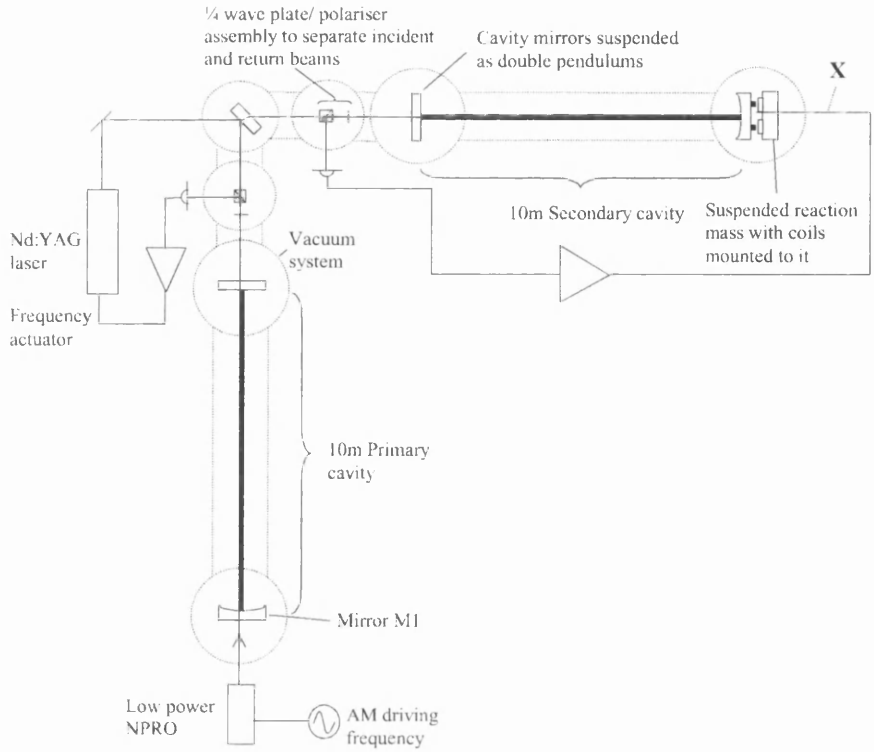

Figure 7.1: *A schematic of the Glasgow prototype gravitational wave detector. Frequency stabilisation schemes are simplified for clarity.*

will be changed relative to the other by a determinable amount. Radiation pressure has been suggested as a method of moving a cavity mirror in the LIGO and GEO detectors and varying the length of one arm [92, 93]. This technique has the advantage that it does not require any mirrors to be altered thus maintaining the Q-factor of the mirror internal modes. To verify the validity of this method for calibrating large scale gravitational wave detectors, an experiment to calibrate the prototype detector in this way was performed.

7.2 The experiment

To apply the radiation pressure, light from a low power Lightwave NPRO [47] was incident on the mirror labeled M1 in Fig 7.1. The light was reflected

at the rear of the highly reflecting coating applied to the front face of the mirror. The laser power was amplitude modulated at a particular frequency so that any displacement of the test mass resulting from the radiation pressure was seen as peak at this frequency in the spectrum of the spectral density of displacement sensitivity of the detector. The Lightwave NPRO can be amplitude modulated to a modulation depth of 100% at frequencies of interest and a $160\,\mathrm{mW_{peak}}$ output is obtained. Since the test mass is suspended as a pendulum, as described in Chapter 2, the expected response to the modulated laser light is readily estimated. The displacement of the mass is obtained from

$$\ddot{x} + \frac{\gamma}{m}\dot{x} + \omega_0^2 x = \frac{F(t)}{m} \tag{7.1}$$

where γ is the damping constant, ω_0 is the fundamental frequency of the pendulum, m is the mass of the test mass and $F(t)$ is the time dependent force resulting from the modulated radiation pressure. $F(t)$ is then given by

$$F(t) = \frac{2P_0}{c}[1 + \sin(\omega_m t)] \tag{7.2}$$

where P_0 is the un-modulated laser carrier power, c the velocity of light and ω_m is the angular modulation frequency. For $\omega_m \gg \omega_0$ and $\omega_m^2 \gg \frac{\gamma\omega_m}{m}$ the displacement $x(t)$ has the form

$$x(t) = \frac{2P_0}{mc\omega_0^2} + \frac{2P_0}{mc\omega_m^2}\sin(\omega_m t - \phi) \tag{7.3}$$

where ϕ is a phase shift of $\sim \pi$. The rms value of the time dependent component of the displacement is therefore

$$x_{rms} = \frac{2P_0}{\sqrt{2}mc\omega_m^2}. \tag{7.4}$$

7.3 Calibration

The displacement sensitivity of the detector is derived from the signal fed to the coils in the reaction pendulum in Fig 7.1, which represents differential length

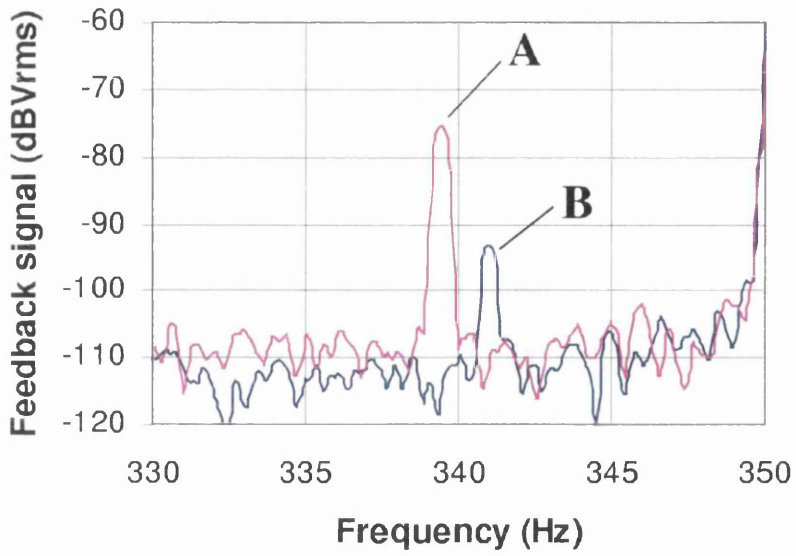

Figure 7.2: *Power spectrum of the feedback signal to the secondary cavity end mirror with calibration peaks applied. Spectra are for application of peak via coil/magnet arrangement at 339 Hz (labeled A) and via radiation pressure at 342 Hz (labeled B).*

change between the two Fabry-Perot cavities. This signal can be calibrated by varying the length of the primary cavity and using the AOM feedback signal or by the static mirror response method described in Chapters 4 and 6.

To calibrate the displacement resulting from radiation pressure, the mirror M1 was moved at a frequency ω_m by using radiation pressure. This produced a peak in the spectral density of displacement sensitivity. The displacement corresponding to this peak was then calibrated by applying a determinable displacement at $\omega_m - 3$ Hz by means of the coil magnet arrangement. A sample of the results is shown in Fig 7.2. These spectra show the feedback signal at X with mirror M1 moved by the coil/magnet arrangement and by the radiation pressure scheme. The relative height of the two peaks allows the motion resulting from radiation pressure to be calculated.

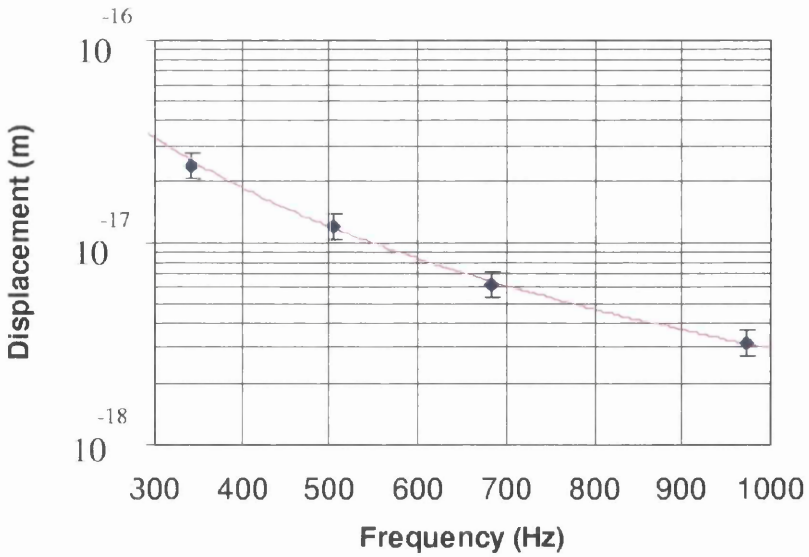

Figure 7.3: *Calibrated motion of mirror resulting from radiation pressure at different frequencies. Also shown is predicted response.*

7.4 Results

The calibration described above was performed at a number of different modulation frequencies. The resulting calibrated mirror motion is shown in Fig 7.3 at each frequency. Also shown is the predicted response based on Equation 7.4. The radiation pressure induced displacement can be seen to follow the theoretical prediction within error proving its validity as a method of calibrating interferometric gravitational wave detectors.

7.5 Conclusions

Radiation pressure has been demonstrated as a valid non-intrusive method of detector calibration. The results agree with the prediction of mirror motion for a given radiation pressure and modulation frequency based on a simple model of the pendulum. Using this technique the calibration peak from the

radiation pressure can be left as a permanent marker without degrading the detector sensitivity. This is the first time a fully suspended prototype detector has been calibrated using this technique. Published results can be found in [94].

Chapter 8

Evaluation of optical components for GEO 600

8.1 Introduction

Gravitational wave detectors require very high quality optical components, some of which must be specially manufactured given the stringent specifications. Of particular importance are polarisers and electro-optic modulators, each of which play a crucial role in interferometry. LEYSOP [95] manufactured these components for use in GEO 600 and the optics were first tested in the Glasgow prototype interferometer. This chapter contains a summary of the properties of these components.

8.2 Polarisers

Many polarisers are to be used serially in GEO 600, individually and as part of other optical components. To avoid attenuating the laser power, it is important that the polarisers have a very small insertion loss. Further to ensure highly polarised light enters the interferometer, the extinction ratio given by the polariser must be high. LEYSOP manufactured calcite polarisers designed

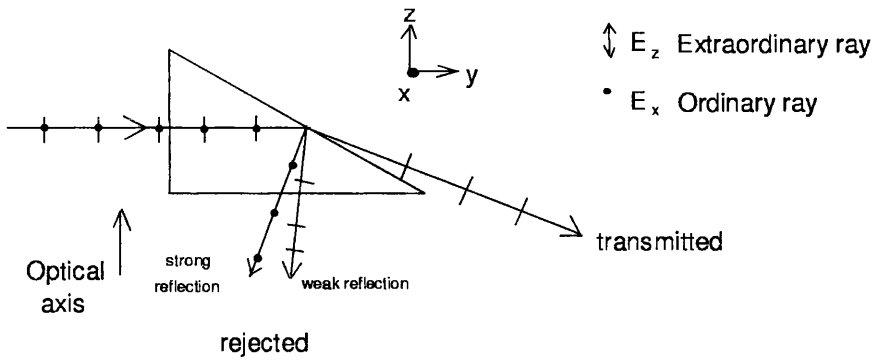

Figure 8.1: *The GEO 600 polarising prism.*

to meet these requirements, utilising the low bulk absorption of calcite at 1064 nm and the quality of the crystal which allows high extinction ratios to the achieved.

Calcite is a uniaxial birefringent crystal and light polarised parallel to the optic axis is an extraordinary ray ($n_e = 1.47$) while light polarised perpendicular to the optic axis is an ordinary ray ($n_o = 1.64$). A diagram of a GEO 600 polarising prism is shown in Fig 8.1 and is similar to a Glan-Thomson polariser. Laser light enters the prism at normal incidence. The ordinary and extraordinary rays then encounter different refractive indices as they pass through the polariser, and at the angled output face, the ordinary ray is totally internally reflected while the extraordinary ray is transmitted. This splitting separates the two orthogonal polarisations so polarises the laser light.

The polarisers are generally used in transmission so an anti-reflection coating is required on both input face and the angled output face.

A power meter was used to measure the loss encountered by the transmitted polarisation. Using approximately 500 mW of polarised laser light, the power before and after the polariser was measured. The loss was measured to be $\sim 0.4 \pm 0.1\%$.

The disadvantage of the polarising prism is that the laser beam is angularly deviated after passage through it. To overcome this problem, two prisms

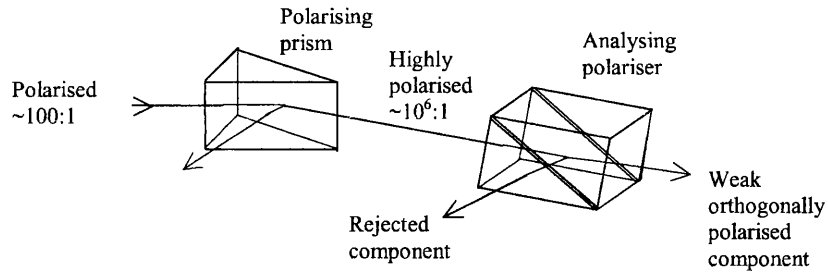

Figure 8.2: *Experiment to measure the extinction ratio of the assembled polariser.*

can be placed back to back, with a small air gap between them, the second compensating for the angular deflection.

The combined loss for this assembled polariser was measured to be $\sim 1 \pm 0.1\%$ with the 500 mW laser, and a similar measurement was obtained using 10 W of laser power in experiments performed at the Laser Zentrum Hannover [1].

Further the extinction ratio was measured using the 10 W laser, as shown in Fig 8.2. A polarising prism first polarised the laser light and an assembled polariser analysed the resulting polarisation state. The highly polarised light enters the analysing polariser and is dominantly rejected from the angled face. The residual orthogonally polarised component is transmitted through the assembled polariser. The extinction ratio was found by careful measurement of this transmitted light. The ratio of input power to transmitted power gives the extinction ratio measured to be $> 10^6$.

These polarisers meet the specifications for use in GEO 600.

[1] A prototype GEO 600 laser was used and the experiment was performed with the assistance of O.S. Brozek.

8.3 Brewster prism

The dominant transmission loss associated with the prisms described above was believed to be caused by imperfections in the anti-reflection coatings. A polarising prism which does not require anti-reflection coatings, yet gives improved performance was designed by Dr. G. Newton. It uses Brewsters angle to minimise the losses encountered at each face.

Its operation can be understood from Fig 8.3. An unpolarised laser beam enters the prism and in this case, because the incidence angle is not normal, the two orthogonal polarisations are split. Generally the polariser is used in transmission, so the prism angles are selected such that the transmitted extraordinary ray is incident on both the input face and the output face at Brewsters angle. If the optic axis is aligned as shown in Fig 8.3 then the angle between the two polarised components is maximised and the ordinary ray is totally internally reflected [96]. Careful alignment of the polariser is crucial to obtain best performance, given that the critical angle for total internal reflection is 37.52^o and the ordinary ray is incident on the output face at 37.70^o.

Initial experiments to measure the transmission loss using a technique described previously, demonstrated that the prism was performing as expected. The measured loss was largely dominated by experimental error, so to characterise the prisms performance, a more accurate measurement technique was needed. A second identical Brewster prism was used to produce an assembled polariser in the same way as the GEO 600 polariser. This assembled polariser did not change the angle of the incident laser beam, although the laser beam was now offset after transmission. The loss of this assembled polariser was measured using a technique developed for measurements of ultra-low loss super-mirrors [97]. The measurement involved placing the assembled polariser in a high finesse Fabry-Perot cavity. The decay time for the cavity

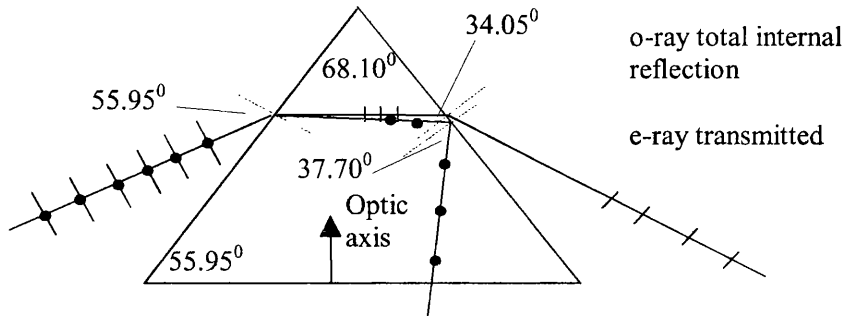

Figure 8.3: *The Brewster prism.*

was measured and compared to that for the high finesse cavity without the intra-cavity polariser. The change in the storage time gives information on the extra intra-cavity loss and hence the loss associated with the polariser. Using this technique the transmission loss for a highly polarised and well collimated laser beam was measured to be 220 ± 80 ppm.

The extinction ratio was measured in a similar way to that of the GEO 600 polariser to be $> 3 \times 10^6$.

These prisms are more difficult to use given the high degree of alignment required for optimal performance, but the low insertion loss coupled with high extinction ratio makes them very useful where power loss is an important factor.

8.4 Electro-optic modulators

GEO 600 electro-optic modulators must have low insertion loss to maximise power throughput, so good anti-reflection coatings are required on all faces. The absorption loss must be low to minimise thermal lensing effects. Further, the effect on the laser phase front should be minimal and a low half wave voltage is desirable to allow a large modulation index to be achieved.

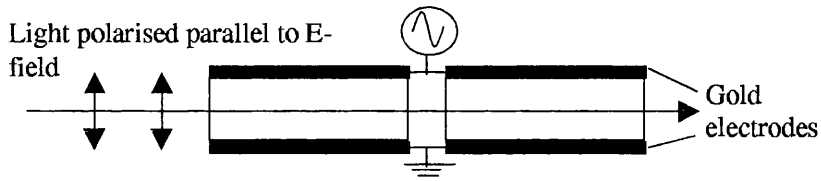

Figure 8.4: *The Leysop modulator.*

8.4.1 Insertion loss

Wide aperture $LiNbO_3$ electro-optic modulators manufactured by LEYSOP were tested. $LiNbO_3$ has a refractive index of ~ 2.2 at 1064 nm so at normal incidence $\sim 14\%$ of the incident light is reflected. The modulators are assembled as shown in Fig 8.4 so there are four air/crystal boundaries. The aperture is 8 mm, considerably larger than other commercially available modulators. A good AR coating is needed to reduce the insertion loss to acceptable levels. The reflection coefficient from the AR coated surface was initially measured to be poor but was improved to less than 1% with a different coating.
Based on the reflection loss measurements an estimate of the absorption loss could be made by measuring the fraction of light transmitted through the modulator. The absorption loss for the modulator was estimated to be less than 0.8% or ~ 1500 ppm/cm.

8.4.2 Electro-optic properties

The capacitance of the $LiNbO_3$ modulator at ~ 20pF was found to be comparable to the capacitance of a GSANGER PM25-IR modulator. PM25 modulators are commonly used for IR applications and it was useful to compare the electro-optic properties of each type. A resonant circuit shown in Fig 8.5 was built to generate the high voltages required to drive the modulators. Since the $LiNbO_3$ and PM25 modulators were of similar capacitance they were interchangeable in the resonant circuit. An HP generator provided the RF signal

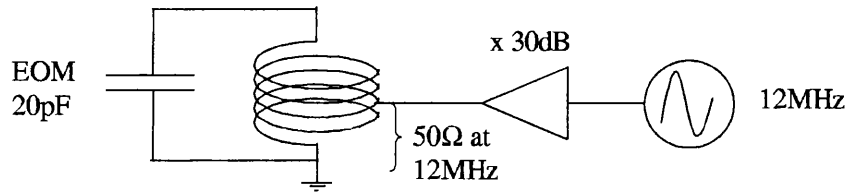

Figure 8.5: *Resonant circuit to drive electro-optic modulators.*

and a Motorola RF amplifier gave 30 dB of gain. A SWR/RF power[2] meter was used to optimise the impedance matching and measure the forward power. A 50 Ω co-axial cable linked the resonant circuit to the driving electronics.

Two PM25-IR modulators were tested to assess how much modulation depth was attainable. The modulation depth is characterised by the modulation index β in Equation 2.21. The forward power measured on the rf-power meter was 1 W in each case and the modulation depth was measured by viewing the optical carrier and sidebands with a scanning Fabry-Perot cavity as shown in Fig 8.6. From Equation 2.22 the ratio of sidebands to carrier is given by

$$\frac{(J_1(\beta))^2}{(J_0(\beta))^2}$$

allowing the modulation index β to be calculated. For the PM25 modulator with 1 W of RF power driving the resonant circuit the modulation index was 0.25 rad.

The $LiNbO_3$ modulator was inserted in the same circuit and the tuning optimised by squeezing the transformer coil slightly and making a small change to the modulation frequency. Again 1 W of forward power was measured on the rf-power meter. The carrier and sidebands can be seen in Fig 8.6. Now the carrier is almost completely suppressed and out to the fourth order sideband can be seen. This corresponds to a modulation index of 2.3 rad.

The half-wave voltage of the $LiNbO_3$ modulator was measured as shown in Fig 8.7. The voltage required across the modulator crystal to take the trans-

[2]Standing Wave Ratio

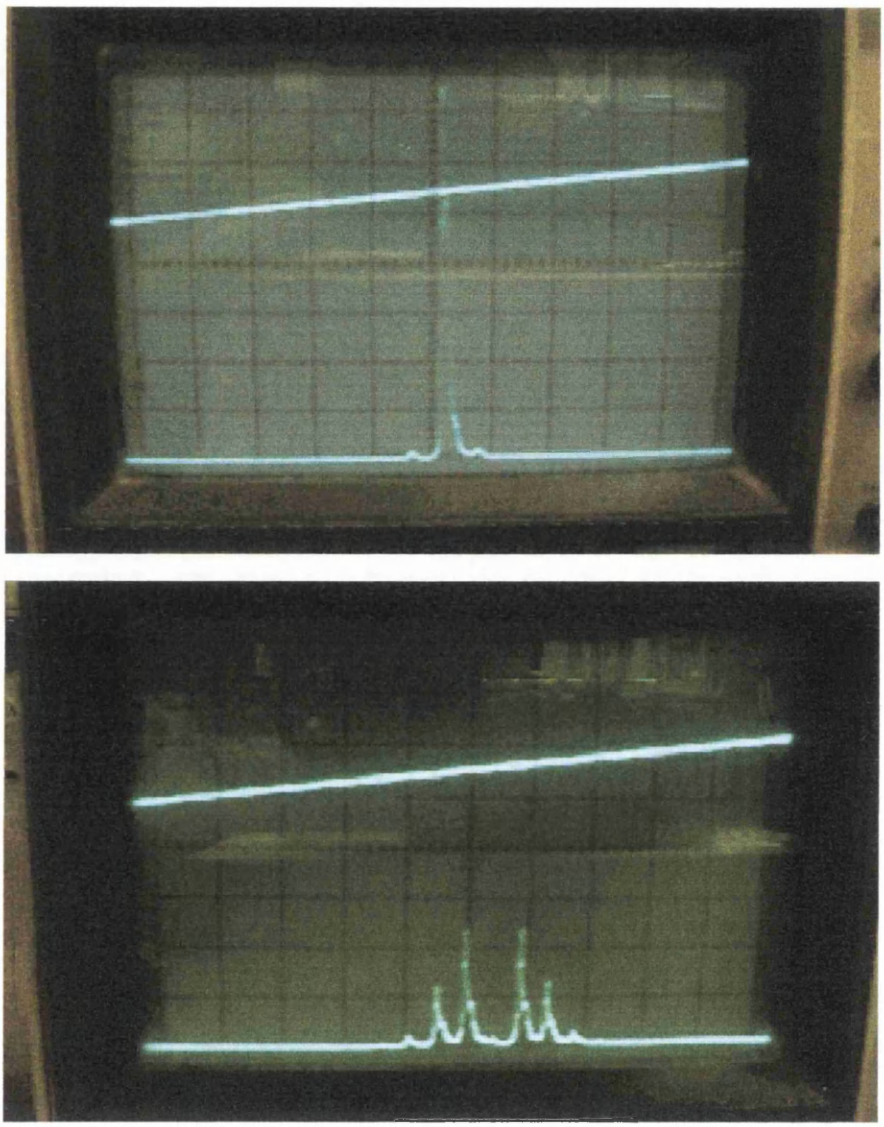

Figure 8.6: *Modulation levels measured with a scanning Fabry-Perot cavity using PM25 (top) and* $LiNbO_3$ *(bottom).*

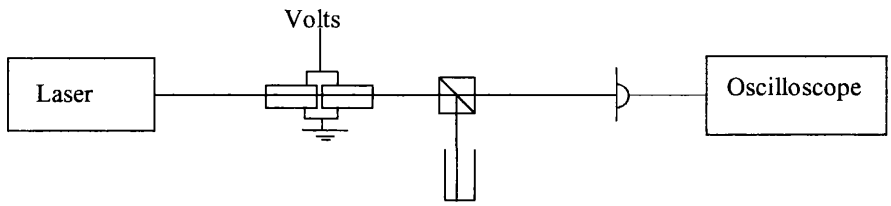

Figure 8.7: *Experiment to measure the half-wave voltage of the* $LiNbO_3$ *modulator.*

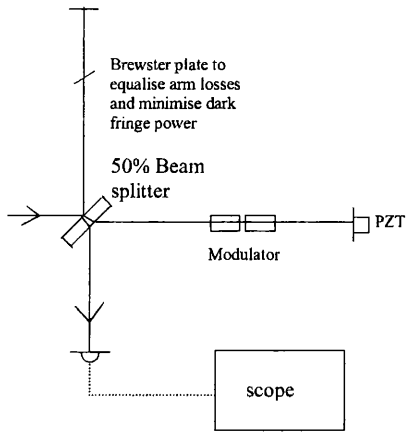

Figure 8.8: *The Michelson interferometer used to test for beam distortions.*

mitted light through the polariser from minima to maxima is the half-wave voltage. It was found to be 600 V.

The PM25-IR modulators are limited to applying small modulation depths with typical relative optical carrier to sideband ratios of over 100. The $LiNbO_3$ modulator however can produce modulation depths well above those required by GEO 600 with easily attainable RF power levels.

8.4.3 Phase front distortion measurements

The phase front distortion was measured using a Michelson interferometer as in Fig 8.8. The length of each arm was 50 cm. The light source was the NPRO with a beam diameter (2w) of 1.5 mm at the beam splitter.

The Michelson interferometer was first tested without the modulator in place.

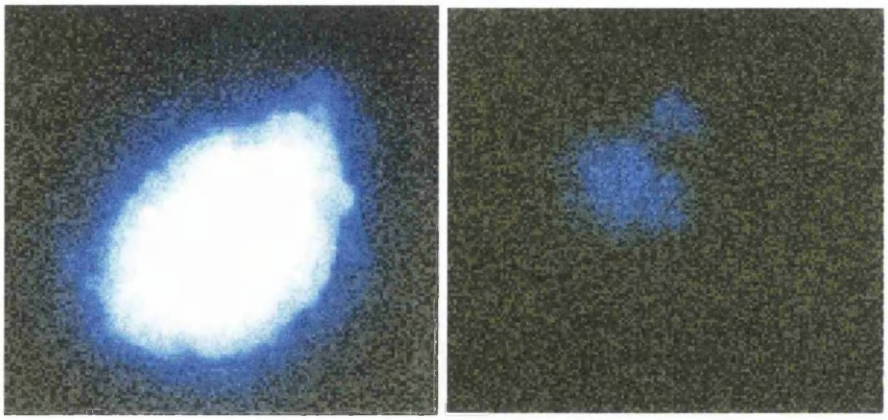

Figure 8.9: *Bright and dark fringe obtained with EOM in one arm.*

The dark fringe intensity was measured to be less than 0.1% of the bright fringe, by sweeping the length of one arm with a PZT and viewing the intensity of the fringe pattern on an oscilloscope. A Brewter plate was used to equalise the optical loss in each arm.

With the modulator in one arm of the interferometer, the other arm length was shortened to optimise the interfering beam sizes at the beam splitter. The dark fringe power was minimised by rotating the Brewster plate. This produced the best cancellation of the TEM_{00} mode by compensating for the loss imposed by the modulator. The resulting dark fringe power was 1.8% that of the bright fringe indicating that $\sim$ 1.7% of the laser power was contained in high order modes after double passing the $LiNbO_3$ modulator. The bright fringe and dark fringe intensity profiles are shown in Fig 8.9

The Michelson interferometer was slightly misaligned to show linear fringes. Any phase front distortions not common to both arms of the interferometer would distort the fringe pattern. The resulting fringe patterns showed no evidence of distortion.

The modulator was rotated slightly from normal incidence during the experiments to prevent reflections from the AR coated faces interfering.

8.5 Conclusions

The polarisers have been shown to meet the requirements for GEO 600 in terms of their optical losses and extinction ratio. The experiments with the novel Brewster polariser have demonstrated the possibility of making a very low loss polariser with no anti-reflection coatings on input or output face. This may become important in the future when very high power lasers are used in upgraded interferometric gravitational wave detectors, which could damage optical coatings. The suitability of the large aperture $LiNbO_3$ electro optic modulators for use in GEO 600 was demonstrated. Their optical and electro-optical properties meet the requirements. Published results based on this chapter can be found in [98]

Chapter 9

Narrow-band phase noise measurement around an electro-optically applied rf phase modulation of a laser field

9.1 Introduction

The frequency stabilisation schemes described previously used rf-reflection locking [34] to derive an error signal centred on the resonant frequency of a reference cavity. In these schemes a $LiNbO_3$ electro-optic modulator was driven with an rf signal to provide phase modulation of the laser light. In the case of Fig 4.1 noise sources associated with the phase modulating process could degrade the resulting frequency stability. Amplitude modulation of the laser light due to, for example misalignment of the optic axis of the modulator crystal and the polarisation vector of the light, combined with polarisation sensitive optical components is well known. What is less clear is whether phase noise over and above that of the intrinsic phase noise of the oscillator will be

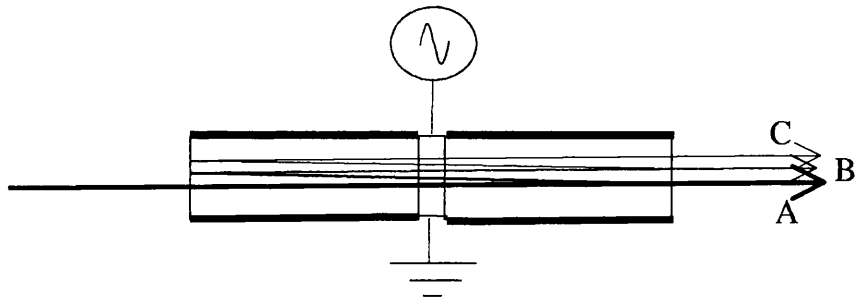

Figure 9.1: *The* $LiNbO_3$ *phase modulator showing how multiple reflections could introduce phase noise.*

imparted on the laser light.

This additional phase noise around the modulation frequency could arise through a number of mechanisms. Consider Fig 9.1 which shows one of the $LiNbO_3$ electro-optic modulators described in Chapter 8. The electro-optic crystal end faces are not perfectly anti-reflection coated, so light can be reflected between the end faces of the crystal. The light rays labeled A,B and C have each traveled a different distance and will have different phase properties. A similar effect can be produced if there is beam jitter on the laser beam. The laser field will travel a different distance through the crystal depending on the angle it enters the modulator, producing a time varying modulation depth. This could lead to phase noise in addition to that of the oscillator. Crystal imperfections could also lead to some additional phase noise.

9.2 Experimental method

Fig 9.2 shows the schematic layout of the main components used in the measurement. The NPRO was used as the laser source. It is necessary that beam geometry fluctuations, and in particular beam pointing, be suppressed as they would lead to a fluctuating path through the modulator and to a variable phase delay. For this reason the laser field was passed through a single mode

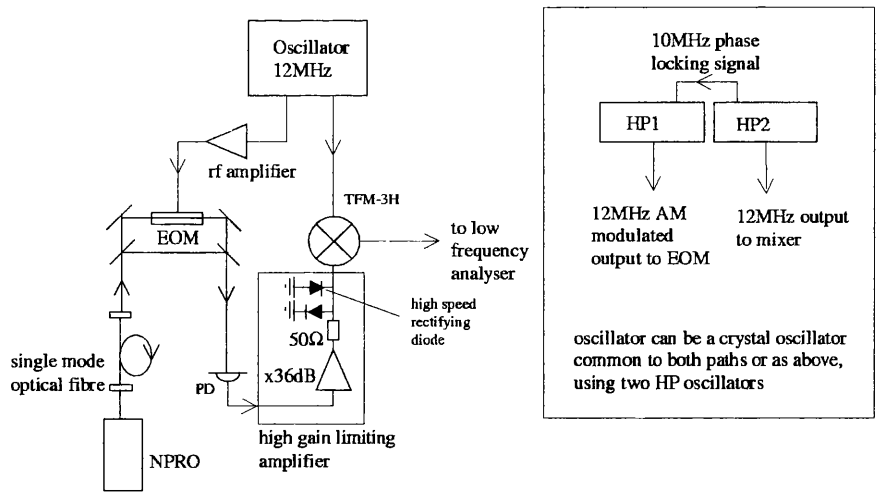

Figure 9.2: *Optical arrangement for the experiment. The oscillator can be changed from a crystal oscillator to two phase locked HP signal generators.*

optical fibre to suppress beam geometry fluctuations before being phase modulated at 12 MHz using the $LiNbO_3$ electro-optic modulator. A beam splitter placed before the modulator split off a portion of the laser field which was later combined with the field that had passed through the modulator. The recombination took place on a second beam splitter placed after the phase modulator. The recombined field was then detected using an EG&G InGaAs photo-diode. The resulting photocurrent consisted of two parts, a DC component due to the laser power and a rf component due to beating between the modulated and unmodulated laser fields. A wide bandwidth pre-amplifier and filter separated the rf component at 12 MHz. Should the phase modulating process impose phase noise on the laser field this would be seen on a rf spectrum analyser as a broadening of the 12 MHz carrier. It is possible to increase significantly both the resolution and sensitivity by mixing the 12 MHz signal from the detector circuit with a pure local oscillator also at 12 MHz. To ensure that the fluctuating output of the mixer is due to relative phase fluctuations between the rf signal and local oscillator, amplitude noise in the rf signal was suppressed. This was achieved using a high gain limiting amplifier placed before the mixer.

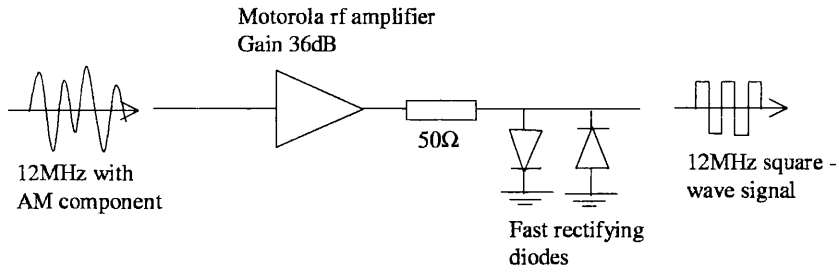

Figure 9.3: *The limiting amplifier used to remove AM from the rf signal.*

The limiting amplifier is shown in Fig 9.3 and it produced an approximate square-wave, $\sim 1.5V_{p-p}$ rf signal. Rf filtering was required after the mixer to remove residual rf components of the mixer output signal.

9.3 Calibration

The laser field exiting from the phase modulator has the form

$$E_{opt} = E_{0,opt} \sin(\omega t + \beta \cos(\omega_{rf} t)) \tag{9.1}$$

where β is the phase modulation index and ω_{rf} is the angular frequency of the rf drive. Expansion of Eq 9.1, shows that the laser field will contain side bands at $\omega_{opt} \pm \omega_{rf}$, $\omega_{opt} \pm 2\omega_{rf}$ etc. Further the relative amplitude of the first order side band to the amplitude of the optical carrier is given by $\frac{(J_1(\beta))^2}{(J_0(\beta))^2}$, where $J_n(\beta)$ are Bessel functions as described previously. By using an optical spectrum analyser, the relative height between the 12 MHz side bands and the optical carrier can be measured and is shown in Fig 9.4. This allowed the modulation index β to be determined. To provide a calibration marker against which the phase noise background can be measured, two 12 MHz oscillators[1] were used. The first was used to drive the phase modulator and the second provided the local oscillator input to the mixer. The 12 MHz carrier frequencies of the two

[1]Hewlett Packard model HP-33120A

oscillators were phase locked by injecting a common 10 MHz reference signal into each oscillator. A calibration peak was then generated by applying a low level amplitude modulation (AM) to the 12 MHz drive to the phase modulator. The optical field then has the form

$$E_{opt} = E_{0opt} \sin[\omega_{opt} t + \beta(1 + \alpha \cos(\omega_m t)) \cos(\omega_{rf} t)] \tag{9.2}$$

where α is the amplitude modulation index and ω_m is the frequency of the amplitude modulation. Expansion of Eq 9.2 shows that ω_{opt} is now driven at three frequencies namely $\omega_{rf}, \omega_{rf} + \omega_m$ and $\omega_{rf} - \omega_m$. The laser field now takes the form

$$E_{opt} = E_{0opt} \sin\left\{\omega_{opt} t + \beta[\cos(\omega_{rf} t) + \frac{\alpha}{2}(\cos(\omega_{rf} - \omega_m)t + \cos(\omega_{rf} + \omega_m)t)]\right\}. \tag{9.3}$$

The additional frequencies appear as sidebands about the rf carrier frequency. The rf signal from the photodiode was analysed using an rf spectrum analyser[2] and a typical result is shown in Fig 9.5. The height of the amplitude modulation sidebands relative to the rf carrier allows the level of phase modulation due to the amplitude modulation at ω_m to be calculated. Subsequent measurement of the background noise relative to the calibration peak in Fig 9.6, using a low frequency high resolution spectrum analyser[3] yields an estimate of the upper limit to the additional phase noise amplitude spectral density imposed by the phase modulator.

9.4 Results and Discussion

From Fig 9.4 the height of the 12 MHz sidebands are seen to be 1/6 of the optical carrier, giving a phase modulation index of $\beta = 0.76$. Fig 9.5 shows the 520 Hz calibration marker to be 45 dBv below the 12 MHz side band and Fig 9.6

[2]Hewlett Packard model HP-8591E

[3]Stanford Research Systems model SR780

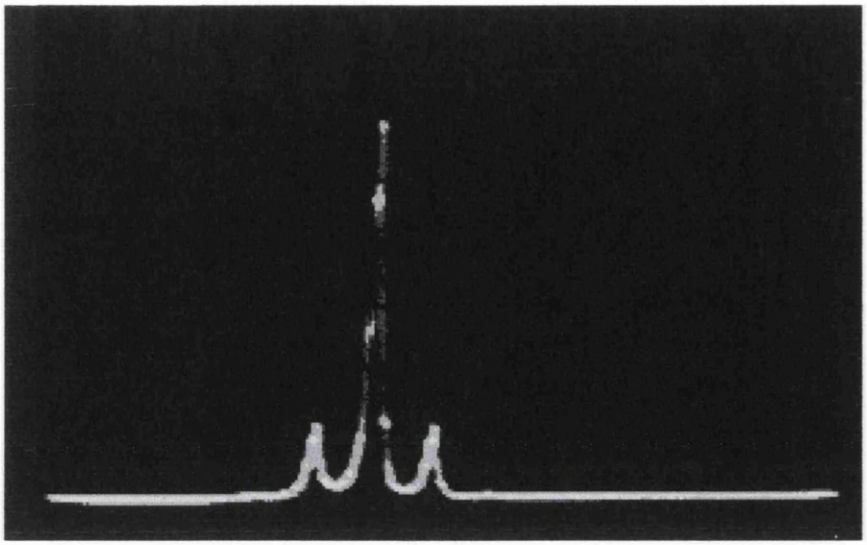

Figure 9.4: *Modulated carrier with 12 MHz sidebands as viewed with a scanning Fabry-Perot optical spectrum analyser.*

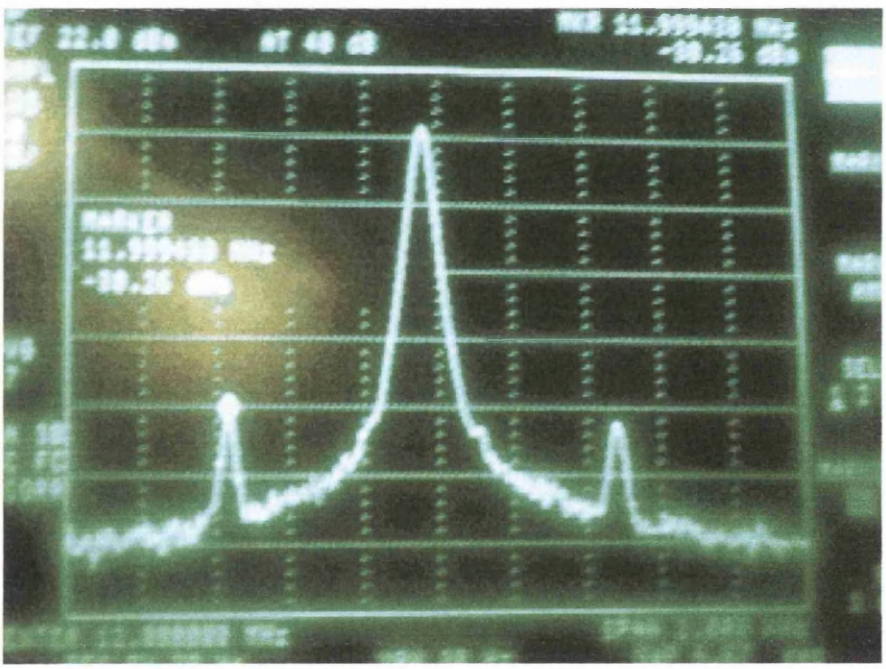

Figure 9.5: *12 MHz signal with calibration sidebands at* 12 MHz ± 520 Hz. *Vertical scale is 10 dB/div.*

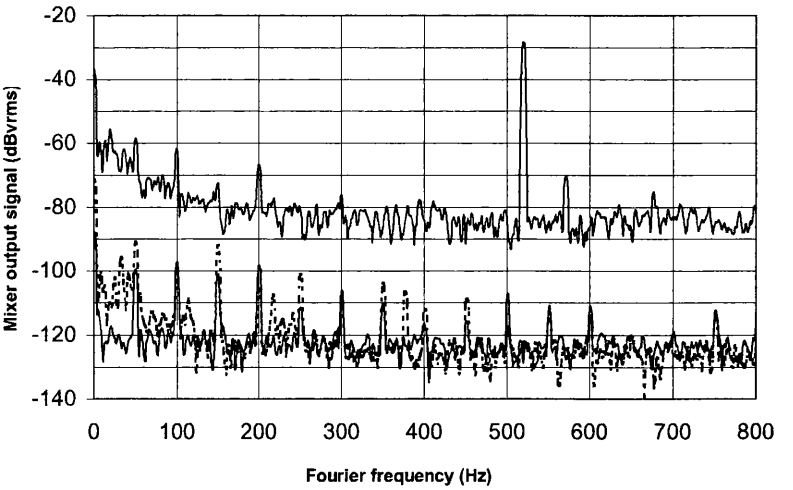

Figure 9.6: *The upper spectrum shows the 520 Hz calibration peak generated using two phase locked oscillators, one AM modulated driving the phase modulator, the other unmodulated supplying the reference input to the mixer. The lower dashed spectrum shows the additional phase noise amplitude spectral density when the phase modulator and mixer are driven by a low noise crystal oscillator of the type to be used in large scale gravitational wave detectors. The lower solid spectrum shows the electronic noise in the detection electronics.*

shows the background noise level (dashed lower spectum) above 150 Hz to be 95 dBv below the calibration marker. Also shown in Fig 9.6 is a spectrum of the noise associated with the measurement electronics (solid lower spectrum). This is seen to be flat over the 800 Hz measurement interval. These measurements set an upper limit to the phase noise amplitude spectral density of $4 \times 10^{-8}\,\mathrm{rad}/\sqrt{\mathrm{Hz}}$.

Fig 9.7 shows both the GEO 600 specification for phase noise around the modulation frequency and also the measured level. The GEO 600 specification was produced using FINESSE [99] an optical modeling package [100]. The calculation is based on assuming perfect interferometer contrast such that the shot noise in the detected light is due to the phase modulation sidebands. If

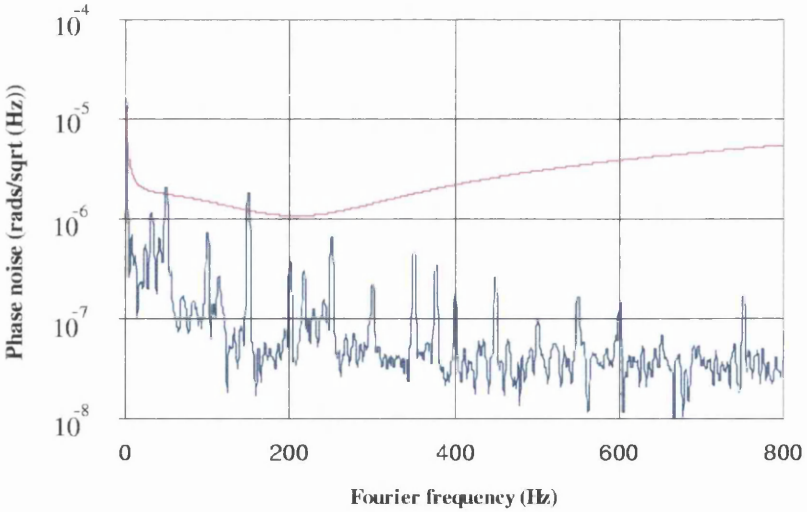

Figure 9.7: *Phase noise around the modulation frequency and the GEO 600 phase noise specification. Spikes are mainly due to the UK 50 Hz line frequency. GEO 600 uses a signal recycling technique to obtain best sensitivity at 200 Hz. This leads to the dip in the phase noise budget at that frequency. A numerical simulation of the GEO 600 interferometer allowed the effect of phase noise imposed by the modulation process to be evaluated. This calculation was done using FINESSE an optical modeling program.*

it is assumed a noise contribution a factor of 10 below this level is tolerable, and that this noise is due to phase noise around the modulation frequency, the phase noise specification can be numerically derived. The shaping of the spectrum is due to the coupled cavity arrangement that exists in GEO 600. The power and signal recycling cavities provide filtering of phase noise around the modulation frequency and the lowest specified phase noise at $\sim$ 200 Hz corresponds to GEO 600 most sensitive frequency. The level of phase noise imposed by the modulating process is well below the GEO 600 specification, so the sensitivity of the detector to gravitational waves will not be compromised by this mechanism.

9.5 Conclusions

An upper limit to the amplitude spectral density of additional phase noise imposed on the laser field by an electro-optic modulator around the modulation frequency of 12 MHz was found to be less than $\sim 3 \times 10^{-8}\text{rad}/\sqrt{\text{Hz}}$. This was measured over a bandwidth of 800 Hz from the modulation frequency and was achieved when driving the modulator with an rf signal large enough to achieve a modulation index of 0.76. Published results based on this chapter can be found in [101].

Chapter 10

A single frequency Yb:YAG laser source

10.1 Introduction

Future generations of gravitational wave detectors will require low noise lasers with much higher powers than are currently attainable. LIGO 2 is expected to use a 100 W Nd:YAG laser source [102] in the form of a two stage amplifier system. This technique has been shown to produce the power levels required but for later detector upgrades, Nd:YAG may not be a suitable gain medium. Yb:YAG offers the possibility of producing lasers with CW output powers of tens to hundreds of kilo-watts [103] while maintaining the favourable properties of Nd:YAG.

Yb:YAG absorbs strongly at 940 nm, a region of the spectrum where high power laser diodes are available. YAG can be doped a factor of ten more strongly with Yb than Nd atoms, so higher gain is available from similar sized crystals.

The energy level diagram of the Yb:YAG system is shown in Fig 10.1 with the 4-level Nd:YAG system at 1064 nm for comparison. Note the relative separa-

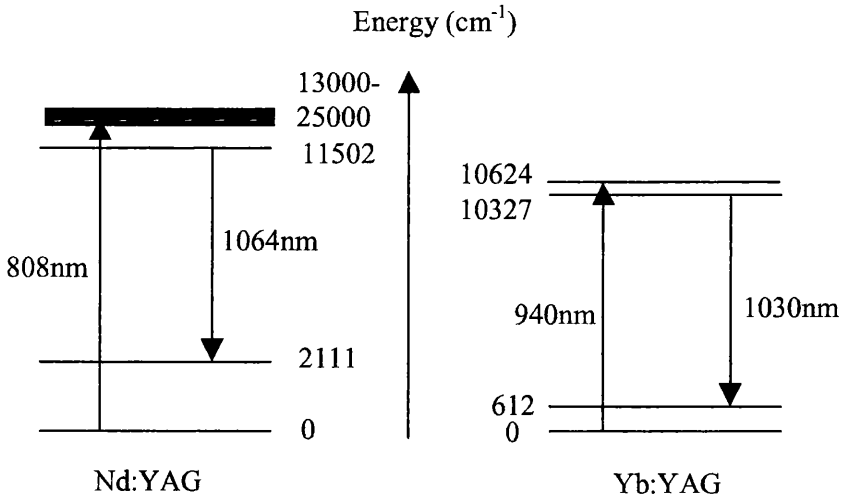

Figure 10.1: *Energy level diagrams for a Nd:YAG and Yb:YAG laser*

tion of ground state and lower laser level in each case. In the 4-level Nd:YAG case the spacing of the levels at 2111 cm^{-1} prohibits thermal population of the lower laser level at room temperature. In the case of Yb:YAG significant thermal population of the lower laser level occurs at room temperature, and for this reason it is known as a quasi 3-level system. The practical consequence of the populated lower laser level is that re-absorption of the emitted 1030 nm radiation can occur. This results in a higher threshold pump power than would be required if the lower laser level was un-populated. Above the lasing threshold a Yb:YAG laser behaves similarly to a 4-level system. The Yb:YAG could be made to behave as a 4-level system if the crystal was cooled and the population of the lower laser level reduced. Yb:YAG has become a viable gain medium recently given the availability of pumping diodes at 940 nm. Flashlamp pumping is not efficient because in contrast to Nd:YAG where many excited states decay to the upper laser level, only one excited state relaxes to the upper laser level.

At the Ginzton Lab, Stanford University a high power diode pumped Yb:YAG laser is being constructed which will be used initially as an oscillator, but

planned experiments will test its performance acting as an amplifier. To probe this amplifier a single frequency Yb:YAG laser source was constructed.

10.2 Design considerations

In a free running solid state laser cavity, the electric field pattern is a superposition of several axial modes, so some technique must be employed to produce oscillation at only one frequency. Spatial hole burning makes single frequency operation in a standing wave cavity difficult to achieve. Spatial hole burning can however be eliminated by producing a unidirectional traveling wave in a ring cavity. This can be achieved by introducing a differential loss between the two counter-circulating traveling waves in a ring laser cavity. The dominant traveling wave will then be in the propagation direction which has the lowest loss. This can be achieved by inserting a Faraday rotator and half wave plate into the cavity. If one mirror acts as a polarisation selector (higher reflectivity of s-polarisation than p-polarisation) then the optic axis of the half wave plate can be optimised, such that no loss is experienced for the light propagating in one direction, while the counter-propagating light is attenuated.
The polarisation rotation given by the half-wave plate can instead be produced by a non-planar reflection at a cavity mirror as is done in commercial NPRO's reducing the number of intra-cavity components and cavity loss.
The aim here was to achieve unidirectional, single frequency operation of a Yb:YAG laser by employing this non-planar ring oscillator technique. A NPRO of the type described in [48] cannot be built due to the low Verdet constant of Yb:YAG.

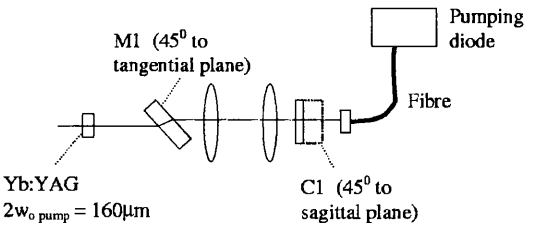

Figure 10.2: *Pumping scheme schematic*

10.3 Pumping scheme

A 3W Opto-power OPC-D003-940 diode was used as the pump source. The diode was water cooled and a re-circulating water cooler allowed temperature and wavelength tuning of the nominal 940 nm output. The diode output was coupled into an optical fibre to give the high brightness pump source required. The light from the fibre was focused to a spot size of 110 μm diameter using two 5 cm focal length lenses. After insertion of the dichroic cavity mirror (M1 in Fig 10.2) the pumping beam was astigmatic and was circularised by introducing an astigmatism compensation plate, C1, in the pump optics. The spot size was increased by these additional optics to 160 μm diameter. The 0.5 cm radius, 800 μm thick Yb:YAG disk was mounted in a copper heatsink and positioned at the focus of the pump light.

At the gain medium there was $\sim$ 1.3 W of pump light available, the reduction due to non AR coated optics and the less than optimal performance of the dichroic mirror. The absorption of the pump light at different diode temperatures was investigated and is shown in Fig 10.3. The absorbed power is close to constant at all diode temperatures and 24°C was selected as a working temperature. This represents a safe intermediate temperature, preventing condensation forming if a lower temperature were used while avoiding the degradation in diode lifetime if operated at a higher temperature. Of the 1.5 W pump power available 66% was absorbed in the Yb:YAG.

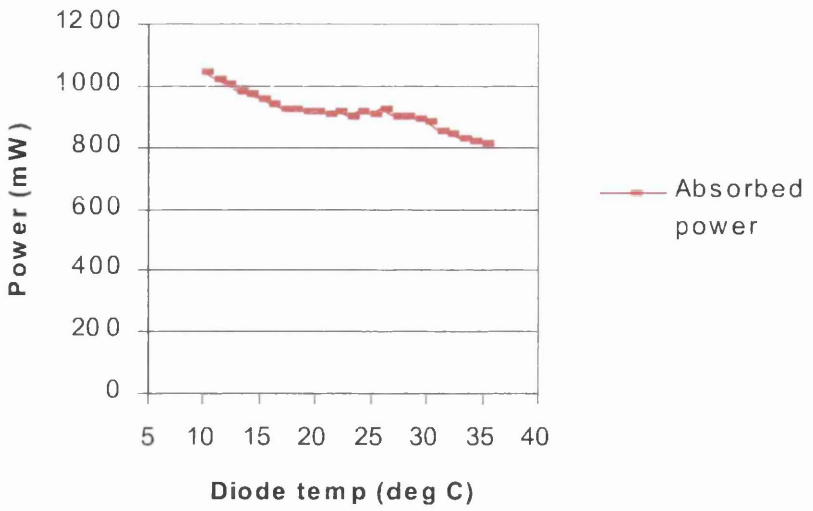

Figure 10.3: *Dependence of absorbed power in Yb:YAG with pumping diode temperature.*

10.4 Laser design

For TEM_{00} operation the diameter of the pump spot w_p should be comparable to the laser mode size w_0 in the laser crystal. A con-focal cavity was found to be the best cavity design to meet this requirement, consisting of two 5 cm radius of curvature high reflectivity mirrors, the dichroic flat high reflectivity and an output coupler. A schematic of the cavity is shown in Fig 10.4 and the cavity has a path length of 15 cm. The gain medium lies at a focus of the con-focal cavity so thermal lensing effects are minimised.

10.5 Laser performance

The free running laser oscillation was found to be bi-directional as expected and in several longitudinal modes (viewed on scanning Fabry-Perot optical spectrum analyser). The Faraday rotator was inserted giving approximately

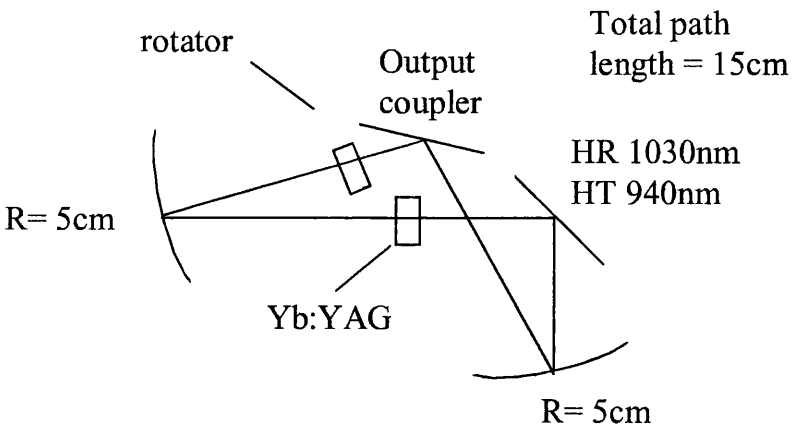

Figure 10.4: *Non-planar cavity design.*

Output coupler transmission	Maximum output power (mW)	Slope efficiency
0.5%	34	0.10
2%	55	0.15
4%	82	0.25
9%	85	0.29
10%	70	0.26

Table 10.1: *Output power from non-planar ring cavity with different output couplers*

3° of polarisation rotation and by careful alignment of the laser mode, the optimal incidence angle could be achieved and unidirectional operation could be enforced. The counter-propagating direction could be selected by turning the Faraday rotator around, reversing its effect. Single frequency operation was achieved, verified using a scanning Fabry-Perot optical spectrum analyser. The output was also highly polarised with a polarisation ratio > 100/1. The M^2 of the laser was found to be 1.25 and 1.37 in the two orthogonal directions. The laser performance was tested with a series of different output couplers. The best power obtained with each and the corresponding slope efficiency (rate of change of laser output power with pumping power) is shown in Table 10.1.

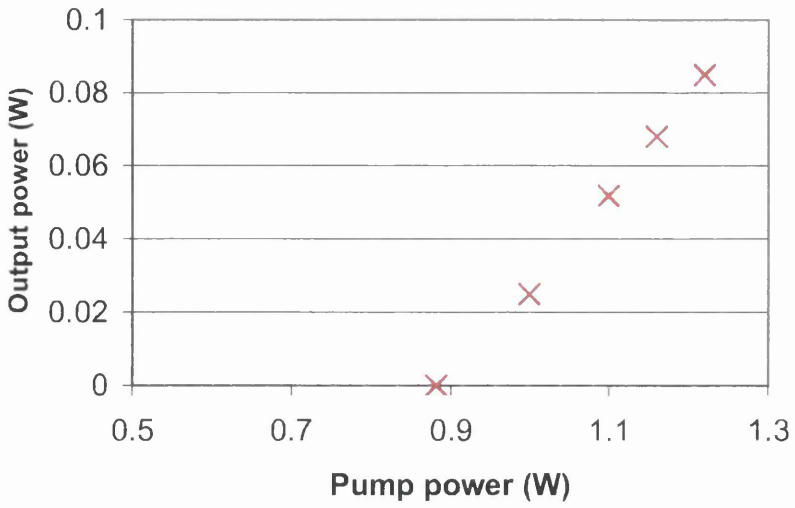

Figure 10.5: *Output power vs pump power for single frequency non-planar ring cavity with 9 % output coupler*

The highest output power and slope efficiency was obtained with a 9 percent transmitting output coupler. The dependence of output power with pumping power is shown in Fig 10.5. The slope efficiency was 0.29 and the threshold pump power was 850 mW. Unfortunately not enough pump power was available to utilise this high extraction efficiency. The relationship between threshold power and output coupler reflectance is shown in Fig 10.6. A Findlay-Clay analysis [53] gives the single pass small signal gain $g_0 l$ to be $0.46 P_{pump}$. The cavity loss would normally be obtained from Fig 10.6 by extrapolating to a threshold pumping power of zero. In this case however the total losses are large, comprising of the passive cavity loss and the re-absorption loss. Extrapolating the fitted line leads to a large error. The Findlay-Clay analysis is therefore not suitable to derive an accurate cavity loss for this laser.

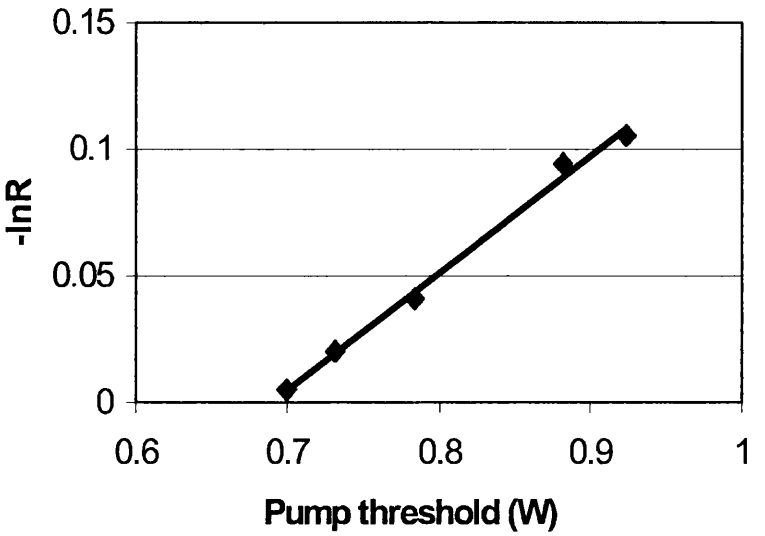

Figure 10.6: *Threshold pump power dependence on output coupling*

10.6 Relaxation oscillation measurements

A 4-level laser has a relaxation oscillation frequency given by

$$f^2 = \frac{1}{(2\pi)^2}\gamma_c\gamma_l(r-1) \tag{10.1}$$

[62] where γ_c is the cavity decay rate, γ_l is the laser level decay rate and r is the normalised pumping rate given by $\frac{\text{Pump power}}{\text{threshold pump power}}$. A quasi 3-level system has an additional factor due to the loss caused by the re-absorption by the populated lower laser level. The corrected relaxation oscillation frequency is given by

$$f^2 = \frac{1}{(2\pi)^2}\gamma_c\gamma_l(r-1)(1+f_l N\frac{\sigma cl}{\gamma_c p}) \tag{10.2}$$

[104] where the factor $f_l N\sigma l$ is the absorption loss in the gain medium of length l and ion density N, situated in a cavity of optical length p. The occupation probability of the lower laser level is f_l. On substituting

$$\gamma_c = \frac{c(\alpha_L - \ln R)}{p} \tag{10.3}$$

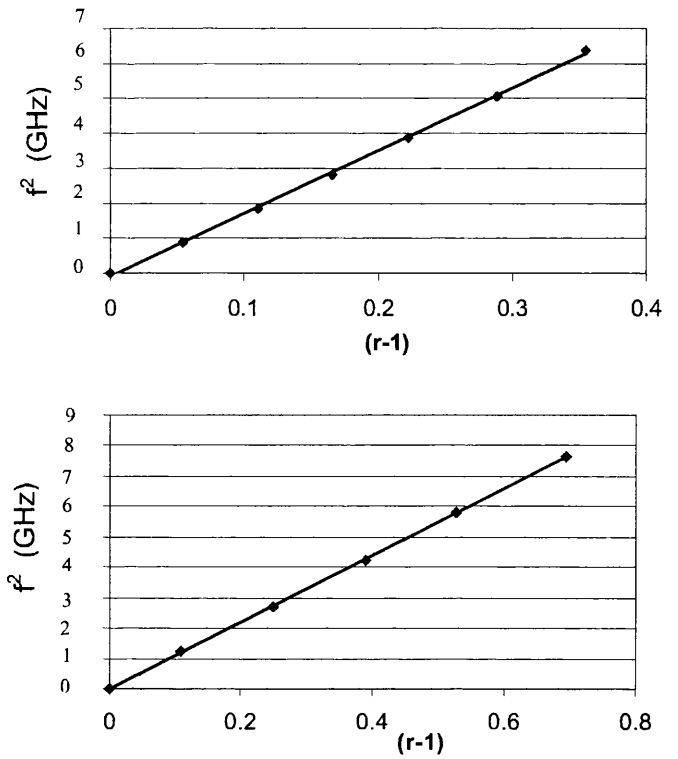

Figure 10.7: *Relaxation oscillation frequency f dependence vs pump rate (r-1)*

[105] the equation can be written as

$$f^2 = \frac{1}{(2\pi)^2}\gamma_c\gamma_l(r-1)(1+\frac{A}{\alpha_L - \ln R}) \tag{10.4}$$

with α_L the intra-cavity loss, A the absorption loss and R the power reflectivity of the output coupler.

The relaxation oscillation frequency was measured at different pumping rates r and for different output couplers and a sample of the results are shown in Fig 10.7. Five different output couplers were used in total.

Using these results, a value for the intra-cavity loss can be derived. The gradient of each of the graphs demonstrated in Figs 10.7 is given by

$$\frac{d(f^2)}{d(r-1)} = \frac{1}{(2\pi)^2}\gamma_c\gamma_l(1+\frac{A}{\alpha_L - \ln R}) = \frac{1}{(2\pi)^2}\frac{\gamma_l c}{p}(K - \ln R)) \tag{10.5}$$

where $K = \alpha_L + A$ is the total loss.

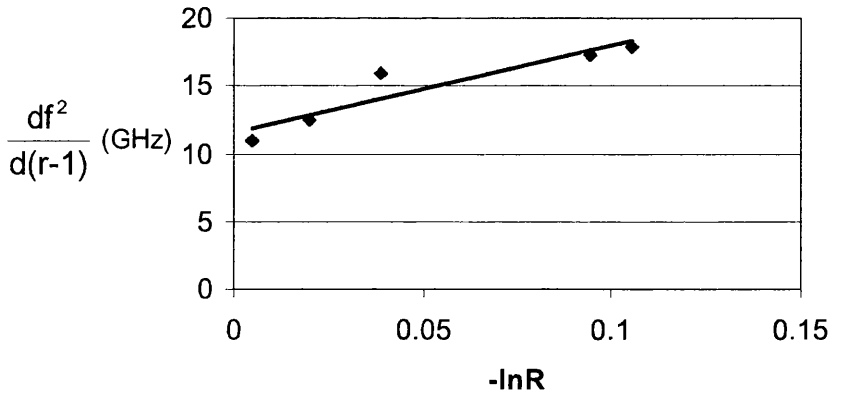

Figure 10.8: $\frac{df^2}{d(r-1)}$ *vs* $-\ln R$ *for different output couplers.*

A linear relationship exists between $-\ln R$ and the gradient. With a plot of these as shown in Fig 10.8, the intercept on the axis is given by

$$\frac{1}{(2\pi)^2}\frac{\gamma_l c}{p}(\alpha_L + A). \tag{10.6}$$

With $l = 800\mu$m, $N = 1.38 \times 10^{27}$ions/m^3, $\sigma = 3.3 \times 10^{-24}$ m^2, $f_l = 0.048$, $\gamma_l = 1051\, s^{-1}$ the cavity losses can be shown to be 0.06.

The theoretical value for the relaxation oscillation frequency can then be found and compared with experimental results. Using the value of cavity loss found above, the theoretical relaxation oscillation frequency can be obtained from Equation 10.4. A comparison of experimental and theoretical values are shown in Table 10.2, for a sample of different output couplers and pumping rates. Experiment and theory are in good agreement.

10.7 Conclusions

A single frequency Yb:YAG laser was constructed which operated in a highly polarised, TEM_{00} mode. The output power was limited to 85 mW, but with a

(r-1)	RO observed (kHz)	RO theory (kHz)
0.35	80.00	77.70
0.22	62.25	61.40
0.05	30.00	30.73

(r-1)	RO observed (kHz)	RO theory (kHz)
0.69	87.50	88.40
0.39	65.00	66.10
0.11	35.50	35.30

Table 10.2: *Comparison of measured and theoretical RO frequency for T=10 % (top) and T=0.5 % (bottom)*

slope efficiency of 0.29, the output power would rise quickly given more pump power.

The relaxation oscillation frequency was measured for a series of different output couplers and the results used to derive the cavity loss factor. Using this loss factor, the measured relaxation oscillation frequency is in good agreement with the theoretical prediction.

Yb:YAG may be the laser medium for future gravitational wave detectors. In the absence of NPRO's of the type described in [48] it may be that a single frequency laser of this type will be required as a master oscillator. This experiment demonstrates the possibility of making a simple low power single frequency laser. It could be stabilised by locking it to a reference cavity to reduce its frequency noise to a suitable level.

Chapter 11

Conclusion

As large scale gravitational wave detectors come online the importance of research work performed on prototype detectors will become clear. The experience gained operating prototype detectors which behave in a similar way to large scale detectors is invaluable. This thesis was an account of the continuing work performed on the Glasgow prototype detector. The work performed on this detector along with the one at the Max Plank Institute in Garching and at other institutes worldwide has formed the basis of knowledge for GEO 600 and other similar detectors.

In recent years only the Glasgow detector has been used to improve levels of displacement sensitivity and at the commencement of the work in this thesis, all the others were using Argon ion lasers. Given that all large scale detectors are to use Nd:YAG lasers the need to perform experiments with, and gain experience of these types of lasers was essential. Several key results had not previously been demonstrated and the Glasgow prototype proved a useful platform for these experiments.

A Nd:YAG laser was constructed and injection locked to produce 4 W of single frequency light. A simple fringe side lock was used to hold the slave laser within the injection locking range, the first time this has been used. This laser offered several times more power than had been available with the Argon

ion laser used before. The injection locked laser was frequency stabilised to $2 \times 10^{-5}\mathrm{Hz}/\sqrt{\mathrm{Hz}}$ around 1 kHz. This is the first time a laser of this type has been stabilised to the level required for gravitational wave detection.

This laser was then used as the light source for the prototype detector and a spectral density of displacement sensitivity of $4 \times 10^{-19}\,\mathrm{m}/\sqrt{\mathrm{Hz}}$ was measured. This is the best result obtained with the Glasgow prototype and the best obtained anywhere with a laser of this type. A better spectral density of displacement sensitivity of $3 \times 10^{-19}\,\mathrm{m}/\sqrt{\mathrm{Hz}}$ was measured at CalTech using an Argon ion laser but this was centred at 400 Hz and the sensitivity degraded only a few hundred Hz from the best point. The result with the injection locked laser demonstrates for the first time a close to shot noise limited displacement sensitivity with a laser of this type and is a crucial demonstration for the operation of the GEO 600, TAMA 300 and VIRGO detcctors.

The internal Q-factor of one of the mirror masses was reduced by smearing grease on its outer surface and the spectral density of displacement sensitivity was degraded to $2 \times 10^{-18}\,\mathrm{m}/\sqrt{\mathrm{Hz}}$. This thermal noise limited spectral density of displacement sensitivity is the first direct measurement of broadband off-resonance thermal noise. This result demonstrates that in the future more controlled experiments could be performed to experimentally verify models of the thermal noise behaviour of mirror masses.

A method of calibrating large scale detectors using radiation pressure to move one detector mirror has been suggested in the past. This was proven to be a valid and accurate calibration technique using the radiation pressure from a power modulated NPRO to move one mirror of the prototype detector. This experiment demonstrates that magnets and coils otherwise used to move a mirror mass need not be used. It may prove a useful technique for the calibration of large scale detectors.

Optical components for GEO 600 were tested in the prototype detector. Low loss calcite polarisers and $LiNbO_3$ electro-optic modulators were tested and

shown to operate to the requirements of GEO 600. A prototype of a novel Brewster angled polariser was tested and is this is now being widely used due to its extremely low loss and high extinction ratio. It is also cheap to produce since it does not require any optical coatings. This polariser could be crucial in the future when much higher power lasers are used which could damage optical coatings. The excess phase noise around the modulation frequency imposed by the electro-optic modulating process was shown to be less than $\sim 3 \times 10^{-8}\mathrm{rad}/\sqrt{\mathrm{Hz}}$ proving that the sensitivity of GEO 600 will not be compromised by this mechanism.

These experiments have demonstrated a displacement sensitivity around 1 kHz limited by the the detected light power. The large scale detectors with improved suspension systems and higher laser powers will now improve the levels of displacement sensitivity further and over a wider frequency range. When the increased arm lengths are considered these detectors will have strain sensitivities comparable to some gravitational wave sources. It is then that the astronomy of gravitational wave detection can begin and a better understanding of astrophysical phenomena can develop.

Bibliography

[1] A. Einstein, "Die Grundlage der Algemeinen Relativitatstheorie," Annalen der Physik, **49**, (1916) pp.769

[2] J.H. Taylor, L.A. Fowler and P.M. McCulloch "Measurements of general relativistic effects in the binary pulsar PSR1913+16," Nature, **277**, (1979) pp. 437-440

[3] B. Willke, P. Aufmuth, R. Balasubramanian, O. S. Brozek, G. Cagnoli, M. Casey, D. Clubley, D. Churches, K. Danzmann, C. Fallnich, A. Freise, S. Goβler, A. Grado, H. Grote, J. Hough, M. Husman, K. Kawabe, H. Luck, P. McNamara, S. McIntosh, K. Mossavi, G. P. Newton, D. Palmer, M. A. Papa, M. V. Plissi, V. Quetschke, D. I. Robertson, N. A. Robertson, S. Rowan, A. Rudiger, B. S. Sathyaprakash, R. Schilling, B. F. Schutz, A. Sintes-Olives, K. D. Skeldon, P. Sneddon, K. A. Strain, I. Taylor, C. I. Torrie, A. Vecchio, H. Ward, H. Welling, W. Winkler, I. Zawischa and C. Zhao, "The GEO 600 Gravitational Wave Detector" in Gravitational Wave Detection II, Universal Academic Press Inc., Tokyo (2000), pp. 25-34.

[4] A. Lazzarini, "The status of LIGO" in Gravitational Wave Detection II, Universal Academic Press Inc., Tokyo, (2000) pp. 1-13

[5] E. Majorana (for the VIRGO collaboration) "Status of Virgo," in Gravitational Wave Detection II, Universal Academic Press Inc., Tokyo (2000), pp. 15-24.

[6] M. Fujimoto for the TAMA collaboration, "An overview of the TAMA Project" in Gravitational Wave detection II, Universal Academic Press Inc., Tokyo (2000), pp. 41-43.

[7] B. F. Schutz, "Gravitational wave astronomy," Classical and Quant. Grav., **16**, 12A, (1999) pp. 131-157

[8] D.G. Blair, "Sources of gravitational waves" in The Detection of Gravitational Waves (Blair ed.), Cambridge University Press, Cambridge (1991), pp. 16-42

[9] J. Hough, B.J. Meers, G.P. Newton, N.A. Robertson, H. Ward, G. Leuchs, T.M. Niebauer, A. Rüdiger, R. Schilling, L. Schnupp, H. Walther, W. Winkler, B.F. Schutz, J. Ehlers, P. Kafka, G. Schafer, M.W. Hamilton, I. Schutz, H. Welling, J.R.J. Bennet, I.F. Corbett, B.H.W. Edwards, R.J.S. Greenhalgh and V. Kose, "Proposal for a Joint German-British Interferometric Gravitational Wave Detector," Technical report MPQ 147 and GWD/137/JH(89), (1989)

[10] S.W. Hawking and W. Israel, "General Relativity," Cambridge University Press (1979)

[11] N. Anderson, "A new class of unstable modes of rotating relativistic stars," Astophys. Journ., **502**, (1998) pp. 708-713

[12] B.J. Owen, "Gravitational waves from the r-modes of rapidly rotating neutron stars," Gravitational waves-procedings of the 3rd Eduardo Amaldi Conf., S. Meshkov ed., Am. Inst. Phys., (2000) pp. 55-64

[13] P. Astone, M. Bassan, P. Bonifazi, P. Carelli, M. G. Castellano, G. Cavallari, E. Coccia, C. Cosmelli, V. Fafone, S. Frasca, E. Majorana, I. Modena, G. V. Pallottino, G. Pizzella, P. Rapagnani, F. Ricci, and M. Visco, "Long-term operation of the Rome Explorer cryogenic gravitational wave detector," Phys. Rev. D, **47**, (1993) pp. 362-375

[14] E. Mauceli, Z. K. Geng, W. O. Hamilton, W. W. Johnson, S. Merkowitz, A. Morse, B. Price, and N. Solomonson, "The Allegro gravitational wave detector: Data acquisition and analysis," Phys. Rev. D, **54**, (1996) pp. 1264-1275

[15] M.E. Tobar, C.R. Locke, I.S. Heng, E.N. Ivanov and D.G. Blair, "Niobe: Improved Noise Temperature and Ground Noise Suppression," Gravitational waves-procedings of the 3rd Eduardo Amaldi Conf., S. Meshkov ed., Am. Inst. Phys., (2000) pp. 283-289

[16] M. Cerdonio, L. Taffarello, J.P. Zendri, L. Conti, V. Crivelli Visconti, A. Ortolan, G. Vedovato, R. Mezzena, G.A. Prodi, S. Vitale, M. Bonaldi, P. Falferi, P. Fortini, "The ultracryogenic gravitational wave detector Auriga: a progress report," Gravitational wave detection - Proceedings of the TAMA workshop on gravitational waves, Universal Academy Press, Tokyo, (1997) pp. 203-211

[17] P. Astone, M. Bassan, P. Bonifazi, P. Carelli, E. Coccia, C. Cosmelli, V. Fafone, S. Frasca, A. Marini, G. Mazzitelli, Y. Minenkov, I. Modena, G. Modestino, A. Moleti, G. V. Pallottino, M. A. Papa, G. Pizzella, P. Rapagnani, F. Ricci, F. Ronga, R. Terenzi, M. Visco and L. Votano, "The gravitational wave detector NAUTILUS operating at T = 0.1 K," Astroparticle phys., **7**, (1997) pp. 231-243

[18] E. Coccia, "Bars in action," Gravitational waves-procedings of the 3rd Eduardo Amaldi Conf., S. Meshkov ed., Am. Inst. Phys., (2000) pp. 32-36

[19] Z. A. Allen, P. Astone, L. Baggio, D. Busby, M. Bassan, D. G. Blair, M. Bonaldi, P. Bonifazi, P. Carelli, M. Cerdonio, E. Coccia, L. Conti, C. Cosmelli, V. Crivelli Visconti, S. D'Antonio, V. Fafone, P. Falferi, P. Fortini, S. Frasca, W. O. Hamilton, I. S. Heng, E. N. Ivanov, W. W. Johnson, M. Kingham, C. R. Locke, A. Marini, V. Martinucci, E. Mauceli, M. P. McHugh, R. Mezzena, Y. Minenkov, I. Modena, G. Modestino, A. Moleti, A. Ortolan, G. V. Pallottino, G. Pizzella, G. A. Prodi, E. Rocco, F. Ronga, F. Salemi, G. Santostasi, L. Taffarello, R. Terenzi, M. E. Tobar, G. Vedovato, A. Vinante, M. Visco, S. Vitale, L. Votano and J. P. Zendri, "First search for Gravitational Wave Bursts with a Network of detectors," Phys. Rev. Lett., **85**, 24, (2000) pp. 5046-5050

[20] W. Winkler, "A Michelson interferometer using delay lines" in The Detection of Gravitational Waves (Blair ed.), Cambridge University Press, Cambridge (1991), pp. 269-304

[21] N.A. Robertson, "Vibration isolation for test masses" in The Detection of Gravitational Waves (Blair ed.), Cambridge University Press, Cambridge (1991), pp. 353-368

[22] Private communication (2000)

[23] P.R. Saulson, "Thermal noise in mechanical experiments," Phys. Rev. D, **42**, 8, (1990) pp. 2437-2444

[24] N.A. Robertson, G. Cagnoli, J. Hough, M.E. Husman, S. McIntosh, D. Palmer, M.V. Plissi, D.I. Robertson, S. Rowen, P. Sneddon, K.A. Strain, C.I. Torrie and H. Ward, "Suspension design for GEO 600 - an update,"

in Gravitational Wave Detection II, Universal Academic Press Inc., Tokyo (2000), pp. 313-319

[25] S. Rowan, G. Cagnoli, P. Sneddon, J. Hough, R. Route, E. K. Gustafson, M. M. Fejer and V. Mitrofanov, "Investigation of mechanical loss factors of some candidate materials for the test masses of gravitational wave detectors," Phys. Lett. A, **265**, (2000) pp. 5-11

[26] S. Rowan, S. M. Twyford, R. Hutchins, J. Kovalik, J. E. Logan, A. C. McLaren, N. A. Robertson and J. Hough, "Q factor measurements on prototype fused quartz pendulum suspensions for use in gravitational wave detectors," Phys. Lett. A, **233**, (1997), pp. 303-308

[27] R.W.P. Drever, J. Hough, A.J. Munley, S.A. Lee, R. Spero, S.E. Whitcomb, H. Ward, G.M. Ford, M. Hereld, N.A. Robertson, I. Kerr, J.R. Pugh, G.P. Newton, B. Meers, E.D. Brooks and Y. Gursel in "Quantum Optics, Experimental Gravitation and Measurement Theory," P. Meystre and M.O. Scully eds., Plenum Press, New York, (1983) pp. 503-514

[28] B.J. Meers, "Recycling in laser interferometric gravitational wave detectors," Phys. Rev. D, **38**, 8, (1988) pp. 2317-2326

[29] A. Freise, G. Heinzel, K. A. Strain, J. Mizuno, K. D. Skeldon, H. Lück, B. Willke, R. Schilling, A. Rüdiger, W.Winkler and K. Danzmann, "Demonstration of detuned dual recycling at the Garching 30 m laser interferometer," Phys. Lett. A, **277**, (2000) pp. 135-142

[30] J. Mizuno, K.A. Strain, P. Nelson, J. Chen, R. Schilling, A. Rüdiger and K. Danzmann, "Resonant sideband extraction- a new configuration for interferometric gravitational wave detectors," Phys. Lett. A, **175**, (1993) pp. 273-279

[31] D.A. Shaddock, M.B. Gray, and D.E. Mclelland, "Frequency locking a laser to an optical cavity using spatial mode interference," Opt. Lett. **24**, 21, (1999) pp. 1499-1501

[32] T.W. Hansch and B. Couillaud, "Laser frequency stabilisation by polarisation spectroscopy of a reflecting reference cavity," Opt. Comm., **35**, 3, (1980) 441-444

[33] D. Hils and J.L. Hall, "Response of a Fabry-Perot cavity to phase modulated light," Rev. Sci. Instum., **58**, (1987) pp.1406-1412

[34] R.W.P. Drever, J.L. Hall, F.V. Kawalski, J. Hough, G.M. Ford, A.J. Munley and H. Ward, "Laser phase and frequency stabilisation using an optical resonator," App. Phys. B, **31** (1983) pp.97-105

[35] K.P. Birch, "A compact optical isolator," Opt. Comm., **43**, (1982) pp. 79-80

[36] I.P. Kaminow and E.H. Turner, "Electrooptic Light Modulators," I.P. Kaminow and E.H. Turner, Proc. IEEE, **54**, pp. 1374-1390

[37] S.D. Killbourn, "Double pendulums for terrestrial interferometric gravitational wave detectors," PhD Thesis, University of Glasgow, (1997)

[38] E. Morrison, "Experimental investigations relevent to the development of a laser interferometric gravitational wave detector," PhD Thesis, University of Glasgow, (1993)

[39] M.E. Husman, C.I. Torrie, M.V. Plissi, N.A. Robertson, K.A. Strain and J. Hough, "Modeling of multistage pendulums: Triple pendulum for GEO 600," Rev. Sci. Instrum., **71**, 6, 2000, pp. 2546-2551

[40] D.I. Robertson, E. Morrison, J. Hough, S. Killbourne, B.J. Meers, G.P. Newton, N.A. Robertson, K.A. Strain and H. Ward, "The Glasgow 10 m

prototype interferometric gravitational wave detector," Rev. Sci. Instrum., **66**, 9, (1995) pp. 4447-4452

[41] J. Hough, H. Ward, G.A. Kerr, N.L. Mackenzie, B.J. Meers, G.P. Newton, D.I. Robertson, N.A. Robertson and R. Schilling, "The stabilisation of lasers for interferometric gravitational wave detectors" in The Detection of Gravitational Waves (Blair ed.), Cambridge University Press, Cambridge (1991), pp.329-351

[42] N.A. Robertson, S. Hoggan, J.B. Mangan and J. Hough, "Intensity stabilisation of an Argon Laser using an Electro-optic modulator - performance and limitations", App. Phys. B., **39**, (1986) pp. 149-153

[43] G.A. Kerr, J. Hough, "Coherent addition of Laser Oscillators for Use in Gravitational Wave Detectors," Appl. Phys. B, **49**, (1989) 491-495

[44] O.S. Brozek, K. Mossavi, K. Danzmann, I. Zawischa, M. Peterseim, C. Fallnich, H. Welling, V. Quetschke, H. Lück and B. Willke, "The GEO 600 laser source: a 12 W frequency stabilised injection-locked Nd:YAG laser system" in Gravitational Wave Detection II, Universal Academic Press Inc., Tokyo (2000), pp.295-300.

[45] F. Cleva, M. Taubman, C.N. Mann and A. Brillet, "Virgo laser source," Proceedings of the 2nd Eduardo Amaldi Conference on Gravitational Waves (E. Coccia, G. Pizzella and G. Veneziano, Eds) pp.321-327

[46] S.T. Yang, Y. Imai, M. Oka, N. Eguchi and S. Kubota, "Frequency stabilised, 10 W continuous-wave, laser diode end pumped, injection locked Nd:YAG laser," Optics letters, **21**, 20, (1996) pp.1676-1679

[47] MISER & DCP Products and LIGO Amplifier, Lightwave Electronics Corp., Mountain View, Cal. (1998)

[48] T.J. Kane and R.L. Byer, "Monolithic, unidirectional single mode Nd:YAG ring laser," Optics Letters, **10**, 2 (1985) pp.65-67

[49] A.D. Farinas, E.K. Gustafson and R.L. Byer, "Design and characterisation of a 5.5 W, cw, injection locked, fiber-coupled, laser-diode-pumped Nd:YAG minature-slab laser," Optics Letters, **19**, 2 (1994) pp.114-116

[50] H. Kogelnik and T. Li, "Laser beams and resonators," Proc. IEEE, **54**, (1966) pp.1312-1329

[51] W. Koechner, "Solid-State Laser Engineering,", Springer-Verlag Berlin, (1992) pp. 79-143

[52] See for example W. Koechner, "Solid-State Laser Engineering,", Springer-Verlag Berlin, (1992) pp. 133 or A. Siegman, "Lasers," Oxford University Press, (1986) pp. 296

[53] D. Findlay and R.A. Clay, "The measurement of internal losses in 4-level lasers," Phys. Lett., **20**, 3, (1966) pp.277-278

[54] R. Adler "A study of locking phenomena in oscillators," Proc. IRE **34**, 351 (1946)

[55] A. Siegman, "Lasers," Oxford University Press, (1986) pp. 1130-1162

[56] A.D. Farinas, E.K. Gustafson and R.L. Byer, "Frequency and intensity noise in an injection-locked, solid state laser," J. Opt. Soc. Am., **12**, 2 (1995) pp.328-334

[57] I. Freitag, D. Golla, A. Tünnerman, H. Welling and K. Danzmann, "Diode Pumped solid-state lasers as light sources for Michelson-type gravitational wave detectors," Appl. Phys. B, **60**, (1995) pp. 255-260

[58] R. Shine, "A high power, diode-laser-pumped solid state laser for precision interferometry," PhD Thesis, Stanford University (1995)

[59] C.N. Nabors, A.D. Farinas, T. Day, S.T. Yang, E.K. Gustafson and R.L. Byer, "Injection locking of a 13 W cw Nd:YAG ring laser," Optics Letters, **14**, 21 (1989) pp.1189-1191

[60] D. Ottaway, P.J. Veitch, M.W. Hamilton, C. Hollitt, D. Mudge and J. Munch, "A compact injection locked Nd:YAG laser for gravitational wave detection," IEEE Journ. of Quant. Elec., **34**, 10, (1998) pp. 2006-2009

[61] G. Mueller and K. Ueda, "Stabilisation of injection locking using a polarisation spectroscopic technique," Jpn. Journ. Appl. Phys., **37**, 6A, (1998), pp. 3313-3318

[62] W. Koechner, "Solid-State Laser Engineering,", Springer-Verlag Berlin, (1992) pp. 104-107

[63] S. Rowen, A.M. Campbell, K.D. Skeldon and J. Hough, "Broadband intensity stabilisation of a diode-pumped monolithic miniature Nd:YAG ring laser," Journ. of Mod. Opt., **41**, 6, (1994) pp. 1263-1269

[64] C.C. Harb, M.B. Gray, H.A. Bachor, R. Schilling, P. Rottengatter, I. Freitag and H. Welling, "Suppression of the intensity noise of a diode pumped Nd:YAG non-planar ring laser," IEEE Journ. of Quant. Elec., **30**, (1994) pp 2907-2911

[65] T. Kane, "Intensity noise in diode pumped single-frequency Nd:YAG lasers and its control by electronic feedback," IEEE Photonics Tech. Lett., **2**, 4, (1990) pp. 244-246

[66] T. Day, E.K. Gustafson and R.L. Byer, "Sub-Hertz relative frequency stabilisation of two-diode laser-pumped Nd:YAG lasers locked to a Fabry-Perot Interferometer," IEEE Journ. Quant. Electron, **28**, 4, (1992) pp. 1106-1116

[67] M. Musha, K. Nakagawa and K. Ueda, "Wideband and high frequency stabilisation of an injection locked Nd:YAG laser to a high-finesse Fabry-Perot cavity," Opt. Lett., **22**, 15, (1997) pp. 1177-1179

[68] M. Musha, T. Kanaya, K. Nakagawa and K. Ueda, "The short and long term frequency stabilisation of an injection locked Nd:YAG laser in reference to a Fabrt-Perot cavity and an iodine saturated absorption line," Opt. Comm., **183**, (2000) pp. 165-173

[69] N. Uehara and K. Ueda, "Ultrahigh-frequency stabilisation of an diode-pumped Nd:YAG laser with a high-power-acceptance photodetector," Opt. Lett., **19**, 10, (1993) pp. 728-730

[70] B. Willke, O.S. Brozek, K. Danzmann, C. Fallnich, S. Goβler, H. Lück, K. Mossavi, V. Quetschke, H. Welling and I. Zawischa, "The GEO 600 Stabilised Laser System and the Current-lock Technique," Gravitational Waves, Proceedings of the 3rd Edoardo Amaldi Conference, American Inst. Physics, New York, (2000) pp. 215-220

[71] M. Musha, S. Telada, K. Nakagawa, M. Ohashi and K. Ueda, "Measurement of frequency noise spectra of frequency stabilised LD-pumped Nd:YAG laser by using a cavity with seperately suspended mirrors," Opt. Comm., **140**, (1997) pp. 323-330

[72] F. Bondu, P. Fritschel, C.N. Mann and A. Brillet, "Ultrahigh-spectral-purity laser for the VIRGO experiment," Optics letters, **21**, 8, (1996), pp.582-584

[73] LISO by G. Hienzel

[74] M.M. Casey, "Developments Towards Autonomous Operation of Laser Interferometric Gravitational Wave Detectors," PhD Thesis, University of Glasgow, (1999)

[75] E.I. Gordon, "A review of Acoustooptical Deflection and Modulation Devices," Proc. IEEE, **54**, (1966) pp. 1391-1401

[76] A.L. Schawlow and C.H. Townes, "Infrared and Optical Masers," Phys. Rev., **112**, (1958) pp. 1940-1949

[77] D.A. Clubley, K.D. Skeldon, B.W. Barr, G.P. Newton, K.A. Strain and J. Hough, "Ultrahigh level of frequency stabilisation of an injection locked Nd:YAG laser with relevance to gravitational wave detection," Optics Comm., **186**, (2000) 177-184

[78] B. Willke, S. Brozeck, K. Danzmann, V. Quetschke and S. Gossler, "Frequency stabilisation of a monolithic Nd:YAG ring laser by controlling the power of the laser-diode pump source," Optics Letters, **25**, 14, pp.1019-1021

[79] A.M. Campbell, S. Rowen and J. Hough, "Apparent relaxation oscillations in the frequency noise of a diode-pumped miniature Nd:YAG ring laser," Phys. Lett. A, **170**, 5, (1992) pp. 363-369

[80] A. Kaminskii, "Laser Crystals," 2nd Edition, Springer Verlag (1990)

[81] L.G. Kazovsky and D.A. Douglas, "Miniature Nd:YAG Lasers: Noise and Modulation Characteristics," Journ. of Lightwave Tech., **8**, 3, (1990) pp. 294-301

[82] K.D. Skeldon, D.A. Clubley, G.P. Newton and J. Hough,"An upper limit to the frequency noise associated with the relaxation oscillation of a monolithic Nd:YAG ring laser," Journ. Mod. Optics., **48**, (2001) 1129-1134

[83] A. Abramovici, W. Althouse, J. Camp, D. Durance, J.A. Giaime, A. Gillespie, S. Kawamura, A. Kuhnert, T. Lyons, F.J. Raab, R.L. Savage Jnr, D. Shoemaker, L. Sievers, R. Spero, R. Vogt, R. Weiss, S. Whitcomb and

M. Zucker, "Improved sensitivity in a gravitational wave interferometer and implications for LIGO," Phys. Lett. A, **218**, (1996) pp. 157-163

[84] D. Shoemaker, R. Schilling, L. Schnupp, W. Winkler, K. Maischberger and A. Rüdiger, "Noise behavior of the Garching 30-meter prototype gravitational-wave detector", Phys. Rev. D, **38**, (1988) pp. 423-427

[85] M. Ando and the TAMA collaboration, "Stable operation of a 300-m Laser Interferometer with sufficient sensitivity to detect gravitational wave events within our galaxy," Phys. Rev. Lett, **86**, (2001) pp. 3950-3954

[86] Measurement of mirror Q-factor performed by P. Sneddon and G. Cagnoli

[87] G. Cagnoli, Private communication (2001)

[88] Measurement of mirror Q-factor performed by P. Sneddon and G. Cagnoli

[89] K.D. Skeldon, D.A. Clubley, B.W. Barr, M.M. Casey, J. Hough, S.D. Killbourn, P.W. McNamara, G.P. Newton, M.V. Plissi, D.I. Robertson, N.A. Robertson, K.A. Strain and H. Ward, "Performance of the Glasgow 10 m prototype gravitational wave detector operating at λ=1064 nm," Phys. Lett. A, **273** (2000) 277-284

[90] D.A. Clubley, K.D. Skeldon, G.P. Newton, K.A. Strain and J. Hough, "Improved performance of the Glasgow prototype gravitational wave detector using an injection locked Nd:YAG laser," Phys. Lett. A, (2000)

[91] A.D. Gillespie, "Thermal noise in the initial LIGO interferometer," PhD Thesis, California Institute of Technology (1997)

[92] F. Raab, Private communication (2001)

[93] H. Ward, "Photon Pressure as a feedback mechanism for interferometric control," Proc. of the 8th GEO 600 workshop, (1998)

[94] D.A. Clubley, G.P. Newton, K.D. Skeldon and J. Hough, "Calibration of the Glasgow 10 m prototype laser interferometric gravitational wave detector using photon pressure," Phys. Lett. A, **283** (2001) 85-88

[95] LEYSOP, 17 Repton Court, Burntmills, Basildon, Essex, UK

[96] Description of the behaviour of o-ray and e-ray found in R.S. Longhurst, "Geometrical and Physical optics," Longman Group, pp. 533-542, 3rd edition (1973)

[97] K.D. Skeldon, "Aspects of improvement in the sensitivity of long-baseline laser interferometric gravitational wave detectors," PhD thesis, University of Glasgow (1995)

[98] K.D. Skeldon, D.A. Clubley, G.P. Newton, S. Thieux, M. Von Gradowski and B. Barr, "Measurements of an ultra low loss polariser for λ=1064 nm using a high finesse optical cavity," Journ. Mod. Opt., **48** (2000) 695-702

[99] FINESSE an optical modelling package by A. Freise

[100] K.A. Strain, Private communication (2000)

[101] D.A. Clubley, G.P. Newton, K.D. Skeldon, K.A. Strain and J. Hough, "Narrow band phase noise measurement around an electro-optically applied phase modulation of a laser field," Journ. Opt.A, **3** (2001) 196-199

[102] W.M. Tulloch, T.S. Rutherford, E.H. Huntington, R. Ewart, C.C. Harb, B. Willke, E.K. Gustafson, M.M. Fejer, R.L. Byer, S.Rowan, and J. Hough, " Quantum noise measurements in a cw laser-diode-pumped Nd:YAG linear optical amplifier," Optics Letters, **23**, pp. 1852-1854 (1998)

[103] T.S. Rutherford, W.M. Tulloch, E.K. Gustafson and R.L. Byer, "Edge-pumped quasi-three-level slab lasers: Design and power scaling," IEEE Journal of Quant. Elec., **36**, 2, pp. 205-219 (2000)

[104] J.R. Salcedo, J.M. Sousa and V.V. Kuzmin,"Theoretical treatment of relaxation oscillations in quazi-three-level systems," Appl. Phys. B, **62**, pp. 83-85 (1996)

[105] A. Siegman, "Lasers," Oxford University Press, (1986) pp. 430